Alma Mater Studiorum · Università di Bologna

Scuola di Scienze

Corso di Laurea Magistrale in Fisica del Sistema Terra

Topographic and Mixed Layer Submesoscale Currents in the Carribean Sea

Relatore:

Prof. Francesco Trotta

Correlatore:

Prof.ssa Nadia Pinardi

Presentata da:

Alessandra Stoppelli

Anno Accademico 2022/2023

"When a complex system is far from equilibrium, small islands of coherence in a sea of chaos have the capacity to shift the entire system to a higher order."

Ilya Prigogine

I would like to express my gratitude to Francesco Trotta for his guidance and support throughout my thesis. I am thankful for the time and effort he has invested, patiently guiding me through challenges and providing constructive feedback that has significantly contributed to refining my work.
I would also like to extend my appreciation to Nadia Pinardi for granting me the opportunity to work on this theme during the past months. Her passion and dedication have been a constant source of inspiration for me.
Finally, I would like to thank Rita Lecci and the OPA division of the CMCC, which allowed the use of the SuperComputer of the CMCC, essential in this work.

Abstract

Recent advancements in observation and modelling techniques with higher spatial resolution have allowed us to discover a considerable amount of structures and processes in the upper ocean with horizontal scales as small as a kilometer. These processes, referred to as submesoscale, are characterized by Rossby and Richardson numbers of the order of one.

They have distinct dynamics compared to the quasi-geostrophic mesoscale and the fully three-dimensional small-scale processes and can transfer energy between them, thereby providing a route to dissipation.

The submesoscale processes are significant contributors to the vertical flux of mass, buoyancy, and tracers in the upper ocean. They play a crucial role in altering the upper-ocean stratification and mixed-layer structure on a timescale of days by facilitating communication between the pycnocline and the surface and simplifying the potential vorticity flux through the mixed layer.

The goal of this thesis is to investigate the submesoscale dynamics in the Caribbean Sea using a high (1/36°, 3 km) resolution model. The simulations are run using SURF, a NEMO-based relocatable ocean modeling platform for downscaling, with beginning and boundary conditions set to CMEMS (1/12°, 9 km). The interest period is February 2021.

This allows to observe submesoscale features in our region, however, by employing dynamical downscaling, we can reduce computing costs.

In the numerical simulation of the Caribbean Sea, the distribution and strength of submesoscale (SM) surface layer fronts and filaments formed by mixed layer baroclinic energy conversion and submesoscale coherent vortices (SCVs) generated by topographic drag are investigated. The mixed layer baroclinic energy conversion is studied through variables as Mixed Layer Depth (MLD), relative vorticity, horizontal and vertical velocities, Kinetic Energy (KE) and Brunt-Väisälä frequency, while the generation of SCV is studied through variables as the Laplacian of the Sea Surface Temperature, the vertical velocity field and the horizontal Reynolds stress (HRS) field. A combination of equatorial closeness and boundary drag produces SCVs with high Rossby numbers ($Ro \sim 10$) in the topographically complicated Chibcha channel. Conversions of mean to eddy kinetic energy indicate barotropic instability in SM topographic wakes.

These fields were analysed for different bathymetric and topographic configurations, carrying out a sensitivity experiments.

Sommario

Grazie ai recenti progressi nelle tecniche di osservazione e modellazione, caratterizzati da una maggiore risoluzione spaziale, sono stati rivelati numerosi dettagli riguardanti le strutture e i processi presenti nella parte superiore dell'oceano, con scale orizzontali dell'ordine del chilometro. Questi processi, chiamati di sottomesoscala, sono caratterizzati da numeri di Rossby e Richardson dell'ordine di uno. Le dinamiche che si osservano in queste strutture presentano caratteristiche distinte rispetto alla mesoscala, con un regime quasi-geostrofico, e differiscono dai processi tridimensionali a scala più piccola, aprendo la via per la dissipazione. I processi di sottomesoscala svolgono un ruolo di grande importanza nel flusso verticale di massa e traccianti nell'oceano superiore. Contribuiscono, in modo significativo all'alterazione della stratificazione nella parte superiore dell'oceano e alla struttura del mixed layer su una scala temporale giornaliera. Questi processi facilitano la comunicazione tra il picnoclino e la superficie dell'oceano, consentendo il flusso di vorticità potenziale attraverso il mixed layer.

L'obiettivo di questa tesi è quello di studiare le dinamiche alla sottomesoscala nel Mar dei Caraibi utilizzando un modello ad alta risoluzione (1/36°, 3 km). Le simulazioni sono state eseguite tramite SURF, una piattaforma di modellazione oceanica rilocabile basata su NEMO. Il modello nidificato è ottenuto tramite "downscaling" dei campi medi giornalieri dal modello globale CMEMS su larga scala (1/12°, 9 km) nel mese di febbraio 2021. Ciò consente di osservare le caratteristiche di sottomesoscala nella nostra regione, tuttavia, utilizzando il downscaling dinamico, possiamo ridurre i costi di calcolo. Nel presente lavoro, viene analizzata la distribuzione e l'intensità di fronti e filamenti di sottomesoscala (SM) nella superficie, generati dalla conversione di energia baroclina nel mixed layer e dai vortici coerenti di sottomesoscala (SCV) generati dalla resistenza topografica. La conversione dell'energia baroclinica all'interno del mixed layer è stata oggetto di studio attraverso diverse variabili, tra cui la profondità del mixed layer, la vorticità relativa, le velocità orizzontali, l'energia cinetica e la frequenza di Brunt-Väisälä. D'altra parte, la generazione di SCV è stata analizzata in relazione al gradiente spaziale della temperatura della superficie del mare, al campo di velocità verticale e al campo di stress di Reynolds orizzontale (HRS). È stato osservato che la vicinanza all'equatore e la forza di resistenza ai margini produce SCV con numeri di Rossby elevati ($Ro \sim 10$) nel canale Chibcha, caratterizzato da complesse formazioni topografiche. Inoltre, la conversione dell'energia cinetica media indica la presenza di instabilità barotropa nelle scie topografiche di sottomesoscala. Questi campi sono stati analizzati per diverse configurazioni batimetriche e topografiche, effettuando esperimenti di sensibilità.

Contents

CHAPTER 1

Introduction

Surface currents in the ocean are primarily driven by wind patterns with scales of $\sim$ 1000 km and larger (synoptic scale). Wind-driven currents display instabilities at the mesoscale, leading to the formation of mesoscale eddies that have the highest kinetic energy in the ocean (see Fig.1.1 from Torres et al. 2018), (John R Taylor 2023).

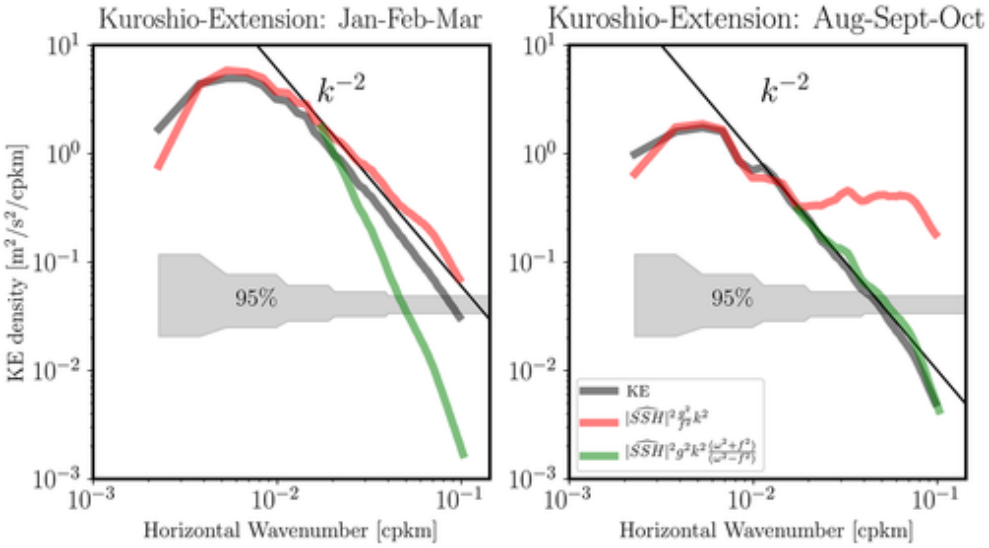

Figure 1.1: Wave number spectra of kinetic energy ($m^2/s^2/(\text{cpkm})$) deduced from (u, v) (gray line), and from sea surface height (geostrophic kinetic energy; red line), and the kinetic energy of internal gravity waves (green line). The shaded gray bands denote the 95% confidence interval. The k^{-2} slope is for the large scales and the flat slope for smaller scales (Torres et al. 2018).

The dominant dynamical theory for oceanic circulation incorporates these mesoscale currents together with mixing and dissipation which is mainly due to microscale flows such as turbulent boundary layers and breaking internal waves (with reference to 1.3). In this work we examine the existence and importance of submesoscale currents at an intermediate scale as an additional crucial component of the oceanic general circulation (Capet et al. 2008a).

The ocean's variability is dominated by mesoscale fluctuations, characterized by a horizontal length scale of 10 to 100 km, their impact on climate is important because its contribution to the lateral transport of heat, momentum, and tracers by means of eddies. Previous field experiments suggested that eddy energy is primarily generated by instability processes of intense boundary currents and radiated subsequently into the interior ocean by Rossby waves. Direct atmospheric forcing by variable wind stress was also considered an important eddy source term in areas remote from intense currents. In addition, small-scale topography can transfer large-scale energy to smaller baroclinic scales through mode-mode coupling (the interplay between distinct oscillation modes in a system).

The geographical variation of eddy amplitude and eddy scales presents a challenge to understanding ocean eddy dynamics and source terms, requiring a systematic regional investigation of observed eddy characteristics. Modern measurement technologies and advanced developments in numerical ocean simulations have improved understanding of the generation and distribution of oceanic mesoscale (Stammer 1997).

As explained above mesoscale eddies in the ocean are responsible for a significant portion of the ocean's heat, momentum and tracers transport. However, there is also a lot of submesoscale variability in the ocean, with horizontal scales of 0.1-10 km and temporal scales of hours to days.

The submesoscales processes are less understood and have only recently been analyzed through observational, modeling, and analytical studies.

Submesoscale motions are mainly generated by mesoscale eddies and strong currents, and they occur along the edges of eddies, mainly caused by frontal sharpening generated from the mesoscale strain. Submesoscale processes can break down the balance in the ocean and contribute significantly to vertical heat transport, transferring heat from the cold lower layer to the warm upper layer (Wang et al. 2022). A significant amount of energy in the ocean is concentrated at medium to large scales where the flow is mostly two-dimensional and in a state of balance that makes it hard to extract energy. The strong and non-balanced flow at the submesoscale level can extract energy from the balanced state and transfer it to smaller scales.

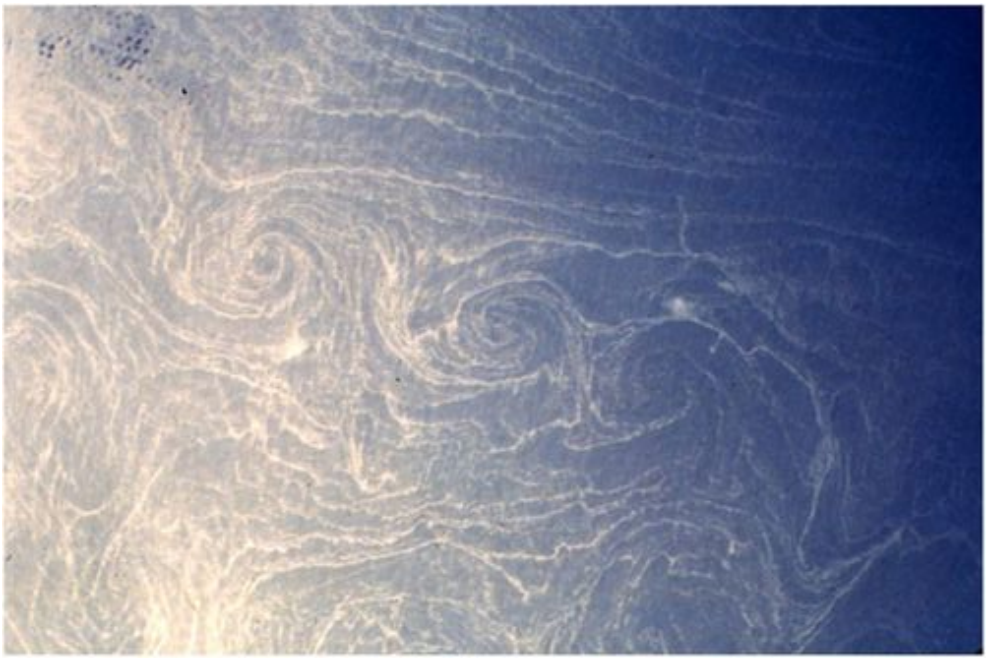

Figure 1.2: Vortex with radii ∼5 Km near the Mediterranean coast of Africa photographed from space. The pattern suggests a vortex-street roll-up has occurred from a lateral shear instability of some parent front, filament or topographic wake. (McWilliams 2016)

1.1 Multiscale Ocean Fluid Dynamics

The ocean dynamics involve different scales, ranging from the large gyres that span ocean basins to the smallest 3D turbulent motions, which are separated by approximately nine orders of magnitude, from 10^{-4} m to 10^{6} m.

The interconnections of the features observed across scales ranging from several hundred meters to several hundred kilometres reflects the intrinsically multiscale nature of fluid dynamics in the ocean. Mesoscale and submesoscale motions can be distinguished by the relative importance of the Earth's rotation. Submesoscales play a critical role in this dynamical coupling by bridging the gap between rotating and nonrotating flows.

The Rossby number is a fundamental nondimensional quantity in Geophysical Fluid Dynamics, and the characteristics of geophysical flow vary greatly with the value of the Rossby numbers.

The ratio of inertial forces (momentum advection) and Coriolis accelerations scales with the *Rossby number* (Ro).

$$\frac{|\boldsymbol{u}\cdot\nabla\boldsymbol{u}|}{|2\boldsymbol{\Omega}\times\boldsymbol{u}|}\sim\frac{U}{fL}=Ro, \tag{1.1}$$

where U and L are respectively characteristic horizontal velocity and length scales, $\boldsymbol{\Omega}$ is the Earth's rotation vector ($\boldsymbol{\Omega}=\hat{j}(2|\Omega|cos\theta)+\hat{k}(2|\Omega|sin\theta)$), and $f=2\Omega sin\theta$ is the

Coriolis parameter at a fixed latitude θ. Mesoscale eddies are characterized by $Ro \ll 1$, and the dominant terms in the momentum equations are the horizontal pressure gradient and the Coriolis acceleration, such that the flow is close to geostrophic balance. Submesoscales are characterized by $Ro \sim 1$ and, hence, the Coriolis acceleration is important, but it does not constrain the motion to the same extent as the mesoscale. The removal of this constraint allows stronger vertical velocities to develop at submesoscales.

In addition to the importance of rotation with respect to the fluid inertia, at a given scale, we can also evaluate the importance of buoyancy and viscous effects compared to the fluid inertia , respectively with two nondimensional parameters that are the *Froude number* (Fr) and the *Reynolds number* (Re) defined as

$$Fr = \frac{U}{NL}, \qquad Re = \frac{UL}{\nu}. \tag{1.2}$$

Where $N = \sqrt{\partial b/\partial z}$ is Brunt-Väisälä frequency and $b = -g\rho/\rho_0$ is the buoyancy; while ν is the kinematic viscosity; $\rho_0 = 1025 kg/m^3$ is the reference density value. The gravitational acceleration is g= 9.806 m/s^2.

The effects of density stratification, the Earth's rotation, and viscosity are not directly felt in the momentum equation for $Fr \gg 1$, $Ro \gg 1$, and $Re \gg 1$, respectively. And in section 1.3 we will discuss the values assumed by these parameters in submesoscale dynamics compared to mesoscale dynamics. We can now assert that at submesoscale the buoyancy effects also play an important role because of the strongly influence of the thickness of mixed layer (ML), but the anisotropy of this scale makes submesoscales develop in such a way that the vertical Froude number is $Fr_v = U/NH \sim 1$, where H is a characteristic vertical length scale (G. Boccaletti 2007).

We have already mentioned the importance of ML in submesoscale dynamics, and in the context of the mixed layer instability, that will be treated below, we refer to a dimensionless number that is the *Richardson number* (Ri). Vertical shear can result in turbulence (mixing), and on the other hand vertical stratification stabilizes the mixing. We can use the Richardson number to express this trade off:

$$Ri = \frac{N^2}{(\partial u/\partial z)^2} \tag{1.3}$$

Where the denominator is the square of the vertical shear of the horizontal speed (Talley 2011).

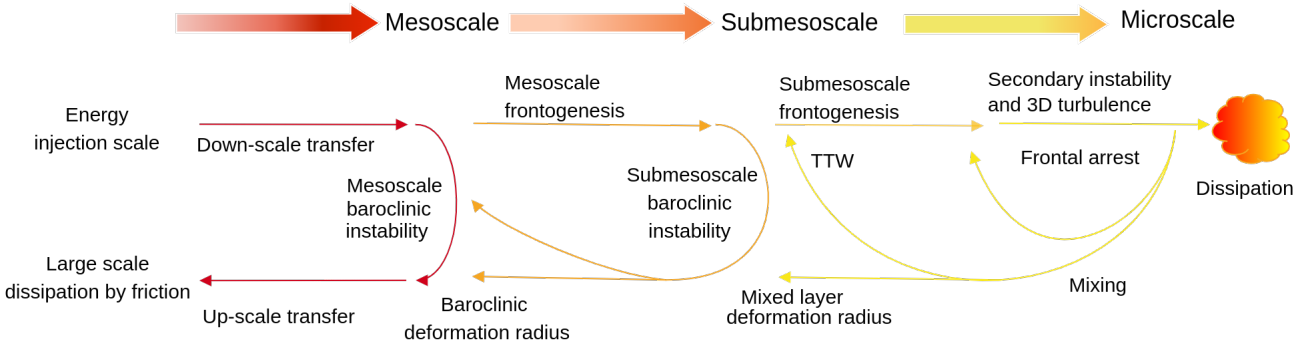

Figure 1.3: Multiscale interactions and oceanic energy transfer. The relative partitioning of energy moving to smaller or larger scales is, at submesoscales. (Adapted from McWilliams 2016)

1.2 Mesoscale dynamic

The mesoscale processes, were discovered during the period of 1973-77, one of the greatest contributions was made by A.R.Robinson, 1932-2009 (Nadia Pinardi 2010).
One of the most important mesoscale features in the ocean are the eddies: these are coherent rotating vortices with horizontal length scale typically of order $O(10km)$ up to $O(100km)$ and timescales typically of week to months (Zhou et al. 2021). The mesoscale eddy field contains coherent vortices as well as a large amount of other structures including filaments and spirals. The mesoscale dynamics of the ocean play a crucial role in determining the circulation patterns of the ocean, and can have significant impacts on a wide range of physical, biological, and chemical processes, including the transport of nutrients, heat, and carbon dioxide, as well as the distribution of marine species and the formation of weather patterns (A. Adcroft 2011). The main regions of formation of the eddies are along the eastern boundaries of the ocean basins, as a manifestations of baroclinic instability of the vertically sheared currents. Eddies form also throughout most of the open-ocean regions (Chelton 2011). Near the equator, eddies give way to fast-moving features called *Kelvin waves*.
In the ocean, vortices are pervasive because ocean is very well approximated by quasi-geostrophic (QG) theory and they are explained by QG turbulence.

Quasigeostrophic theory The mesoscale dynamics in the ocean is described by the QG theory which is an approximation of the geostrophic theory. The geostrophic theory assumes that the flow is exactly parallel to the lines of equal pressure, while the QG theory allows a small deviation from this condition (Cavallini and Crisciani 2012). The

QG theory is more suitable for describing mesoscale vortices that have a certain vertical component (Miracca-Lage et al. 2022).
Briefly, in order to have predictive equations we need to go at the successive order, respect the zero order of the geostrophic equations (Eq. 1.4), in the perturbed expansion of the nondimensionalized shallow water equations

$$\begin{aligned} fv_g &= g\frac{\partial \eta}{\partial x} \\ fu_g &= -g\frac{\partial \eta}{\partial y} \end{aligned} \tag{1.4}$$

where f, g are respectively the Coriolis parameter and the gravitational acceleration module; $\boldsymbol{u_g} = (ug, vg)$ is the geostrophic (horizontal) velocity field and $\boldsymbol{\nabla}\eta$ is the sea level gradient.
From the perturbed equations, through the construction of a vorticity equation one obtains the conservation of a quantity following the geostrophic motion, that is called quasigeostrophic vorticity (Eq. 1.5):

$$\frac{D\Pi}{Dt} = 0, \qquad \Pi = \xi_z + \beta y + \frac{\partial}{\partial z}\left(\frac{f_0}{N^2}\frac{\partial \psi}{\partial z}\right) \tag{1.5}$$

Where $\xi_z = \nabla_h^2 \psi$ is the relative vorticity, βy the planetary vorticity, and the last term is the stretching vorticity, depending on the squared Brünt-Väisälä frequency N^2 that is a measure of seawater stratification.
The solutions of this equation are extremely relevant for the ocean dynamics and led to the predictions of mesoscale features such as the *Rossby waves*.

Quasigeostrophic turbulence In the ocean vortices are pervasive because ocean is very well approximated by quasi-geostrophic and they are explained by QG turbulence. This research field considers thinness of the Earth's ocean (*i.e.* $H/L << 1$), and Earth's rotations (*i.e* $R_o << 1$) and stable stratification; which tend to suppress vertical flow and make 2D horizontal component dominant. The quasigeostrophic equations admit also two conserved quantities (two invariants): one is the total energy integrated over the volume and the other the *enstrophy*, a new quantity proportional to the square of vorticity; with the difference that energy goes to the large scales (*inverse energy cascade*) while the enstrophy goes to the smaller ones (*forward ensotrophy cascade*). This process is called quasigeostrophic turbulence. This is 2D or quasi-2D turbulence and is different from 3D turbulence (Reynolds turbulence) because of this two invariants.
This means that energy accumulates at *large spatial scales* for increasing times and persistent vortices of large amplitude, due to 2D inverse cascade.

1.2.1 Baroclinic Deformation Radius

The Rossby radius of deformation is the horizontal scale at which rotation effects become as important as buoyancy effects, and thus rotation causes a response that is markedly different from the nonrotating case (Gill 1982).
The large scale, almost geostrophic, circulation adjusts to changing wind and buoyancy forcing mainly through *Rossby waves* and *Kelvin waves*.
The Rossby deformation radius is the length scale that distinguishes long and short wavelength Rossby waves. The Rossby radius characterizes the observed mesoscale (eddy) length scales, as well as the spatial decay scale of Kelvin waves: because almost all water flows are unsteady, the gyre-scale flows break up in large eddies.
The two sources of energy instability are the *kinetic energy* and the *potential energy* of the mean flow. Isopycnals must be tilted in order to have accessible potential energy, for baroclinic instability to occur. The instability of sub-mesoscale vortices created in the mixed layer of the ocean is fundamentally one of baroclinic instability working on density fronts within the mixed layer. The fronts are severely inclined isopycnals that are then susceptible to this type of potential energy release. Since the Earth's rotation allows for a mean geostrophic flow with mean tilted isopycnals, baroclinic instability is peculiar to geostrophic flows (Talley 2011).
To summarize; the Rossby radius gives an *energy partition*: short-wavelength geostrophic flow contains mainly kinetic energy, whereas long-wavelength geostrophic flow has most of its energy in the potential form.
The Rossby deformation radius in an unstratified ocean is called the *barotropic Rossby deformation radius*; and is of the order of thousands of kilometers. The Rossby deformation radius associated with the ocean's stratification is called *baroclinic deformation radius*.
The latter is determined linearizing the quasigeostrophic potential vorticity equation about a zero background mean flow. The vertical dependence may be separated from the horizontal and temporal dependencies for a flat bottom. Considering the boundary conditions for the vertical structure (Eq. 1.7), the z-dependent differential equation (Eq. 1.6) thus obtained is equivalent for long, baroclinic gravity waves in a nonrotating, continuously stratified fluid (D. Chelton 1998).

$$\frac{d^2\Phi}{dz^2} + \frac{N^2(z)}{c^2}\Phi = 0 \tag{1.6}$$

$$\Phi = 0 \ \ at \ \ z = 0, \qquad \Phi = 0 \ \ at \ \ z = -H \tag{1.7}$$

A countable collection of increasing non-negative eigenvalues c_m^{-2} and associated eigenfunctions $f_m(z)$ exist. The subscript m denotes the baroclinic mode number.

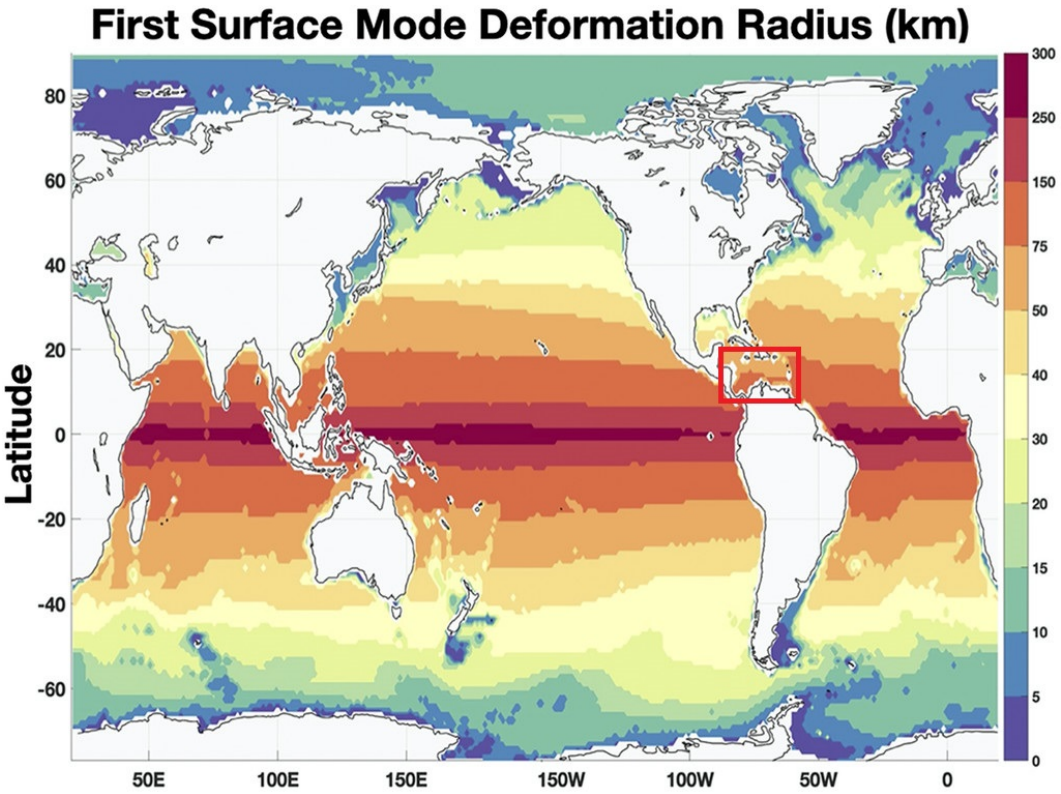

Figure 1.4: First surface mode baroclinic deformation radius. From LaCasce 2020. The region of interest is found in the red box.

Where c_m represents the phase speed of the mode-m gravity waves.
Outside the Tropics the Rossby radius of deformation for mode m is

$$\lambda_m = \frac{c_m}{|f|}. \tag{1.8}$$

Since the Coriolis parameter tends to zero near the equator (where the latitude is smaller than 5°), we consider a modified strain radius:

$$\lambda_m^{EQ} = (\frac{c_m}{2\beta})^2. \tag{1.9}$$

Where $\beta = df/dy$ is the latitudinal variation of the Coriolis parameter.
The effects of stratification and water depth on the mode-m eigensolution are entirely included in the parameter c_m. The vertical length scale associated with the first baroclinic mode is approximately 1000 m, which corresponds to pycnocline depth. In the tropics, the deformation radius for the first baroclinic mode ranges from more than 150 km to roughly 10 km at high latitudes (Fig. 1.4). From the Figure 1.4 we can see that the deformation radius in the Caribbean Sea is between 50 and 75 Km.

1.3 Submesoscale dynamic

When the Rossby numbers are larger (i.e. smaller length scales) the ageostrophic motions become dynamically relevant and are referred as submesoscale currents (SMCs) (Müller 2005).
Submesoscale currents are associated with density fronts and filaments, vortices and topographic wakes at the surface and ocean's interior (Gula et al. 2022).
SMCs have an horizontal scale typically of order $O(100m)$ up to $O(10Km)$, a vertical scale typically of order $O(10m)$ up to $O(1Km)$ and timescales typically of hours to days.
The horizontal scale is larger than the turbulent boundary layer thickness (below which currents are more nearly isotropic), and smaller than the first baroclinic deformation radius (above which currents are geostrophic).
They are distinguished by increased vertical velocities and vorticity, and so submesoscale motions have to be considered 3-dimensional.
The fundamental distinction from the geostrophic mesoscale currents and from the isotropic shear turbulence is a Rossby number and a Froude number that are not, respectively, asymptotically small or asymptotically big. The local Richardson number also can assume intermediate values in SMCs. (McWilliams 2016)
Submesoscales can transfer energy from larger quasi-balanced motions to small-scale three-dimensional turbulence, thereby providing a route to dissipation. In fact balanced eddies are characterized by an inverse energy cascade, and so do not provide a route to dissipation.
As mentioned SMCs have a large vertical velocity, and this leads to large material eddy fluxes by SMCs, that re-distribute water properties, including buoyancy, momentum, heat, freshwater, and biogeochemical tracers. While submesoscale instabilities enhance vertical exchange, they drive an efficient restratification of the upper ocean. They can also have a strong impact in the bottom boundary layer where they generate turbulent mixing and export mixed waters out of the bottom boundary layer (Gula et al. 2022).
The Mixed layer (ML) at the ocean's surface is maintained by convection and wind stress. Submesoscale restratification restricts the depth to which boundary layer turbulence may reach, hence reducing the depth of the ML, which can cause phytoplankton blooms under light-limited situations (John R Taylor 2011). The mixed layer depth (MLD) is also a significant element in determining upper ocean dissolved gas concentrations, the rate of air/sea gas exchange, and hence the ocean's carbon dioxide absorption (John R Taylor 2023). In addition, at the submesoscale, there is a marked asymmetry in the strength of upwelling versus downwelling and anticyclonic versus cyclonic vorticity, with an enhancement of downward velocity and cyclonic vorticity (Fig. 1.5) (Capet

et al. 2008b).

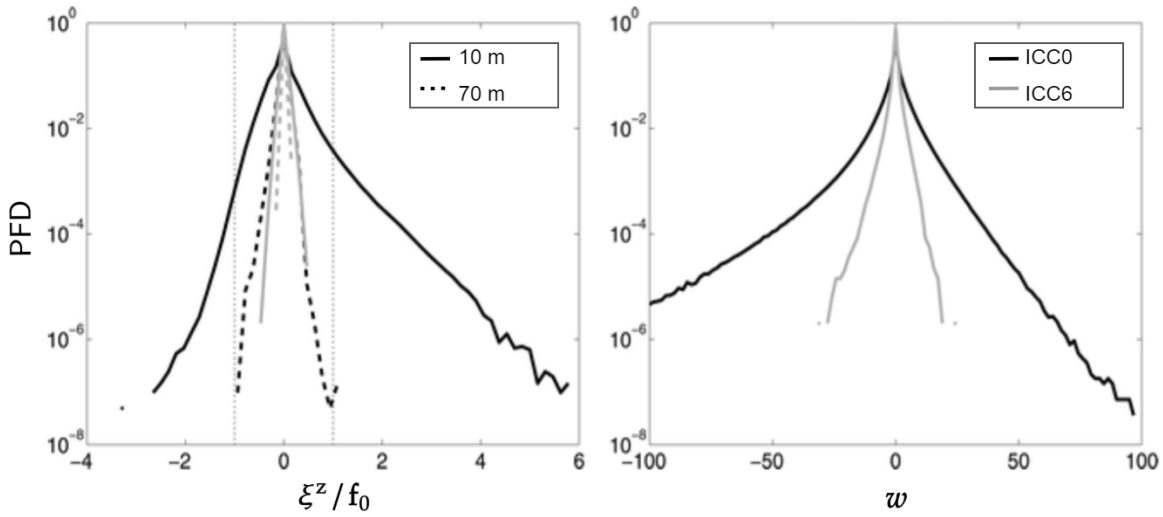

Figure 1.5: Single-point PDFs for (left) ξ_z/f_0 at 10 (solid line) and 70 m depth (dashed line) and (right) w (day^{-1}) at 20 m depth at 0.75 (black lines) and 6 km resolution (gray lines). Adapted from Capet et al. 2008b

1.4 Generation Mechanisms

Submesoscale currents occur on lateral scales of 100 m–10 km in the ocean and are associated with density fronts and filaments, vortices and topographic wakes at the surface and in the ocean's interior.

As mentioned we find submesoscale (SM) surface layer fronts and filaments generated through mixed layer baroclinic energy conversion and submesoscale coherent vortices (SCVs) generated by topographic drag.

We try to identify the main mechanisms of submesoscale generation; this section is mainly based on the papers by Srinivasan et al. 2017 and McWilliams 2016.

Submesoscale currents are generated and influenced by a number of different processes, which are summarized below and and sketched in Fig.1.6.

1.4.1 Mixed layer instability

The formation of SM features generally occurs at the ocean's top and bottom. The production of mixed layer eddies (MLEs) and fronts is caused by the mixed layer instability of the poorly stratified, due to efficient vertical buoyancy mixing by boundary layer turbulence, surface mixed layer. MLEs act to continuously restratify the surface

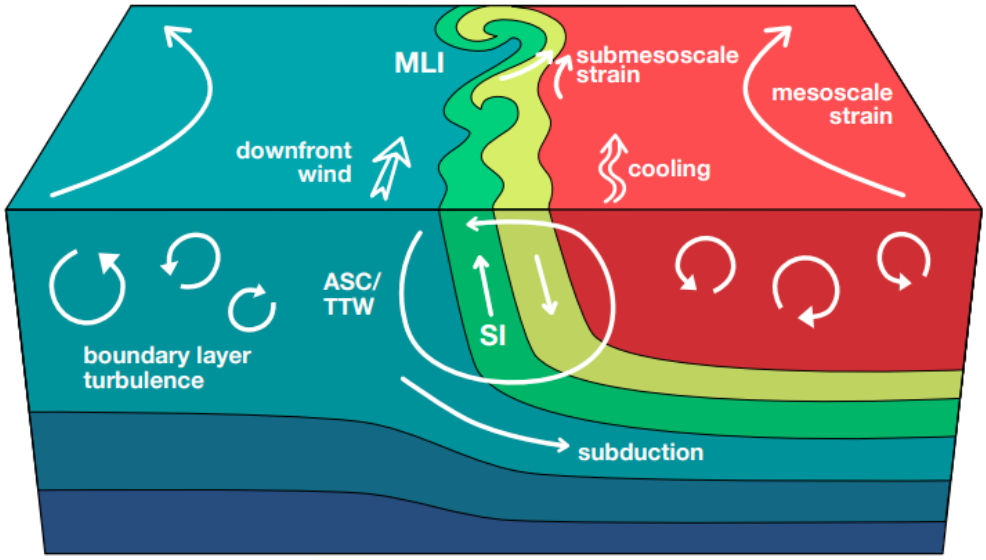

Figure 1.6: Idealized depiction of various submesoscale processes discussed in this subsection. Convergent mesoscale strain drives frontogenesis. Surface cooling or a downfront wind can make the front unstable to symmetric instability (SI). The frontogenetic strain and vertical mixing drive an ageostrophic secondary circulation (ASC), which, in the latter case, can be described as a turbulent thermal wind (TTW) balance. Submesoscale eddies develop through mixed layer instability (MLI) which drives further frontogenesis and localizes boundary layer turbulence and subduction of water into the thermocline. (From Gula et al. 2022)

mixed-layer. Mixed layer instability is an upper-ocean equivalent of the classical interior baroclinic instability (Fig. 1.7) (TWN Haine 1998). Submesoscale currents are generated with horizontal scales around the deformation radius $l_s \sim N_s h_b/f \sim 1km$, which is typically smaller than the baroclinic deformation radius (horizontal scales for the generation process of mesoscale currents) because the stratification $N_s \sim 10^{-3}s^{-1}$ is smaller and also the thickness ($h_b = 10^2 m$).

In this context, MLI can be viewed as baroclinic instability in the limit when $Ri, Ro \sim 1$, both characteristic of submesoscales in the mixed layer (Gula et al. 2022).

MLEs are stronger for bigger horizontal buoyancy gradients ($\nabla_h b$) and deeper mixed layers (h_b), and they are a key factor for the increase in SM activity throughout the winter.

MLI draws its energy from the available potential energy associated with horizontal buoyancy gradients and converts it to kinetic energy.

There are two possible non-linear energy cascades: an inverse energy cascade towards larger scales, typical of geostrophic turbulence, and a forward energy cascade driven by

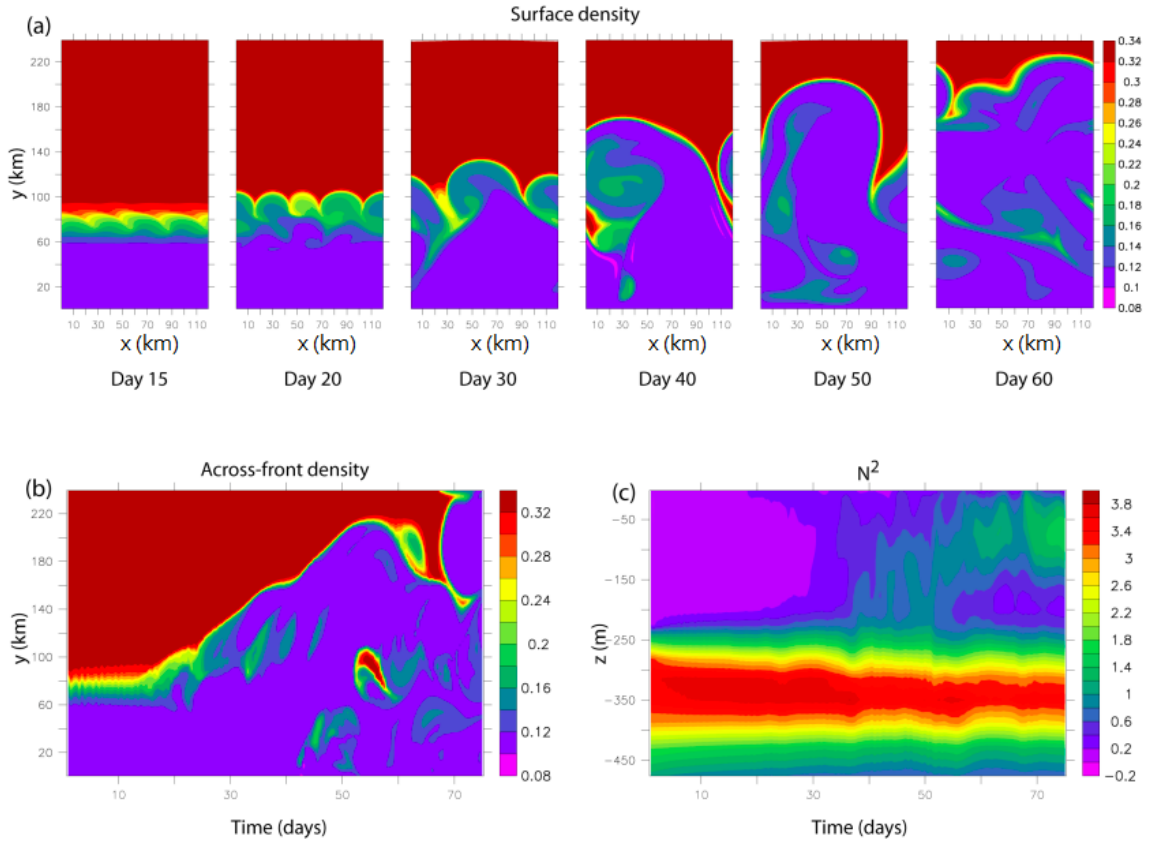

Figure 1.7: (a) Time sequence of the surface density anomaly showing the evolution of MLI in an idealized simulation of a front. (b) Evolution of the across front density and (c) of the vertical stratification along a midchannel section. (Adapted from Gula et al. 2022)

ageostrophic motions and loss of balance.

1.4.2 Frontogenesis

Frontogenesis, often associated with atmospheric settings, occurs when the mesoscale eddy strain field in the mixed layer increases due to the action of a dynamically active ageostrophic secondary circulation (ASC), and also increases the horizontal density or temperature gradients resulting in the formation of fronts and filaments, common sub-mesoscale features, visible at the ocean surface in observations and models.

Surface-layer frontogenesis generates an ageostrophic secondary circulation due to a large-scale and mesoscale lateral strain. The secondary circulation tilts the isopycnals towards the horizontal, resulting in restratification. Restratification is a process where warmer and lighter waters lay over colder and denser waters and also generates intense vertical velocities (LN Thomas 2008).

In the case of fronts, two water masses with different densities meet, resulting in the formation of an overturning cell with upwelling and surface divergence on the lighter side and downwelling and surface convergence on the denser side. For filaments instead, a water mass is embedded in a lighter one, resulting in the establishment of two overturning cells and along-side flows in both directions (McWilliams 2016).
The flow configurations of strain-induced frontogenesis are sketched in Fig.1.8.

While frontogenesis can occur independently of mixed layer instability, the two pro-

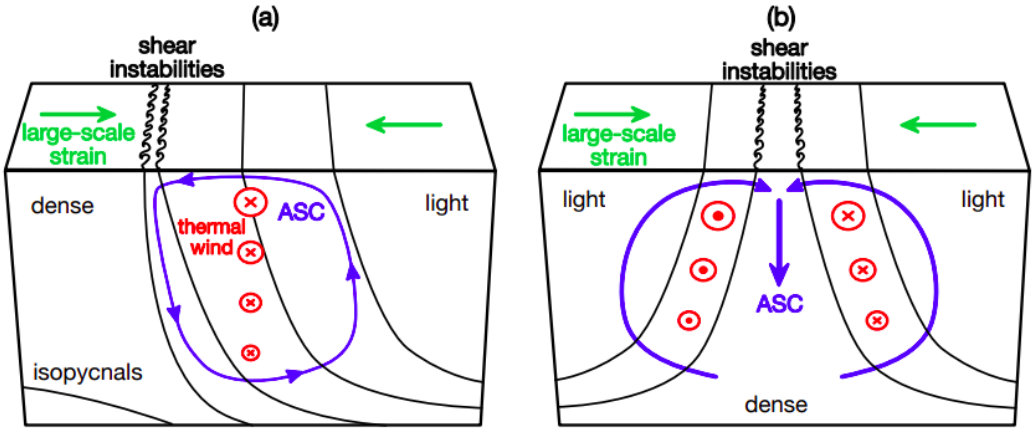

Figure 1.8: Sketches of surface-layer frontogenesis caused by a large-scale deformation flow for front (a) and dense filament (b) configuration; from McWilliams 2016

cesses frequently coexist, with secondary frontogenesis occurring at the borders of MLEs.

1.4.3 Turbulent thermal wind

Additionally, unlike the preceding inviscid methods of SM creation and maintenance, a nonconservative SM process, referred to as the turbulent thermal wind (TTW) balance, is related with secondary circulation and frontogenesis owing to turbulent vertical momentum mixing in fronts and filaments. TTW is a composite generalization of geostrophic, hydrostatic (thermal wind) balance, and Ekman boundary-layer balance. When the vertical eddy viscosity associated with surface boundary layer turbulence is big these two types of circulation are coupled, and an ageostrophic secondary circulation arises around the submesoscale structure. In other words (u,w) shapes in two-dimensional configuration (see Fig.1.8) will have the same shapes in TTW as they do in strain-induced frontogenesis. This further implies that frontogenesis can occur because of TTW in association with the surface convergence lines on the dense side of

a front and in the center of a filament.
All of these processes are characterized by submesoscale generation from the conversion of surface-layer available potential energy (from the mesoscale) to kinetic energy, implying restratification flux, in a further downscale flux among Submesoscale Coherent Structures (SMCs).

1.4.4 Topographic wakes

We also present a different route to generating submesoscale eddies: the interaction of mean and mesoscale currents with topography, which generates wakes: *topographic wakes*.
The basic mechanism sees wakes exhibit vorticity by bottom drag in the bottom boundary layers, the boundary separation of high-vorticity sheets and subsequent barotropic or centrifugal instability that makes separated wakes roll up into both mesoscale or SM coherent vortices (SCVs), depending if the Rossby number Ro is small or $O(1)$.
The wakes and their evolution are fully three-dimensional due to non-uniformity in z of both the incoming flows and the boundary shape.
SCVs are gradient wind balanced (i.e., including the cyclostrophic force), as opposed to the usually geostrophically balanced mesoscale eddies. Oceanic currents can also separate behind an island, as well as along a continuous coast because of the changing wind stress curl, boundary curvature away from the downstream flow direction, and an internally generated adverse pressure gradient (M. Jeroen Molemaker 2015).

1.5 Topographic wakes and Island Mass effect

In the following sections, we try to give a general picture of topographic wakes and of Current-Island Interactions, based on the article by De Falco et al. 2022 and McWilliams 2016.
In the Ocean wakes occur in the same phenomenological sequence of fluid dynamic (horizontal flow past a vertical cylinder): generation of vertical vorticity at the BL, horizontal separation of the flow, and creation of an internal zone with large lateral shear; that produces instability and amplification of the lateral shear and roll-up into long lived vortices.
In the ocean with rotation and stratification (Ro and Fr are not large), the non uniformity of the flow and the boundary shape, makes the wakes fully 3D.
This phenomenon can be viewed within the submesoscale range, because, even in an idealized rotating and stratified simulation the wake shear layers are quite thin (if Re is large).
When a current meets a slope, as the vertical velocity goes to zero, vertical vorticity is

generated in the BBL. Slope boundary currents separate from the boundary and go into the stratified interior with their strong anomaly of vertical vorticity, producing shear instabilities: wakes break up into vortices.
Currents impinging on the bathymetry upstream of an island can raise the isotherms and cause vertical transport, the increased vertical shear caused by the combination of strong incoming currents and bottom friction can improve vertical mixing and allow water from the thermocline to enter the mixed layer.
Around small islands is known that the Net Primary Productivity (NPP) is increased, this phenomenon is known as Island Mass Effect (IME): the upwelling and mixing increase the input of nutrients in the euphotic layer[1], favoring biological productivity, while also lowering surface temperature. The physical processes that cause this occurrence might vary, but upwelling mechanisms in an island's lee include the formation of cyclonic eddies caused by barotropic or baroclinic instabilities, as well as flow divergence.
We need to understand the unique blend of factors driving each IME island because many of the smaller or more remote islands have never been researched.
The main physical processes responsible for the IME are: Current-Island Interactions, Vertical Mixing in the Upper Ocean, Wind-Island Interactions and Oceanic and Atmospheric Processes Interactions.

1.5.1 Current-Island Interactions

The resulting circulation related to an incoming currents, refers to the classical problem of a cylindrical obstacle in a horizontal fluid. In the present study we are dealing with weak incoming currents and/or very small islands compared to the local Rossby deformation radius, thus referring to Re values of up to a few tens of metres (Fig.1.9 (A)): the oceanic flow away from the obstacle is laminar and lateral friction causes two stationary eddies with opposing signs to form just behind the obstacle. If the islands are small enough (Fig.1.9 (B)), the Reynolds number is small despite the speed of the currents and wake-like signals are produced by the interaction between the incoming currents and the island. The island induced flow separation and give rise to localized upwelling: the pair of horizontal surface jets behind the island entrains water from the lee side and causes surface divergence in the wake fed by a deeper returning current. The upwelling velocity (Eq. 1.10) is proportional to the current speed variation and inversely proportional to the distance over which the change occurs, which is associated to the diameter of the island.

[1]The euphotic zone is the layer closer to the surface that receives enough light for photosynthesis to occur (Kingsford 2023)

$$w(-h) = \int_{-h}^{0} \frac{\partial w}{\partial z} dz = \int_{-h}^{0} (\frac{\partial u}{\partial x} + \frac{\partial v}{\partial y}) dz \tag{1.10}$$

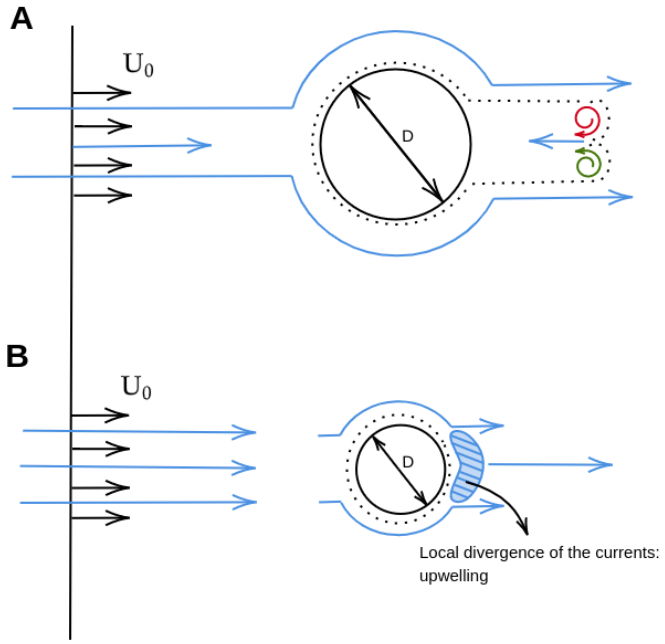

Figure 1.9: Ocean circulation in the wake of a circular island for (**A**) O(10) Reynolds number and (**B**) wake-lee upwelling. Green and red spirals illustrate positive and negative vorticity in the ocean's upper layer, respectively. Upstream currents are the black arrows (U_0) on the left side of a D-diameter obstacle. The flow streamlines are shown by blue arrows (De Falco et al. 2022).

Wind-Island Interaction:

In this case we have weather related consequences: terrain induced circulation affects precipitations and clouds, and the physical barrier induces instability.
The control parameter in this case is the *Froude number* ($Fr = U_{MABL}/Nh$) where U_{MABL} is the upstream wind averaged within the Marine Atmospheric Boundary Layer (MABL) and h is the height of the mountain. A low Fr number ($Fr \sim 0.5$) leads to the creation of two large counter rotating vortices on the lee side of a mountain, while a higher Fr number ($Fr \sim 1$) leads to a larger wake and more turbulent. If the Fr number is very high (low island) the wake is very large compared to the island and is characterised by very turbulent flow.

The wind speed is also linked to the ML depth: a weaker wind entails a ML shallower with an intense surface warming, there is less vertical exchange and so a decrease in the NPP.

1.5.2 Ocean and atmosphere Processes interactions

The processes emerging from the interaction between currents and bathymetry features and between wind and topographic features are coupled: the atmospheric circulation injects vorticity into the ocean that favours the generation of eddies by wind stress despite weak background currents. This coupled processes give rise to surface temperature anomalies, forcing local upwelling or downwelling.

1.5.3 Vertical mixing

The fluctuations of the wind stress, the tidal forcing and the lee wakes can perturb the interface and generate internal waves. Internal waves entrain cold and nutrient rich waters in to the upper ocean, propagating at the base of ML. The break of this internal waves is a great source of vertical mixing, they can indeed propagating inshore depending if there is a gradual topography slope. Vertical mixing can occur also by bottom friction, leads to strong vertical shear (reducing horizontal currents), that can lead to unstable flows and enhance vertical mixing, with entertainment of deep cold water in the mixed layer. Vertical mixing enhancement caused by internal waves or bathymetry interaction results in a nearly symmetric imprint.

1.6 Thesis objective

In this study, we aim to investigate the characteristics of submesoscale structures in the Caribbean Sea with a particular focus on the Chibcha channel area (western Caribbean Sea) where we study the SM features generated through interaction of mesoscale flow with the topographic features.
We conducted short-term high-resolution dynamically downscaled projections from February 2nd to February 28th, 2021, using the SURF numerical platform (Structured and Unstructured grid Relocatable ocean platform for Forecasting) based on the NEMO code.
We generated a nested model, called "child", with a resolution of $1/36^\circ$ using initial and lateral boundary conditions information from the coarser-grid global model at $1/12^\circ$ resolution, called "parent", provided by the Copernicus Marine Environment Monitoring Service (CMEMS). First, we analyze the results obtained from the coarser-grid parent model, and then we compare these results with the finer-grid child model results. To study the topographic SMs in our region of interest, we conduct several sensitivity experiments varying the depth and size of a small island called Petrel Island, situated in the western Caribbean Sea at coordinates 15.85°N 78.66°W. This island has a surface area of approximately 11x3 kilometers and is not resolved in either the parent or child grid.
Next, we analyze how these configurations influence the dynamics in the specific region and what role they play in the development of submesoscale features.

In terms of thesis structure, Chapter 1 is an introduction chapter on mesoscale and submesoscale dynamics and the function of islands in submesoscale dynamics. The second chapter gives an overview of the areas of interest, the datasets used, and the numerical model used. In Chapter 3, we explore mesoscale patterns over the whole region using information from the "parent" model, and we highlight submesoscale phenomena identified in the Chibcha channel using high-resolution simulations. In this context, a comparison of the "parent" and "child" models is made, emphasizing the benefits of using a high-resolution downscaling strategy. The fourth chapter focuses on performing sensitivity tests by varying the size and depth of a specific island in order to understand the effects on submesoscale dynamics. Finally, in Chapter 5, we present the conclusions drawn from our research efforts.

CHAPTER 2

Model Setup

In this work, we implement a nested high-resolution ocean model in the Caribbean Sea at 1/36° horizontal resolution using the structured grid component of the SURF platform based on the NEMO code. The initial and lateral boundary conditions for the nested models were extracted from the large-scale CMEMS-global analysis daily mean product at 1/12° horizontal resolution. A 27-day simulation have been produced from 2 February 2021 at 00:00 until 28 February 2021 at 24:00.
In this chapter we describe the simulations features, including the NEMO numerical ocean model, the SURF platform, the simulation region and the datasets exploited.

2.1 NEMO-OCE

NEMO, which stands for "Nucleus for European modeling of the Ocean," is an advanced modeling framework designed for ocean and climate research and prediction services. It has been developed by a consortium of European partners in a sustainable manner, ensuring its long-term viability and effectiveness (see `https://www.surf-platform.org/`).
The system consists of three principal engines: NEMO-OCE, for modelling the blue ocean (thermo)dynamics and solving the primitive equations; NEMO-ICE, for modelling the white ocean (thermo)dynamics, NEMO-TOP, for modelling the green ocean using oceanic tracers transport and biogeochemical processes We will use in this work

the NEMO-OCE component.

2.1.1 Primitive Equations for the Ocean

NEMO-OCE focuses on the study of ocean dynamics and thermodynamics. It accomplishes this by solving the three-dimensional primitive equations, derived in Appendix A, that describe the behavior of the ocean.
Although the equations established in A already contain numerous simplifying approximations, they are still too complicated for our purpose. In fact the ocean can be described to a good approximation by 3D primitive ocean equations with *free surface* under *hydrostatic*, *incompressibility* and *Boussinesq* approximations, along with turbulence closure schemes and a non-linear equation of state, which combines the two active tracers (temperature and salinity) with the fluid velocity.
Below I will briefly describe these approximations:

- *Incompressibility approximation*: the continuity equation under the incompressibility approximation takes the following form, $\boldsymbol{\nabla} \cdot \boldsymbol{u} = 0$.

- *Boussinesq approximation*: assumes that the density variations of a fluid are small compared to its mean density.

- *Hydrostatic approximation*: the pressure within the fluid is primarily determined by the fluid's depth or height, rather than other variables like velocity or acceleration. This relationship is described by the equation $\frac{\partial p}{\partial z} = -\rho g$. This equation implies that changes in pressure within the fluid are mainly influenced by variations in depth, which in turn affect the density of the fluid. The density changes can occur due to two factors: momentum exchanges at the air-sea interface, which are influenced by the boundary conditions and interactions with the atmosphere, and thermodynamic processes that alter the density and subsequently the pressure within the fluid.

- *Turbulence closure schemes*: the one that we use in this work is the Reynolds-averaged Navier-Stokes (RANS) model. RANS models average out the turbulent fluctuations, providing a simplified solution to the equations of motion. This method is described in detail in Appendix B.

We also consider the Earth as a sphere, assuming locally vertical gravity, neglecting the ocean depth compared to the Earth's radius, and disregarding the variation of Coriolis terms with latitude.

As an orthogonal reference system, we consider $(\hat{\mathbf{i}}, \hat{\mathbf{j}}, \hat{\mathbf{k}})$, aligned with the Earth's coordinates, $\hat{\mathbf{k}}$ represents the upward direction, while $(\hat{\mathbf{i}}, \hat{\mathbf{j}})$ form a horizontal vector

tangent to geopotential surfaces. The unit vectors are respectively associated to longitude, latitude and depth (x, y, z axes).
The equations describing the system are (reflecting order in the system 2.1) the continuitity equation, the two momentum balance equations, the hydrostatic balance, the heat and salt conservation equations and finally the equation of state:

$$\begin{cases} \boldsymbol{\nabla} \cdot \boldsymbol{u} = 0 \\ \dfrac{\partial u}{\partial t} + \boldsymbol{u} \cdot \boldsymbol{\nabla} u - fv + f^* w = -\dfrac{1}{\rho_0}\dfrac{\partial p}{\partial x} + (\dfrac{A_h}{\rho_0} + \nu)\boldsymbol{\nabla}_h^2 u + (\dfrac{A_v}{\rho_0} + \nu)\dfrac{\partial^2 u}{\partial z^2} \\ \dfrac{\partial v}{\partial t} + \boldsymbol{u} \cdot \boldsymbol{\nabla} v + fu = -\dfrac{1}{\rho_0}\dfrac{\partial p}{\partial y} + (\dfrac{A_h}{\rho_0} + \nu)\boldsymbol{\nabla}_h^2 v + (\dfrac{A_v}{\rho_0} + \nu)\dfrac{\partial^2 v}{\partial z^2} \\ \dfrac{\partial p}{\partial z} = -\rho g \\ \dfrac{\partial \theta}{\partial t} + \boldsymbol{u} \cdot \nabla \theta = (K_h + K^*)\nabla_h^2 \theta + (K_v + K^*)\dfrac{\partial^2 \theta}{\partial z^2} \\ \dfrac{\partial S}{\partial t} + \boldsymbol{u} \cdot \nabla S = (K_h^s + K_S^*)\nabla_h^2 S + (K_v^s + K_S^*)\dfrac{\partial^2 S}{\partial z^2} \\ \rho = \rho(\theta, S) \end{cases} \tag{2.1}$$

The variables involved above are velocity ($\mathbf{u} = (u, v, w)$), potential temperature (θ), salinity (S), pressure (p) and density (ρ).
The reference denity is written as ρ_0, $f = 2\Omega sin\theta$ is the Coriolis parameter at a fixed latitude θ and $f^* = 2\Omega cos\theta$. ν is the kinematic viscosity of the water, K^* and K_S^* are the molecular diffusivity of temperature and salinity respectively. A_v and A_h are respectively called vertical and horizontal turbulent viscosity coefficients. The subscript h stands for the horizontal vector, i.e. projected on ($\hat{\mathbf{i}}$, $\hat{\mathbf{j}}$); and v stands for the vertical vector, i.e. projected on ($\hat{\mathbf{k}}$).

2.2 SURF structured grid component

The Structured and Unstructured grid Relocatable ocean platform for Forecasting (SURF), (F. Trotta 2016) provides a numerical platform for forecasting hydrodynamic and thermodynamic fields at high spatial and temporal resolutions. SURF is designed to rapidly deploy a nested high-resolution numerical model into larger-scale ocean forecasts, and includes multiple nesting capabilities (i.e., consecutive nested models can be implemented with increasing grid resolutions), starting with the first nesting in a large-scale ocean model and reaching horizontal grid resolutions of a few hundred metres. For each nesting, the parent coarse-grid model provides the initial and lateral boundary conditions for the child components.

Downscaling allows not only to increase model resolution but also to include geo-

metric features of the coastal areas that affect the flow field, the use of higher resolution bathymetry and the incorporation of more processes such as tides and specific parametrizations in the domain of interest (F. Trotta 2021). The physical processes in the open ocean are driven by the so-called energy cascade and occurs at several time and spatial scales depending on the location, the magnitude of the forcing and the stratification of the water column. In the marginal seas the bathymetric constrain and the freshwater inputs become relevant and can modify the circulation both at regional scale and at larger scale. An adequate representation of these processes should rely on numerical model capable to span between different spatial scales (Maicu et al. 2021).

SURF has been implemented in the Caribbean Sea using initial and boundary conditions from the open and free-access general circulation model systems available in the Copernicus Marine Environment Monitoring Service online catalogue.
We also study the vertical structure of the ocean in this region, we can distinguish a three-layer vertical structure in the ocean represented by the mixed layer, the thermocline and the deep layer. This division is due to the force of gravity that fell the difference in density of the water masses. The upper part is divided from the deep layer thanks to the thermocline, the region of rapid change in temperature.

The structured grid component of the SURF platform is based on the finite differences hydrodynamic NEMO-OCE code (v3.6).
The Nemo model uses the Arakawa C grids for spatial discretization, with the state variables defined on the staggered grid: the scalar field (temperature T, salinity S, pressure p, density ρ) are defined at the centre of each grid volume; the zonal, meridional and vertical component of the velocity field are shifted by half a grid in the respective direction so they are defined at the edges of the grid volume (see Fig.2.1). For the grid points distribution, in the horizontal direction, the model employs a rectangular (or latitude-longitude) grid in a spherical coordinate system.
The type of vertical grid used in SURF corresponds to geopotential z-coordinate levels, with partial bottom cell representation of the bathymetry; that includes five free parameters: $z(k) = h_{sur} - h_0 - k - h_1 log[cosh((k - h_{th})/h_{cr})]$.
Where the coefficients h_{sur}, h_0, h_1, h_{th} and h_{cr} are free parameters to be specified. h_{cr} represents the stretching factor of the grid and h_{th} is approximately the model level at which maximum stretching occurs. The layers are distributed along the water column, with appropriate thinning designed to better resolve the surface layer (see Fig.2.2). Partial cell parameterisation was used (i.e. the bottom layer thickness varied as a function of position) in order to fit the real bathymetry.

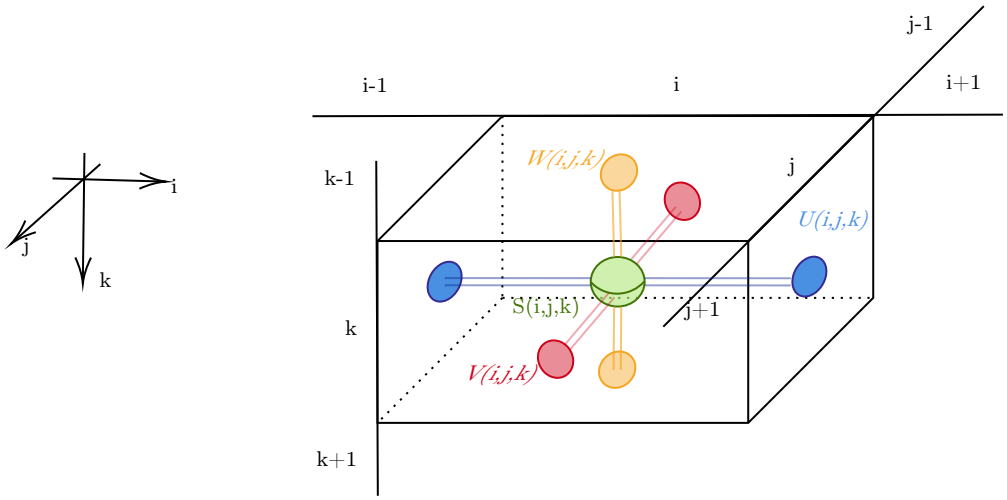

Figure 2.1: The NEMO ocean model employs a staggered Arakawa C-grid. S denotes scalar points that define scalar numbers; U, V, and W denote vector points that define the three velocity components. Indexes (i,j,k) represent longitude, latitude, and depth grid indexes, respectively.

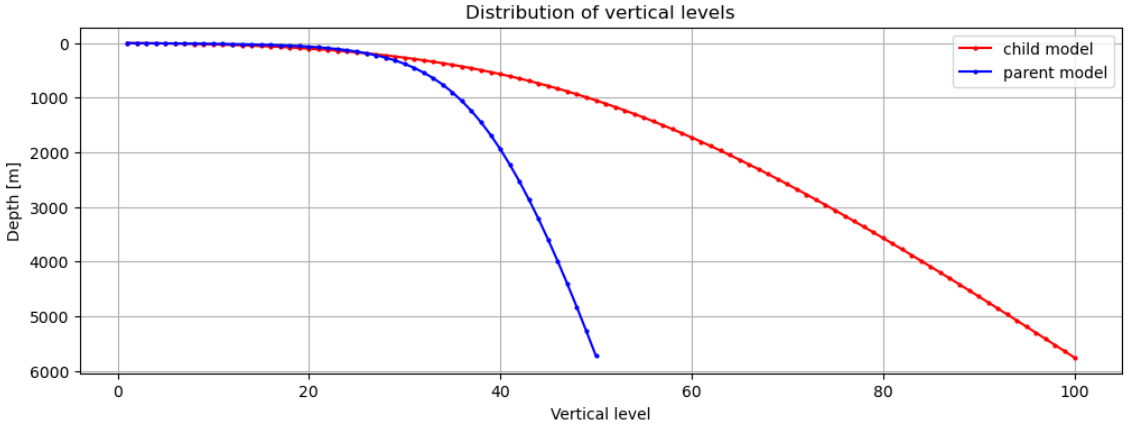

Figure 2.2: Distribution of vertical levels in child and parent models.

Regridding is the process of changing the grid to remap the input fields on the child grid. This phase will generate the surface forcing, initial and open lateral boundary condition datasets on the child grid.

The problem to be solved is an Initial-Boundary (surface boundary conditions, bottom boundary conditions, lateral open and close boundary conditions) Value (IBV) Problem. The ocean fields needed for the initial conditions and ocean boundary conditions are the Potential Temperature, the Salinity, the Sea surface height, the Zonal and Meridional Velocity.

From these data we then extract the data along the selected boundary needed for the open boundary conditions (BC) in Nemo. The Monotonic Upstream Scheme for Conservation Laws (MUSCL) was used for the tracer advection and the Energy and Enstrophy conservative (EEN) scheme was used for the momentum advection . No-slip conditions

on closed lateral boundaries were applied and the bottom friction was parameterised by a non linear function. To evaluate the surface heat balance, atmospheric fluxes were computed through the MFS bulk formulation (D Pettenuzzo 2010).
Two different numerical algorithms are used to treat open BC; the Flather scheme for barotropic velocity and the Flow Relaxation scheme for baroclinic velocities, active tracers and SSH. In order to preserve the total transport after interpolation, an integral constraint method was imposed (N. Pinardi et al. 2003). We can also add to the barotropic velocity the Tidal Potential Forcing at the lateral open boundaries.

To specify we can provide the data for the surface BC: 10 m zonal and meridional wind, 2m Air Temperature, 2m Dew Point Temperature, Total Cloud Cover, MSL Pressure and the Total Precipitation. Now we need the Bathymetry and the Coastline as input datasets to build the child 3D meshmask. After having manipulated the source bathymetry for example smoothing out small-scale variations this product has to be interpolated on the child T-grid. The input ocean fields available on CMEMS are on regular curvilinear spherical grid non-staggered; and the next step is the one of initial data regridding (extrapolation and interpolation), which generates the bottom topography, surface forcing and the initial and open lateral boundary conditions datasets on the child grid. It's important to note that the parent coarse resolution model only provided the total velocity field, the interpolated total velocity field into the child grid was split into barotropic and baroclinic components (F. Trotta 2017). And two different time steps are used to integrate this two different modes (time splitting technique): the fast barotropic mode is integrated with a small time step instead the slow baroclinc mode with a larger time step (120 s).

The model time stepping environment used in NEMO is a three level scheme in which the tendency terms of the equations are evaluated either centred in time, known as the leapfrog method associated with a Robert–Asselin time filter, for momentum and tracer advection, pressure gradient, and Coriolis terms. Either forward, or backward in time depending respectively for horizontal and vertical diffusion terms.
We have to provide the time step, that has to be limited by the Courant-Friedrichs-Lewy stability condition. So the time step is limited by the definition of the space grid; and allows us to ensure that the information does not propagate for more than one cell per time step:

$$c = \frac{|v|\Delta t}{\Delta x} \leq c_{max} \sim 1. \tag{2.2}$$

We can esplicitally resolve scales bigger of the effective grid resolution, so the unresolved scale processes must be incorporate with a subgrid-scale parametrization. To close the eqs. the effects of smaller scale motions must be represented entirely in terms of large-scale patterns (closure problem). These effects appear in the equations as the divergence of turbulent fluxes (of momentum, temperature and salinity). A common

turbulence closure model is the eddy-viscosity model which assumes that turbulent flux of momentum is proportional to mean-velocity gradient $[-\rho\bar{u}\bar{v} = \mu_t \frac{\partial U}{\partial y}]$ where μ_t is the eddy viscosity coefficient. The same can be done for the tracers equations via eddy diffusivity coefficient. Due to the strong anisotropy between the lateral and vertical motions the parameterisation of small-scale physics for the momentum and tracers equations are divided into a lateral and vertical component. The horizontal eddy diffusivity and viscosity coefficients are parameterized as a function of the parent coarse resolution model. The vertical eddy viscosity and diffusivity coefficients are computed following the Pacanowsky and Philander's Richardson number-dependent scheme (F. Trotta 2021) following the formulae:

$$A_V^T = \frac{A_{ric}}{(1 + aR_i)^n} + A_b^{vT} \tag{2.3}$$

and

$$K_V^T = \frac{A_{ric}}{(1 + aR_i)} + K_b^{vT} \tag{2.4}$$

where R_i is the local Richardson number (i.e. the ratio of stratification to vertical shear).

2.3 Case of study: Caribbean sea

By implementing the downscaling process, the child model is rendered significantly more refined compared to its parent counterpart, exhibiting a three-fold increase in resolution. Tthe transition occurs from a coarser global Ocean General Circulation Model (OGCM) with a resolution of $1/12°$ ($\sim 9km$), provided by the Copernicus Marine Environment Monitoring Service (CMEMS). to a more detailed nested model with a resolution of $1/36°$ ($\sim 3km$), achieved through NEMO-based SURF platform, (1:3 grid ratio with the parent).
Fig.2.3 shows an image of bathymetry in the Caribbean Sea, with the names of the main locations superimposed on it.
The parent and children model setup and the model parameters of the experiment are listed in Tab.2.1.

2.3.1 Initial and boundary conditions

The initial and lateral boundary conditions for the ocean are sourced from the Copernicus Marine Environment Monitoring Service (CMEMS, Le Traon et al. 2019). Specifically, we make use of the CMEMS-global analysis and forecast daily mean product (GLOBAL_ANALYSIS_FORECAST_PHY_001_024) to obtain temperature, salin-

ity, sea surface height, and total velocity fields. This model is based on a tripolar grid, then redistributed on a regular grid, with a horizontal resolution of 1/12° and consists of 50 vertical levels spanning from 0 to 5500 meters. It's provided by the Operational Mercator global ocean analysis and forecast system at 1/12° degree (Law Chune et al. 2019).

2.3.2 Surface Boundary Condition

Surface Boundary Conditions are obtained from ERA5, created by the Copernicus Climate Change Service (C3S) at ECMWF, represents the fifth generation of ECMWF atmospheric reanalysis, encompassing the global climate from January 1940 until the present. It offers hourly estimations for numerous atmospheric, land, and oceanic climate variables. The dataset spans the entire Earth on a 30km grid and utilizes 137 levels to depict the atmosphere, ranging from the surface up to an altitude of 80km. Within ERA5, uncertainties are incorporated for all variables, albeit at reduced spatial and temporal resolutions. The generation of ERA5 involves the integration of extensive historical observations through advanced modeling and data assimilation systems to generate global estimates (see ECMWF-ERA5 website[1]).

2.3.3 Coastline

The $GSHHS\_h\_L1$ coastline system, short for "Global Self-consistent, Hierarchical, High-resolution Shoreline", is a comprehensive dataset that offers highly precise and detailed information about the Earth's coastlines, rivers, lakes, and islands. It is constructed by combining various data sources, including satellite imagery, maps, and other geographic data. The dataset is organized in a hierarchical structure, with multiple levels of resolution, enabling users to access different levels of detail based on their specific needs.

Geography data are in five resolutions: crude(c), low(l), intermediate(i), high(h), and full(f). Shorelines are organized into four levels: boundary between land and ocean (L1), boundary between lake and land (L2), boundary between island-in-lake and lake (L3), and boundary between pond-in-island and island (L4).[2] In this work we use the $GSHHS\_h\_L1$ coastline system.

2.3.4 Bathymetry

General Bathymetric Chart of the Oceans (GEBCO) organization provide the bathymetry dataset: $GEBCO\_2014$, the version employed here, a continuous terrain model for

[1] https://www.ecmwf.int/en/forecasts/dataset/ecmwf-reanalysis-v5

[2] see NOAA website: https://www.ngdc.noaa.gov/mgg/shorelines/gshhs.html

oceans and land at 30 arc-second interval (∼ 830 m) (Becker et al. 2009).
The bathymetry in the entire domain and the region of interest is shown in Fig.2.3

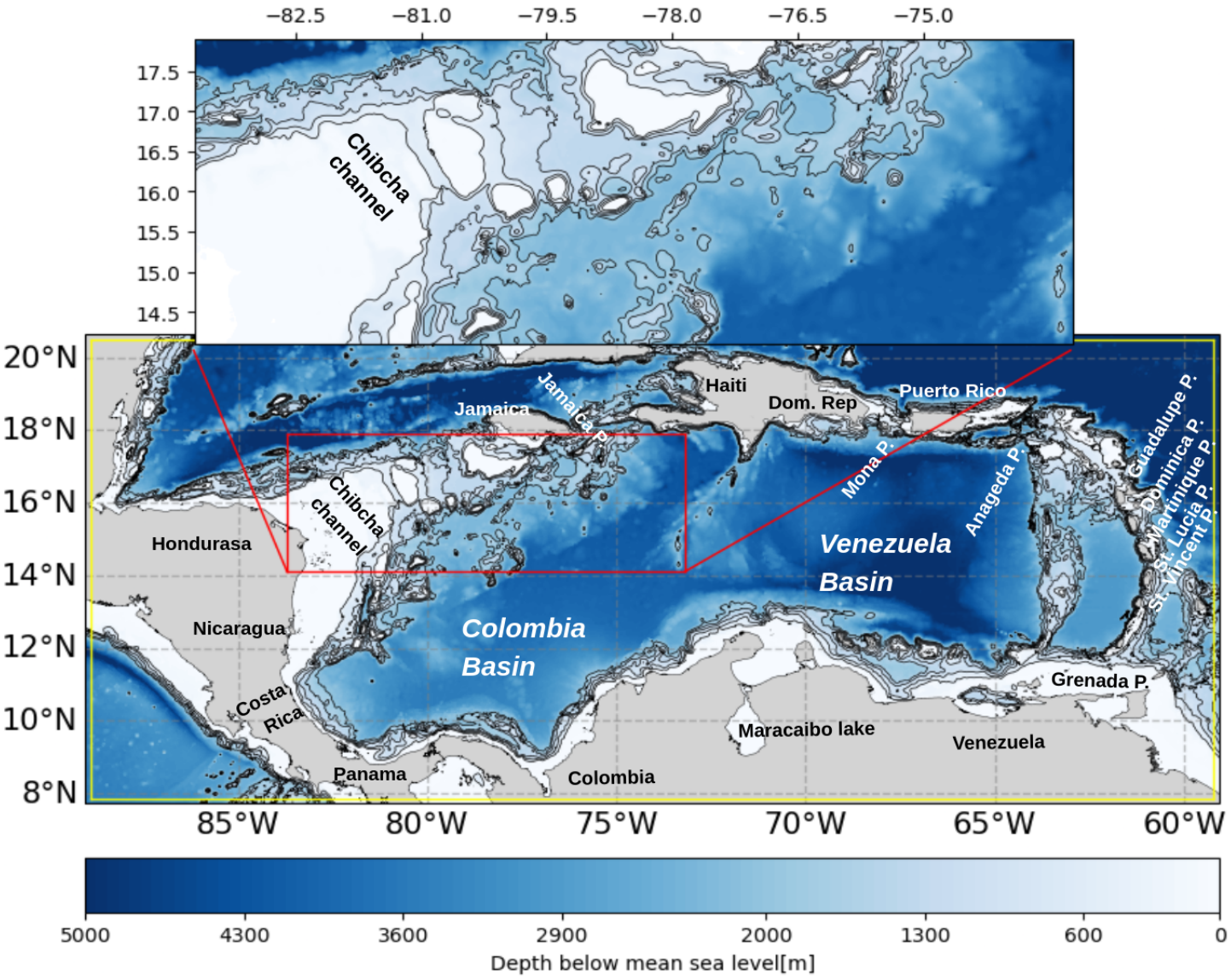

Figure 2.3: Bathymetry dataset *GEBCO_2014* used in the simulation, the area enclosed by the red box represents the area of interest in which we will focus in the second part of our work. The area enclosed by the yellow box represents the domain of the child model. "P." is the abbreviation of "Passage".

2.3.5 Tidal harmonic components

TPXO is a collection of global ocean tide models that effectively fit the Laplace Tidal Equations and altimetry data using a least-squares approach. Each subsequent model in the TPXO series incorporates updated bathymetry and assimilates more data compared

to previous versions. These models were generated using the OTIS software, which implements the methods described in detail by Egbert and Erofeeva 2002. The TPXO models include complex amplitudes of sea-surface elevations relative to mean sea level (MSL) and currents for eight primary harmonic constituents (M2, S2, N2, K2, K1, O1, P1, Q1), two long-period constituents (Mf, Mm), and three non-linear constituents (M4, MS4, MN4). TPXO8-atlas represents the first generation of new atlas solutions. Similar to older ATLAS solutions, the new generation solutions combine a fundamental global solution (TPXO8) obtained at a resolution of 1/6 degree and high-resolution (HR) local solutions.

	PARAMETERS	PARENT	CHILD
Time	start date	Since 29 Nov 2020	02/02/2021
	n days	-	26
	spinup time	-	3 days
	$\Delta t_{baroclinic}$	360 s	120 s
	Courant num.	-	$C \leq 0.8$
	output	daily mean	hourly mean
Spatial Grid			
horizontal	lon λ (°W)	global	89.0 ÷ 59.0
	lat ϕ (°N)	global	7.75 ÷ 20.6
	$\Delta\lambda$,$\Delta\phi$	0.083°	0.027°
	Δx,Δy	$\sim$ 9 Km	$\sim$ 3 Km
	$n_x \times n_y$	4320 × 2041	1078 × 464
vertical	n_z	50	100
	h_{cr}	-	30
	h_{th}	-	50
	dz^w_{min}	-	1
	$h_{max}(m)$	5727.92	5700
Sub-grid physics	hor. viscosity (m^4/s^2)		
	bilaplacian	-1.25 $\times 10^{10}$	-1.54 $\times 10^{8}$
	hor. diff. (m^2/s)		
	laplacian	100	25
	vert. mixing	TKE param.	PP
	vert. visc. (m^2/s)	1.0 $\times 10^{-4}$	1.2 $\times 10^{-5}$
	vert. diff. (m^2/s)	1.0 $\times 10^{-5}$	1.2 $\times 10^{-6}$
	EVD coeff (m^2/s)	10	10
Bottom friction	drag. coeff.	1.0 $\times 10^{-3}$	1.0 $\times 10^{-5}$
	bottom TKE (m^2/s^2)	-	2.5 $\times 10^{-3}$

Table 2.1: model setup and parameters for the Parent and the Child model.

2.4 Manipulation of topography and bathymetry

In the chapter 4 of this work, the topography and the bathymetry have been changed. The bathymetry, and the coastlines used as input to the reference experiment (child model), are respectively: the dataset $GEBCO\_2014$ and the $GSHHS\_h\_L1$ coastline system, as mentioned above.

Only the bathymetry and coastline of one particular island has been changed, which can be seen in our focus area shown in Fig.2.3 and is shown more clearly in Fig.2.4. The island mention is The Petrel Island, also known as Bajo Nuevo Bank, is a tiny,

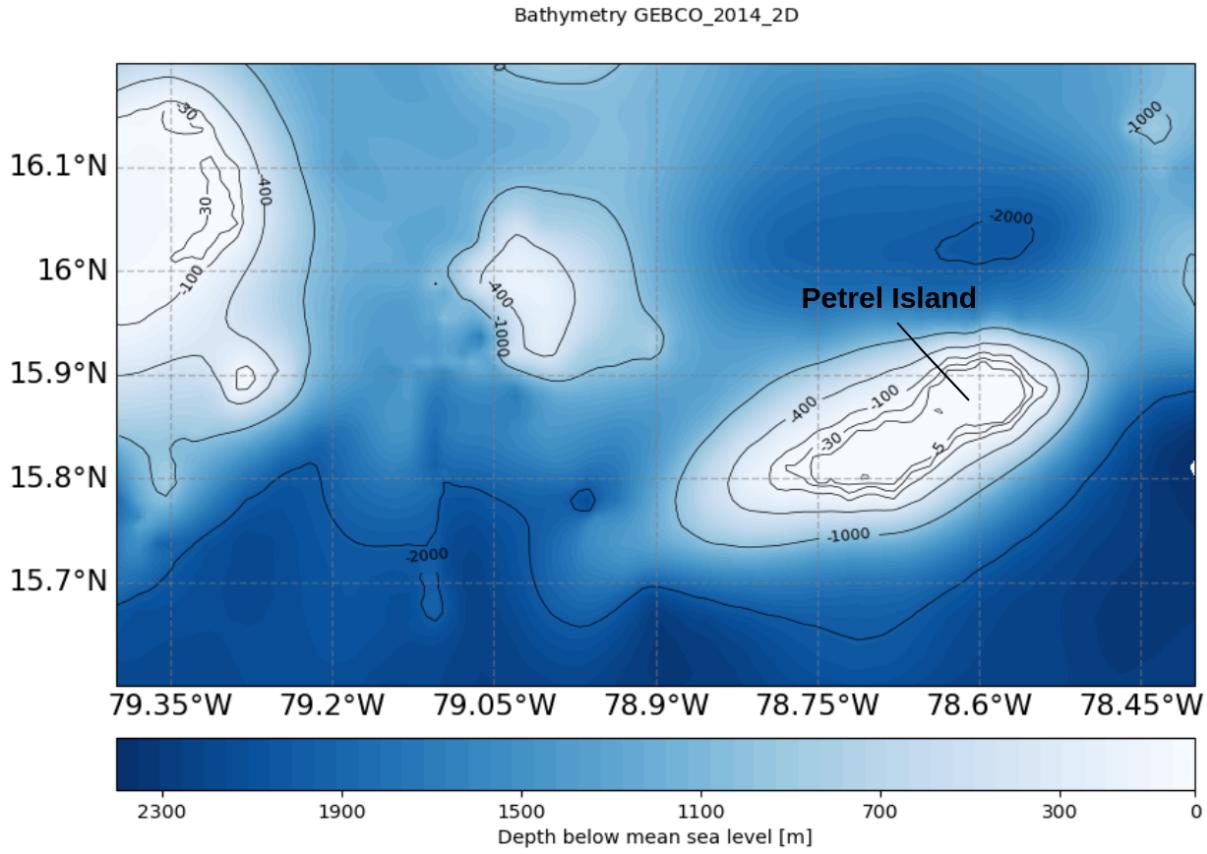

Figure 2.4: Bathymetry dataset $GEBCO\_2014$, in a limited region of interest, used in input in the simulation.

deserted reef located in the western Caribbean Sea at 15.85°N 78.66°W.

As mentioned, this is an island, but due to the simplifications and resolution of the initial dataset, it appears in $GEBCO\_2014$ as a seamount, with a subemergence of 2 m, while the coastline contours present it as an emergence of only two small points (see top left graph in Fig.4.2).

Following interpolation on the grid of the child model, the two emergences are lost, and due to the small size of the island it does not emerge distinctly untill the depth of 10 metres. The topography was therefore first changed so that it was as close as possible

to its actual shape even at the surface (this step is referred as Exp.2 in chapter 4), and then the bathymetry was modified in order to understand what effect the island had on the dynamics at the sub-mesoscale (this step is referred as Exp.3 in chapter 4). The graphical results of the changes are shown later in Fig.4.2.

QGIS was utilized to interactively display and modify coastal lines. Using its graphical interface, it allows to import the coastline data and visualize it on a map. Additionally, QGIS provided tools and functionalities that enabled me to edit and manipulate the coastline features. QGIS, which stands for Quantum Geographic Information System, is an open-source software that allows users to create, edit, visualize, and analyze geospatial data[3].

To change the bathymetry, we act on the SURF configuration file, by specifying the longitude and latitude of the boundaries and the depth of rectangular regions to cut.

Fig.2.5 also shows bathymetry, in the same area of Fig.2.4, as a 3D visualisation.

Figs.2.6 also show Petrel Island as seen from Google Earth (figure on top) and from the International Space Station[4] (figures on bottom). Photos centre point is 15.87° N, 78.65° W.

The photo shows how, contrary to what is shown in the bathymetry plot (Fig. 2.4), this structure in question actually emerges, in two places with a small discontinuity in between, and can even be viewed from the space.

[3]see https://www.qgis.org/it/site/ for more information

[4]NASA Photo ID ISS004-E-7525 https://eol.jsc.nasa.gov/SearchPhotos/photo.pl?mission=ISS004&roll=E&frame=7525

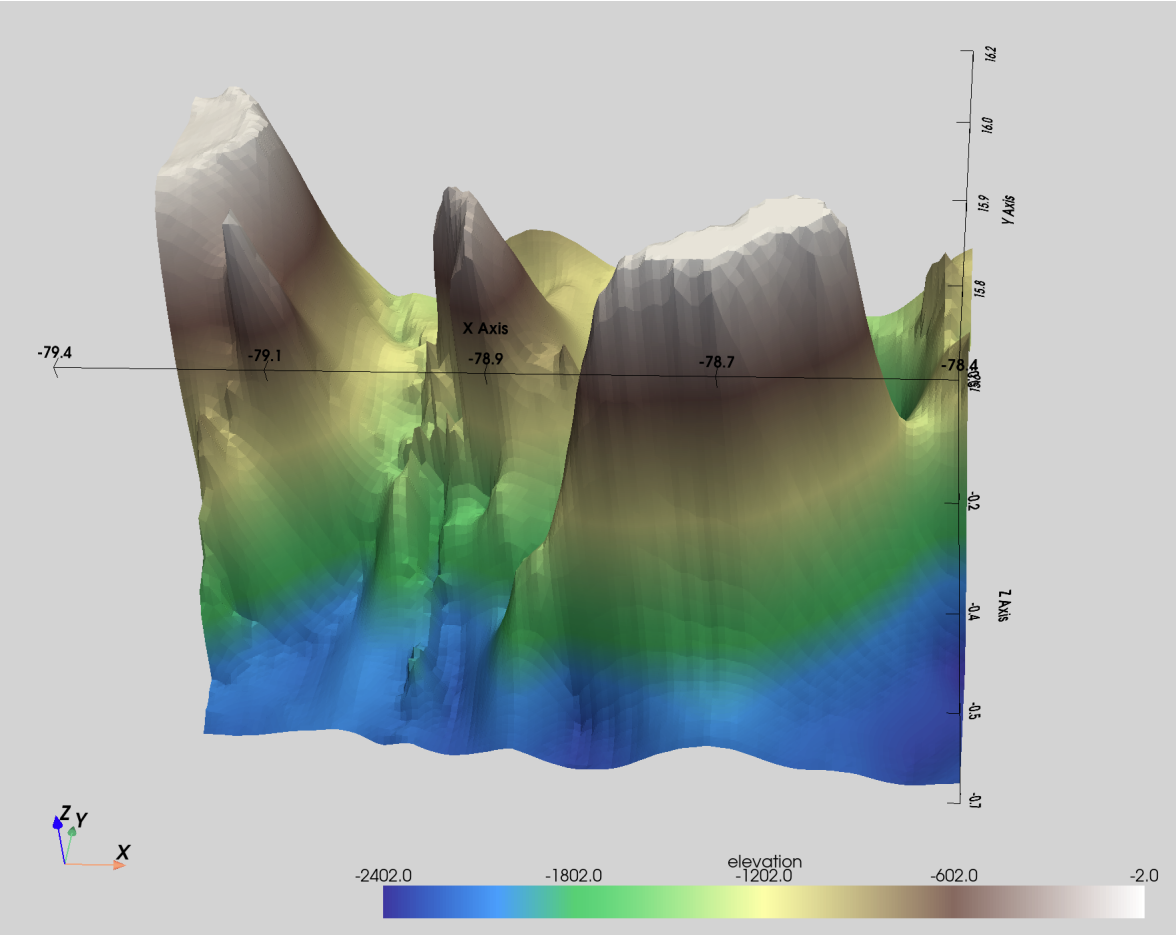

Figure 2.5: Bathymetry dataset *GEBCO_2014*, in a limited region of interest, used in input in the simulation.

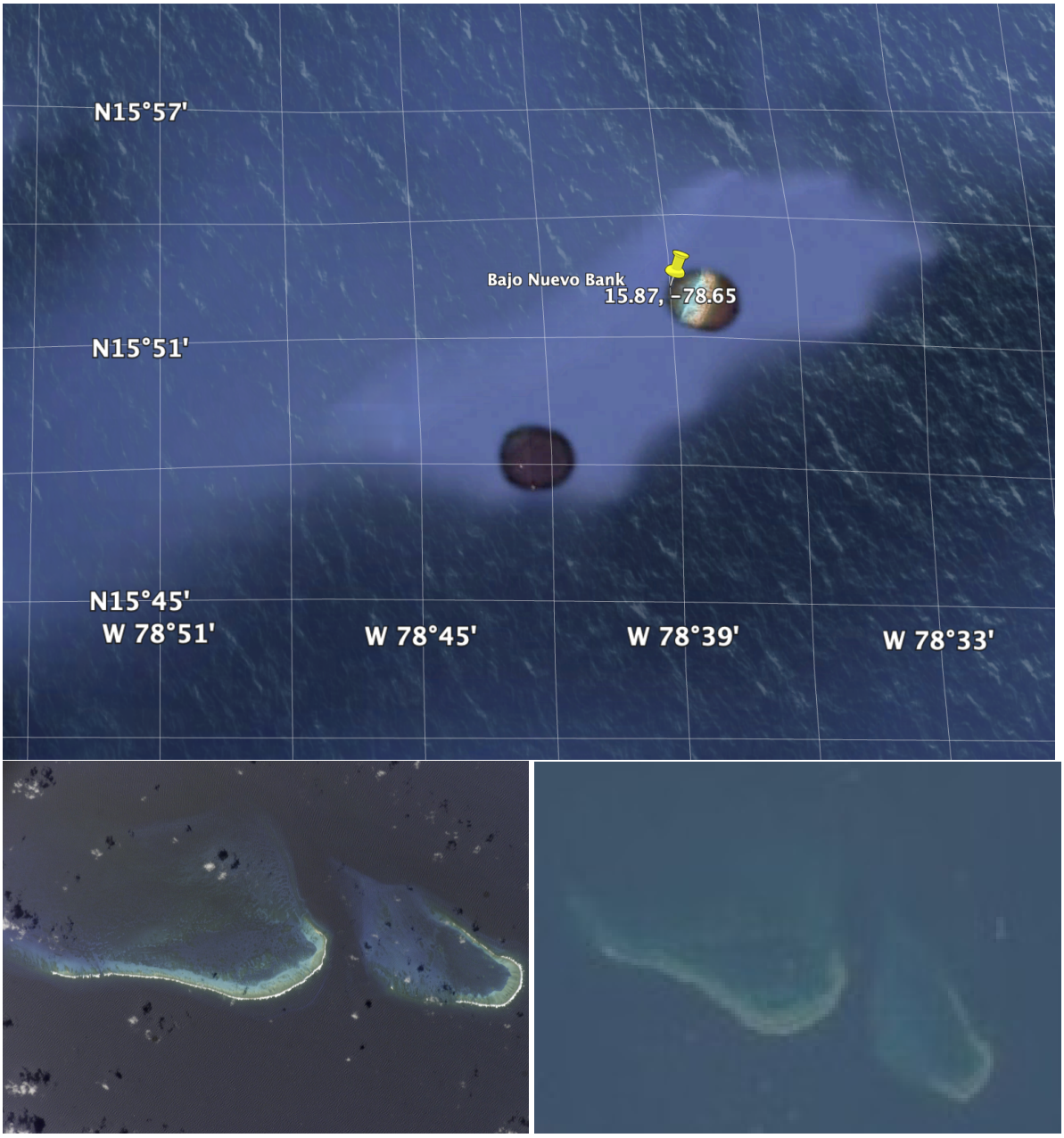

Figure 2.6: Petrel Island from Google Earth (top) and from ISS (two on bottom), photos centre point is 15.87° N, 78.65° W.
Furthermore, the axes seen in the figure above are characterised by numbers in the sexagesimal system, unlike the decimal system used for all other plots in this work.

CHAPTER 3

Mesoscale and Submesoscale Analysis in the Caribbean Sea

In this chapter, we present an overview of to the mesoscale features in the Caribbean Sea region. The period analysed is from the 2nd to 28th of February 2021.
We first analyze the results obtained from the coarser-grid *parent* model, focusing on the fields of velocity, temperature, salinity, and relative vorticity at 10 m depth within the surface mixed layer.
We then compare this results with the finer-grid child model results.
We also analyze the vertical profiles of the Brunt-Väisälä frequency and the Kinetic Energy to understand the vertical stratification.
The aim is to study the onset of submesoscale processes in our region of interest, as well as the advantages of high-resolution downscaled fields.

3.1 Mesoscale variability in the Caribbean Sea

The Rossby radius of deformation characterizes the observed mesoscale length scales, and in the Caribbean Sea, it is in the range of 50-75 km according to LaCasce 2020, see Fig.1.4. Since the CMEMS dataset has a horizontal resolution of $1/12^{\circ}$ (approximately 9 km in the Caribbean Sea), it is expected to resolve the mesoscale dynamics well in this region. We focus on the month of February and daily average the hourly data from the child model to make a consistent comparison with the parent CMEMS global

model. The daily mean currents, relative vorticity, temperature, and salinity fields at 10 m depth within the mixed layer are shown in Figure 3.3.

Mesoscale eddies typically form from initial instabilities created by the interaction between strong horizontally sheared currents or from current-topography interactions in boundary currents (López-Álzate et al. 2022).

As regards daily mean currents, relative vorticity, temperature and salinity we show the horizontal fields nearly 10 m deep. This is considered significant for studying horizontal features inside the Mixed-Layer (ML), as here important submesoscale processes may take place. Fig.3.1 shows the monthly mean ML depth in the Caribbean Sea, that was found to be 34.84 m.

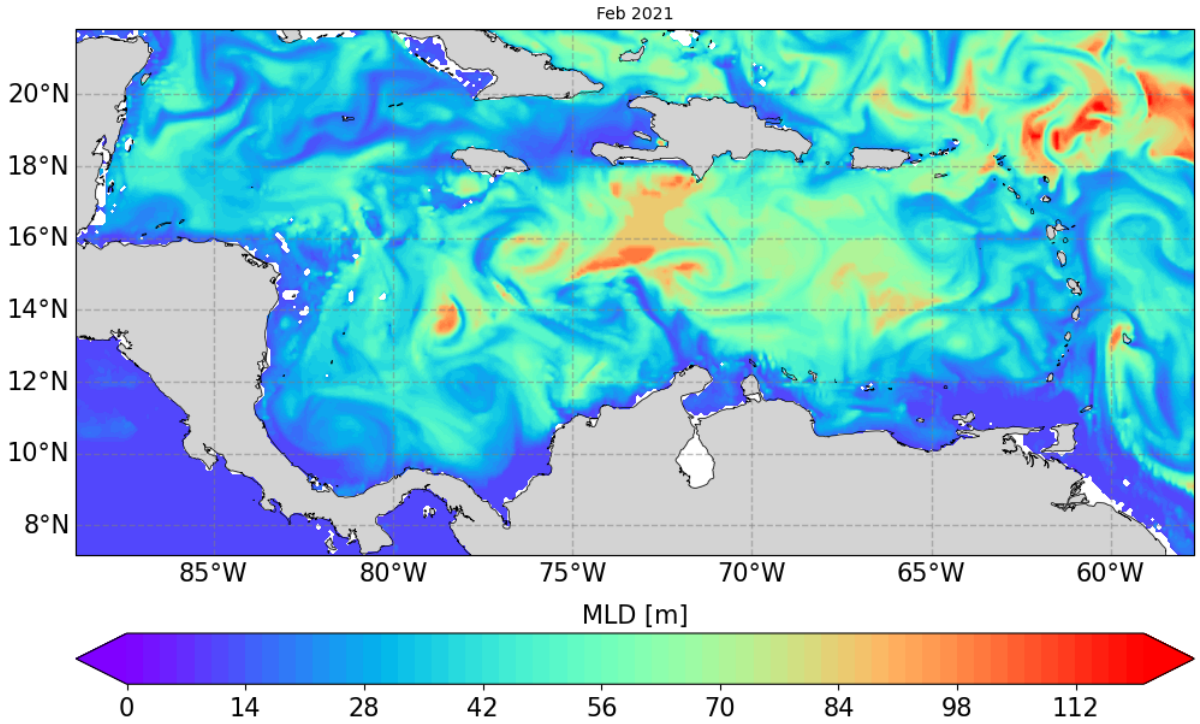

Figure 3.1: Mixed-layer depth for the parent CMEMS global model: monthly mean of Feb. 2021 for the parent model.

Fig.3.2 shows the sea surface height (SSH) field with superimposed velocity field at the surface, , averaged for the month of February. One can see two anticyclonic eddies on the south-west side of the study area (west of 75° W) with central SSH a few to tens of centimeters higher than the surrounding water and one cyclonic eddies in the central Caribbean with a lower central SSH.

In Fig. 3.3 the velocity fields evolution is shown, comparing values for Feb 5th, the simulation day after 3-day spin-up period, the 28th, the last day of the simulation. The spin-up period is defined as the time necessary by the child ocean model to reach a steady state value for the volume average kinetic energy, starting from initial and

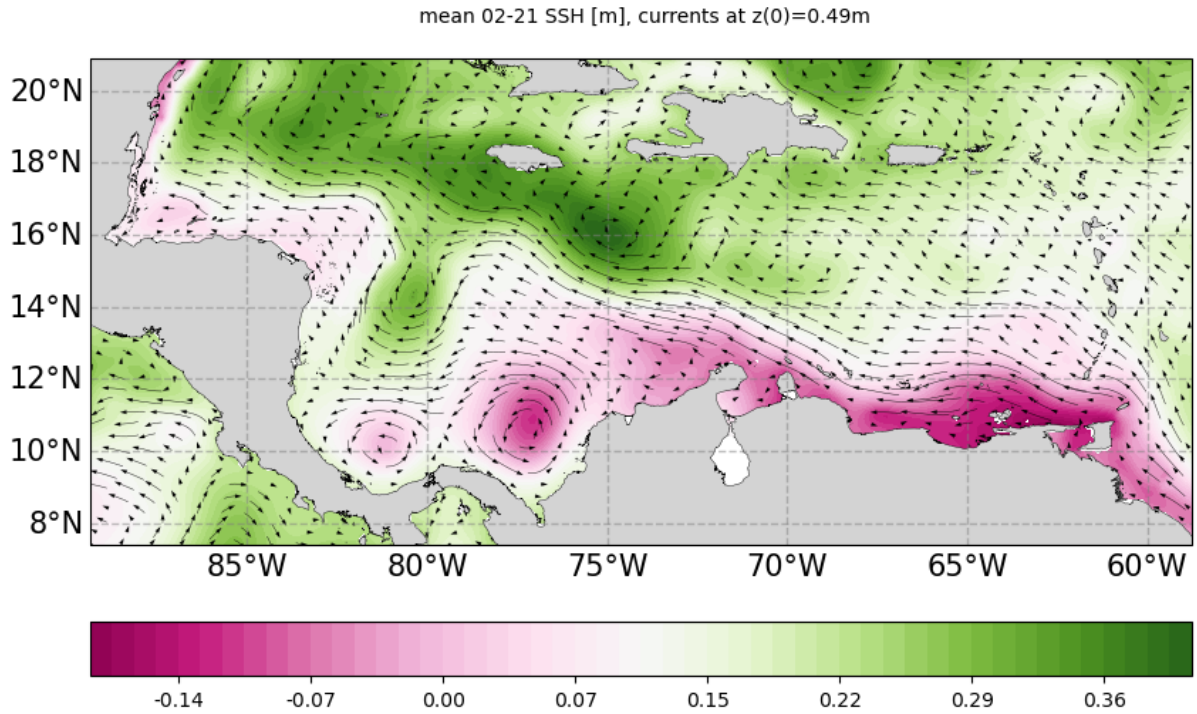

Figure 3.2: SSH for the parent CMEMS global model, with superimposed velocity field at the surface: monthly mean of Feb. 2021 for the parent model.

lateral boundary conditions interpolated from the parent model, Simoncelli et al. 2011. When referencing place names in this work, see to Fig. 2.3.

At 10 m depth, two strong and energetic jets are dominant, flowing westward through the Grenada Passage, St-Vincent and St-Lucia Passages, known as the North Brazil current and the North Equatorial Current, respectively. These currents have intensities of up to 1.4 m/s and a salinity of approximately 35 PSU. The Subtropical Gyre also contributes to the Caribbean circulation with slightly higher salinity levels (around 36.5-37 PSU) : see Fig.3.5.

In the Colombia basin and Venezuela basin, two main current systems are formed at the southern and northern boundaries. Numerous eddy structures are observed, including an anticyclone located around 75°W, 16°N, which shows a westward shift during February. Another persistent anticyclone is present around 69°W, 15°N, while a cyclonic circulation structure is observed above it. A smaller anticyclonic structure is found in the eastern part of the Venezuela basin (65°W-15°N).

All of this is consistent with Jouanno et al. 2008 that state that most eddies in the Caribbean Sea are anticyclonic with also the presence of smaller and weaker cyclonic eddies, mainly located near the northern part of the Venezuela Basin.

The Panama-Colombia Gyre, formed by the currents from the Guadeloupe Passage, exhibits cyclonic structures at 81.5°W, 11°N and 77°W, 11°N, with velocities reaching up to 0.96 m/s on the 5th of Feb. These cyclonic eddies interact with a persistent anti-

cyclonic structure at 80°W, 14°N. Additionally, cyclonic systems are observed between Jamaica and Cuba.
The Currents from the Guadeloupe Passage, that feeds the cyclonic Panama-Colombia Gyre, merge together with the currents in the northern part of the Venezuela basin, they leave the sea at high speed ($\sim 0.7 m/s$) through the Chibcha channel, and then head for the Mexican coast.
The sea surface height (SSH) field with superimposed velocity field at the surface, Fig.3.2), averaged for the month of February, shows the Panama-Colombia cyclonic gyre exhibits two SSH local minima, in agreement with López-Álzate et al. 2022. The salinity and potential temperature at 10 m of depth of the parent model respectively are shown in Fig.3.5 and Fig.3.4 for Feb 5th and for the Feb 28th. Being the region further southward, temperatures are high, ranging from about 22.5°C to 29.5 °C
The warmer temperature, around 29.5°, is found in the Colombian basin and towards the Cayman basin. The colder temperature is along the Venezuela coast, with temperature reaching the 21.5°. Furthermore, by looking at the temperature field one may better identify the signature of meanders and big vortices; in agreement with López-Álzate et al. 2022 depending on which side with respect to the main flow they form, eddies may contain either relatively warm or cold water compared to their surroundings.
Anticyclonic eddies in the Venezuela basin contain a warm-core and display a central Sea Surface Height of a few to tens of centimetres higher than outer water, while cold-core eddies present a central SSH lower than its surroundings.
The distribution of the tracers follows the progression of the anticyclonic eddy between the first and the last day of the analyzed time period, due to the advection of this scalar fields.
During the entire simulation, the water temperature cools in the Venezuelan and Colombian basins. These basins also seem to increase their salinity, while the western part of the Caribbean Sea remains unchanged and follows the shifts already seen in the temperature and current fields. Finally, the vorticity fields (Fig. 3.6) show a better definition of some structures at the end of the analysis period, but in particular, when crossing the Chibcha channel, with a lower water depth than the rest of the domain, rich in islands and sea mountains, thin filaments of positive and negative vorticity are created, with very high values in modulus. When a current meets a slope, as the vertical velocity goes to zero, vertical vorticity is generated in the BBL. Our following analysis will focus mainly on this area of the Chibcha channel. In summary, the Caribbean Sea region exhibits a complex mesoscale circulation, characterized by the presence of currents, eddies, and gyres with various intensities and structures. These features play a crucial role in the region's oceanic processes and should be considered when studying

the local marine environment.
As the authors López-Álzate et al. 2022 states the formation of eddies is mainly due to flow-topography interaction, the meandering of the Caribbean boundary current, and the growth of baroclinic instabilities around river plume fronts. As we can see in Fig. 3.4, 3.5 the cold filaments at the eastern side of the basin lead to a cooling if the Caribbean Sea eastern part, and some eddies transport salinity anomalies from Amazon and Orinoco river plumes westward.

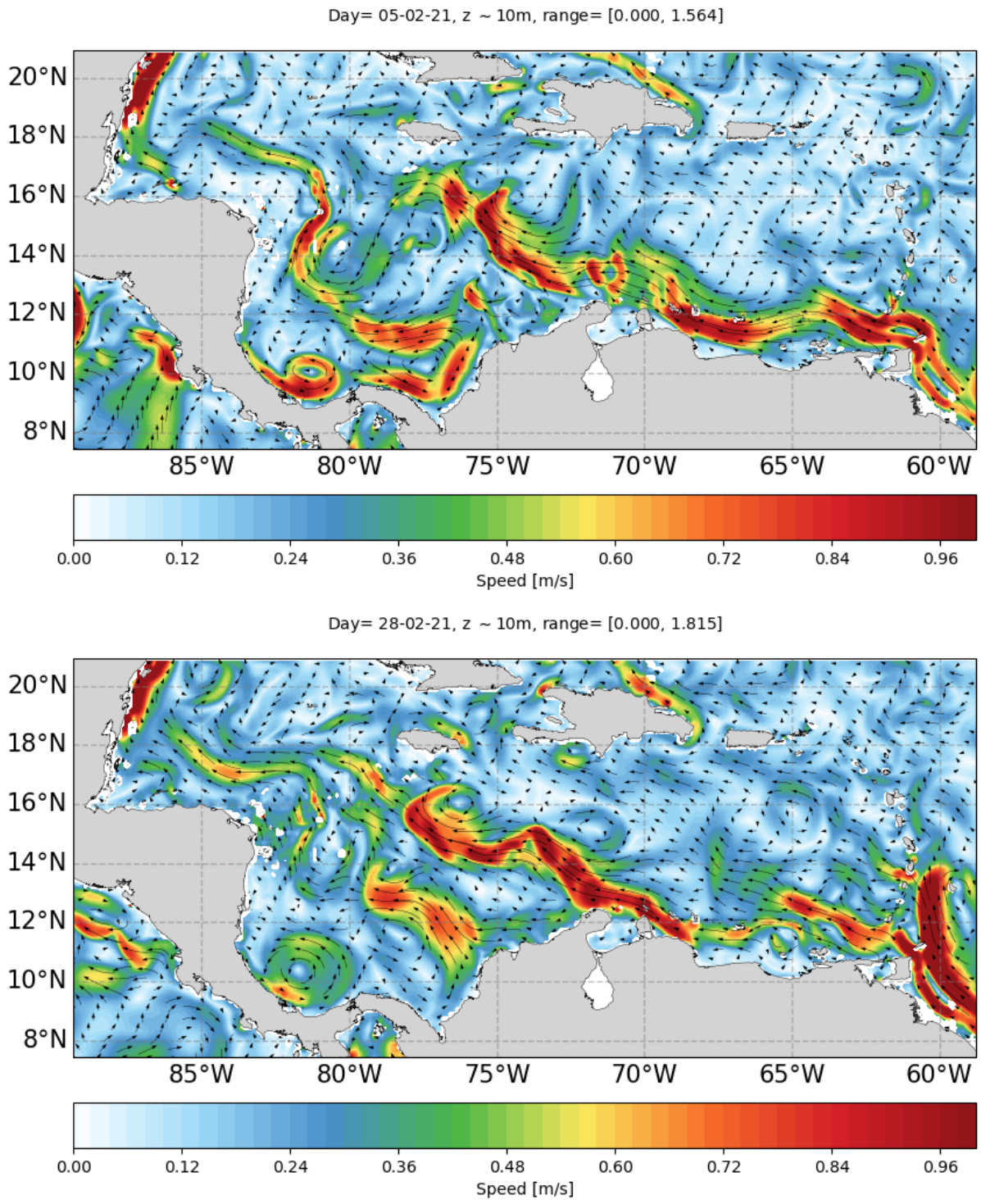

Figure 3.3: Velocity field for the parent CMEMS global model: for the Feb 5th (top) and 28th (middle) for the parent model.

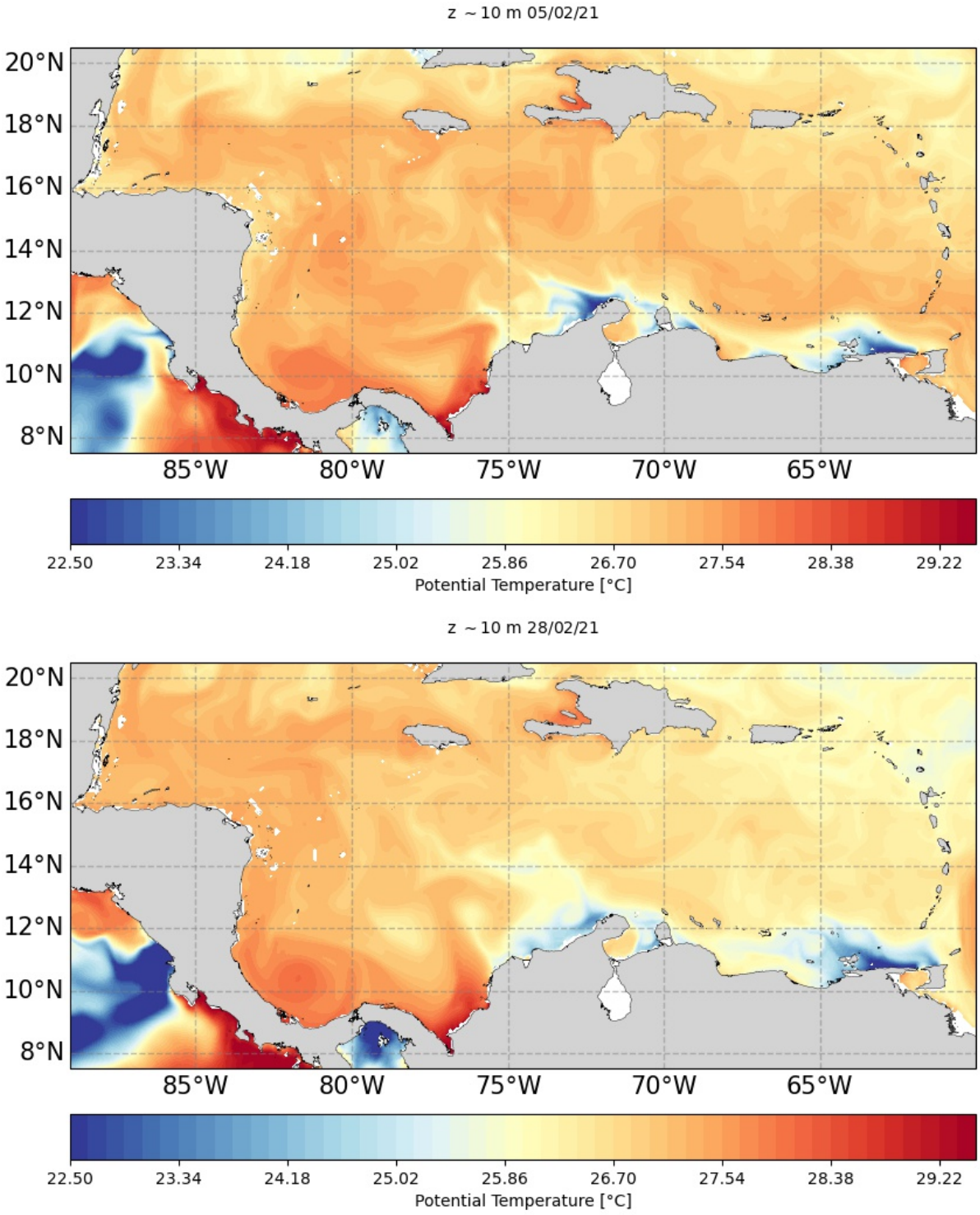

Figure 3.4: Potential temperature for February 2021 5th and 28 of the parent CMEMS global model.

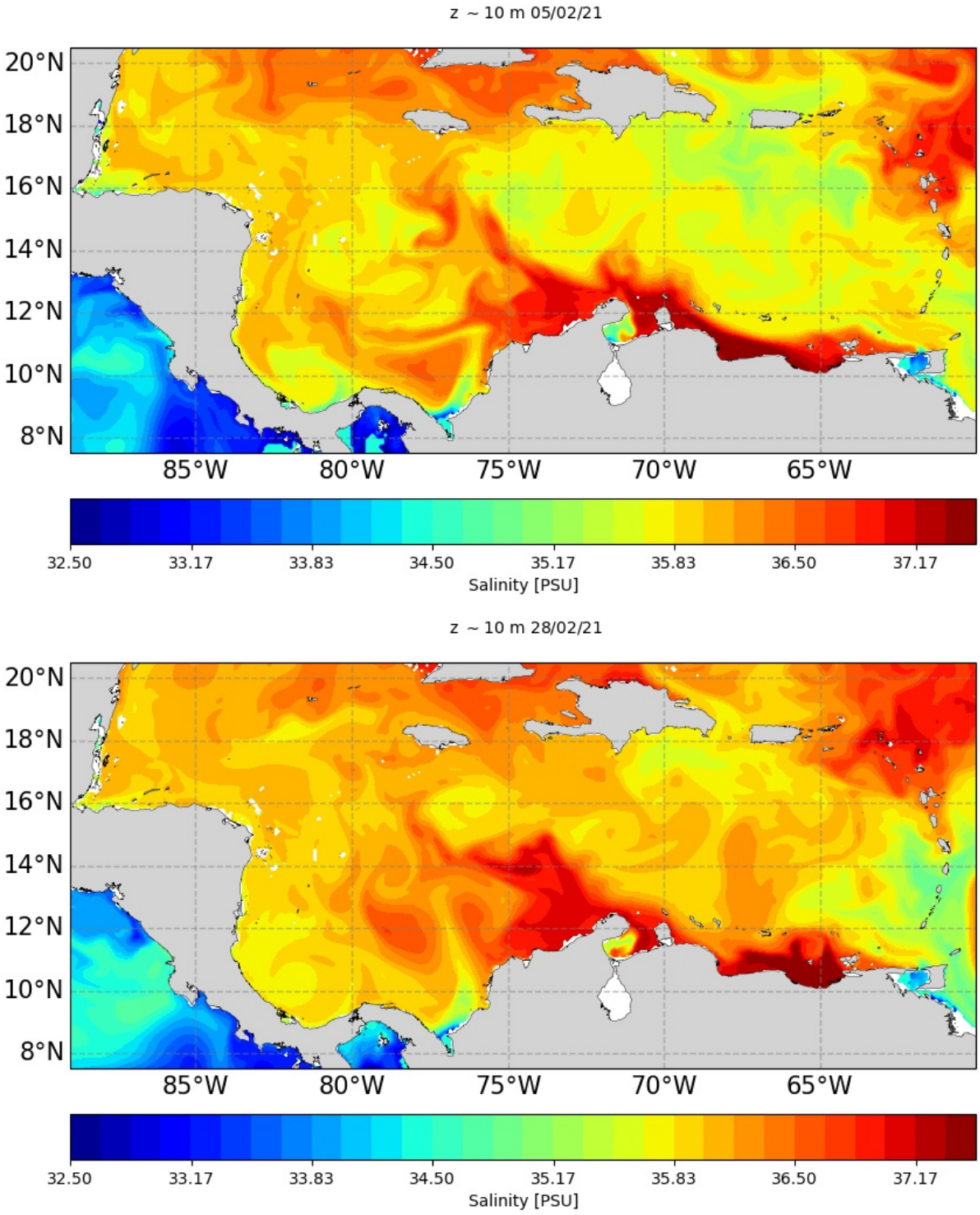

Figure 3.5: Salinity for February 2021 5th and 28 of the parent CMEMS global model.

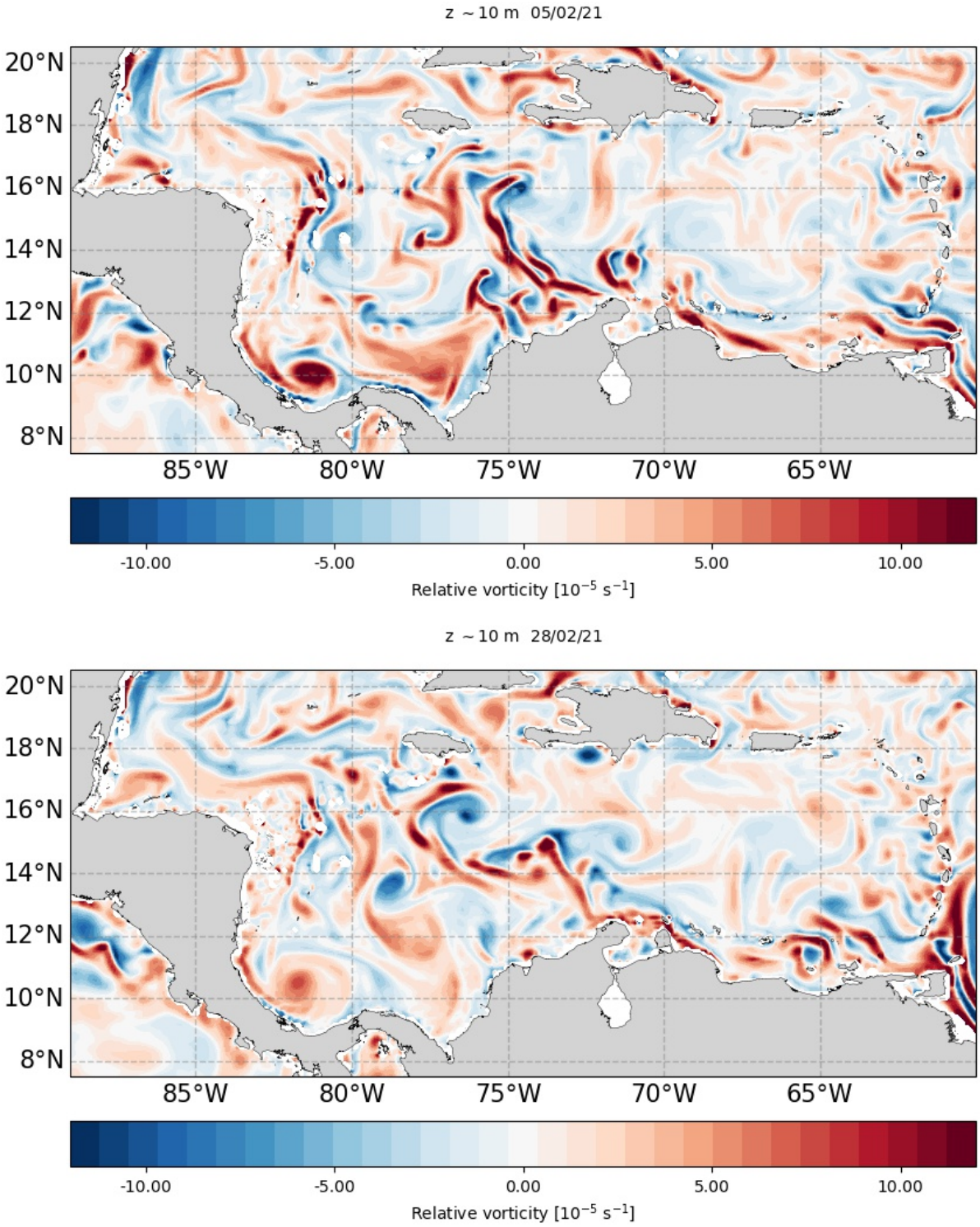

Figure 3.6: Relative vorticity for February 2021 5th and 28 of the parent CMEMS global model.

3.2 Submesoscale variability in the Caribbean Sea

Downscaling was performed on the entire domain, but as I would like to focus on the effect of topography in mesoscale and submesoscale dynamics: in this section we will study the onset of submesoscale processes in the Chibcha channel area; along with benefits of the high-resolution downscaled fields.
Here the currents are approaching an area where the depth of the seafloor is decreasing. To study the emergence of submesoscale dynamics in this area, starting with the parent model at horizontal resolution of $1/12°$, a higher horizontal resolution simulation was performed by downscaling. The nesting has a horizontal resolution of $1/36°$ ($\sim$ 3 km) and includes the entire Caribbean Sea.
In the following sections, we compare horizontal fields and vertical structures from the parent coarser simulation and the child high-resolution ones showing the benefits obtained through the downscaling, in the specific area described above, which is bounded by latitude values of $14.1 \div 17.9$ N and longitude values of $83.7 \div 73.2$ W. We will compare the fields already analyzed in the previus section, from the parent coarse model and from our child high-resolution model.
To compare the fields consistently, the hourly data of the child model have been daily averaged and interpolated on the parent computational grid. We noticed that the increase in resolution also brings the emergence of several islands as well a refined bathymetry which could also have an impact on the flow structure.

3.2.1 Current Field and Relative Vorticity Field

In Fig.s 3.7, 3.8, the current field and the relative vorticity field comparisons at nearly 10 m depth are shown in our region, on Feb. 5 (Fig. 3.7a, 3.8a) and Feb 28 (Fig. 3.7b, 3.8b), 2021.

At the beginning of our simulation, the low-resolution model and the high-resolution model show no particular differences in the spatial distribution of values neither in the horizontal velocity nor in the relative vorticity range.
However, more complex structures are already emerging in the western part of the graphs in the proximity of all the islands, which emerge in the child model due to the increase in resolution.
The surface vorticity patterns of the parent model are dominated by eddies, but higher-resolution case also prominently displays SM frontal patterns.
With regard to the velocity field on the last day of the simulation, on the other hand, there are many differences; around the islands near the coast of Honduras, much greater values are recorded than in the parent model, with currents of up to 1 m/s. In general,

the child model shows higher velocity values. The parent model then shows two well-defined anticyclonic structures, around longitude 76.5°W, these mesoscale structures are lost in the child model, resulting in a more complex structure showing submesoscale features within it.
In addition, the large central jet, around the point 15.8°N-78.7°W encounters an island, and in the graph 3.7b this topographic structure splits the current, creating two strong currents laterally, while behind it complex filaments are created.

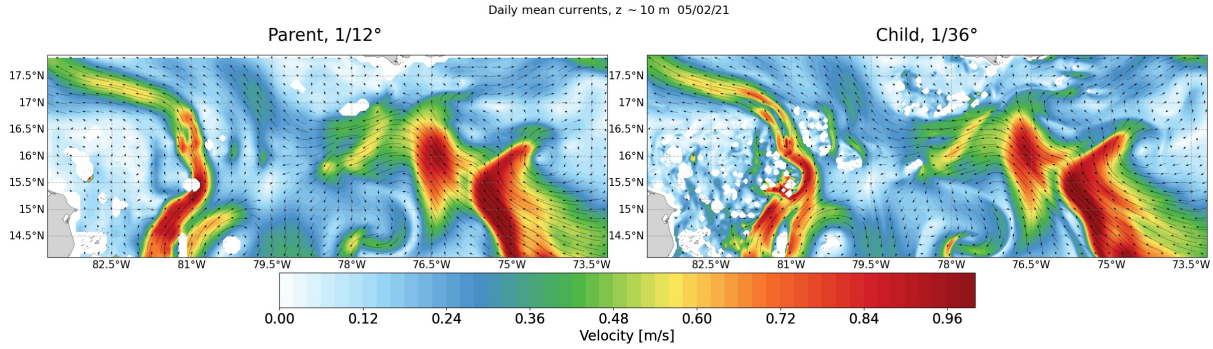

(a) 05/02/2021

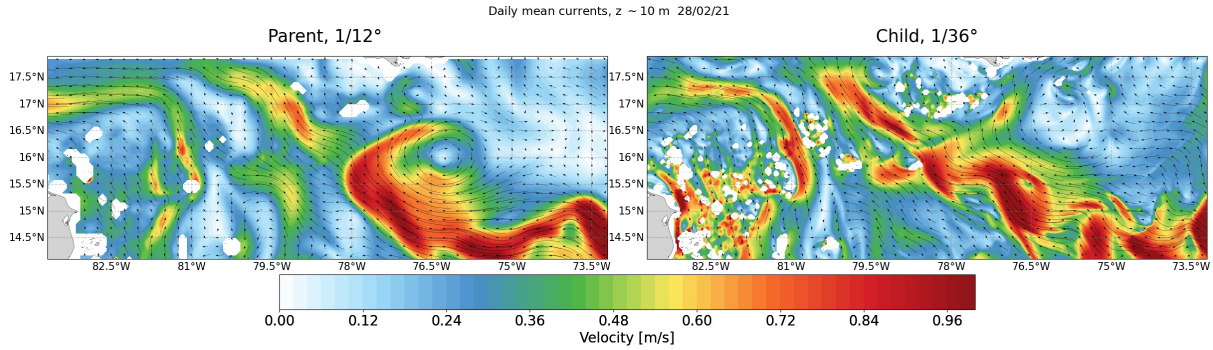

(b) 28/02/2021

Figure 3.7: Daily mean horizontal currents at nearly 10 m depth: comparison between parent and child models in the Chibcha channel, on Feb 5 (up) and 28 (down), 2021.

The relative vorticity fields are initially quite similar (Fig. 3.8a) between parent and child, after 28 days of simulations the differences are substantial (Fig. 3.8b). It is also noticeable here that the central anticyclonic structure is no longer seen in the child model and gives way to a structure with 4 zones with large relative vorticity modulus. The small-scale structures are thus clearly recognisable, especially in the final part of the simulation.
Around the islands and seamounts near the coast of Honduras, smaller eddy and filaments of relative vorticity emerge from non-linear interactions as the resolution increases. Especially the one at 15.8°N-78.7°W the child model seems to clearly outline vorticity wakes in the leeward of it. In contrast to the open Venezuela basin, large horizontal velocity e vorticity variance values are seen along the weastern coasts of

Chibacha channel and generally along island wakes visible as coastally spun eddies and fronts.
These are a result of the separation of bottom drag–generated shear layers in shallow water that spawn near-surface SM eddies. They are especially prevalent near coastal headlands and islands with strong passing currents.

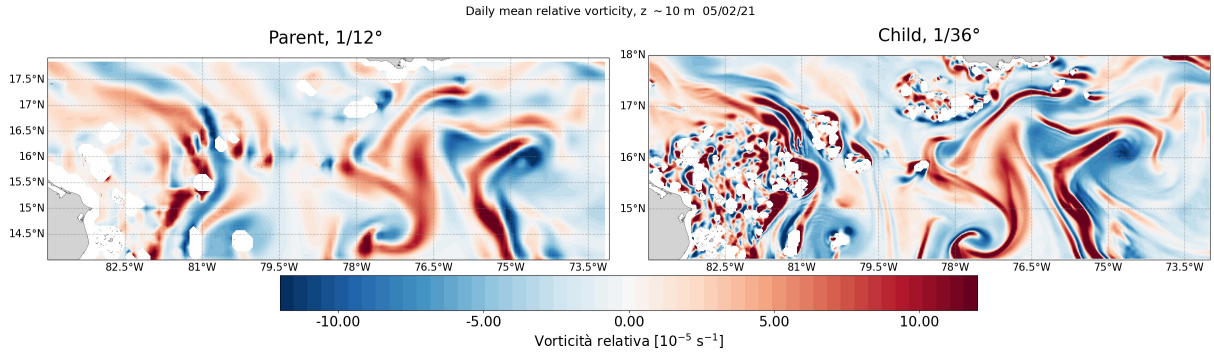

(a) 05/02/2021

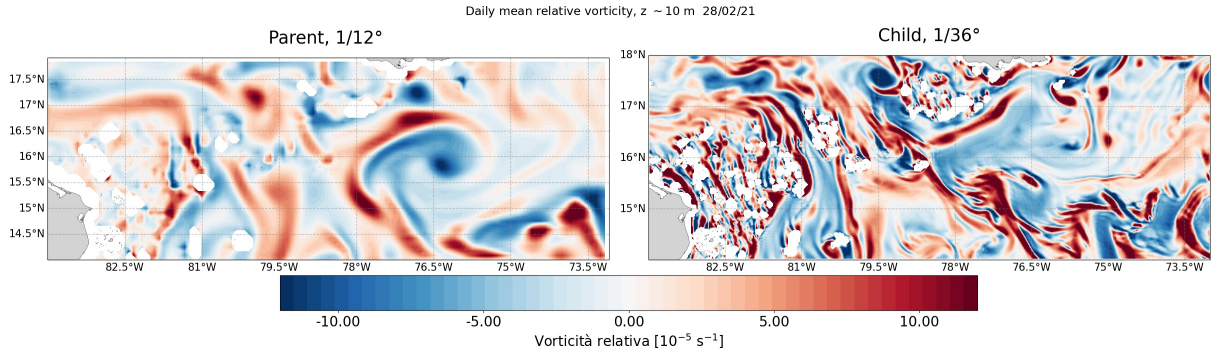

(b) 28/02/2021

Figure 3.8: Daily mean relative vorticity at nearly 10 m depth: comparison between parent and child models in the Chibcha channel, on Feb 5 (up) and 28 (down), 2021.

3.2.2 Rossby numbers

In our area of interest we determine the presence of instability at the submesoscale by observing the Rossby number (ξ_z/f), the daily mean R_o number field is computed by dividing relative vorticity by the latitude-dependent Coriolis parameter f. Fig.3.10 shows the Rossby number at the two scales analysed by us, on the last day of the simulation, at 10 m depth.
Considering the parent model, the R_o number is mainly in the geostrophic range, i.e. between -1 and 1, which excludes the presence of submesoscale activity. However, when we move to a resolution of 3 km, thinner filaments with high Rossby numbers ($|R_o|>1$) begin to develop, both positive and negative through the Chibcha channel. This is indicative of a transition to a more ageostrophic regime. In Fig.3.9 we also show the distributions of the Rossby number R_o, for the last day of our simulation.

The distributions are obtained by considering the fields in Fig.3.10 at a depth of 10 m. It can be seen that, for the last day of the simulation, the distributions of parents and children differ significantly, with those of children reaching higher absolute values of the R_o number. This becomes clearer by comparing the kurtosis and standard deviation values of the distribution (Tab. 3.10). The standard deviation of the child model turns out to be much larger than that of the parent model. The kurtosis of the child model is greater than that of the parent model because the tails of the distribution are thicker. This indicates that the child model detects submesoscale phenomena much better, which are reflected in large Rossby numbers.

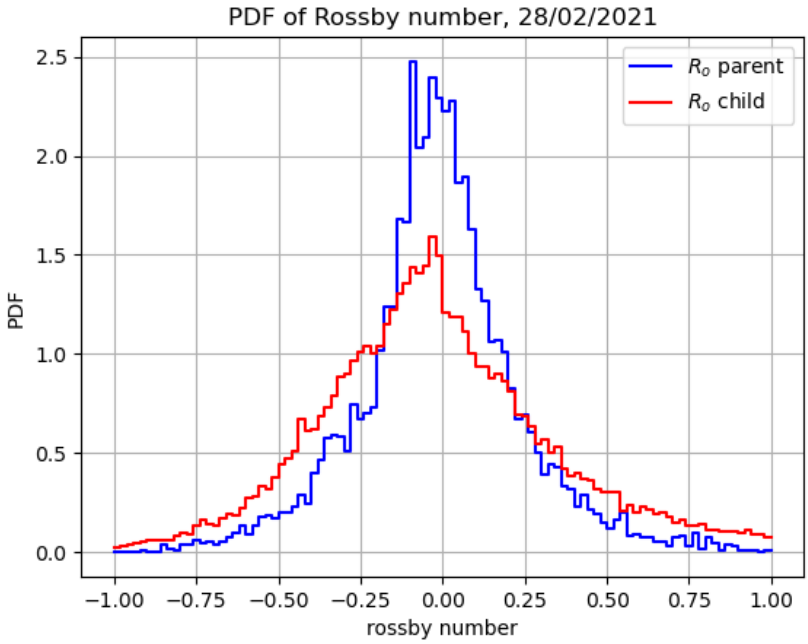

	Parent (red)	Child (blue)
kurtosis	0.87	2.81
std. dev.	0.247	0.434

Figure 3.9: Comparison between parent and child model of the daily mean Rossby number distributions, computed at nearly 10 m depth. The table compare the kurtosis and standard deviation of the distributions.

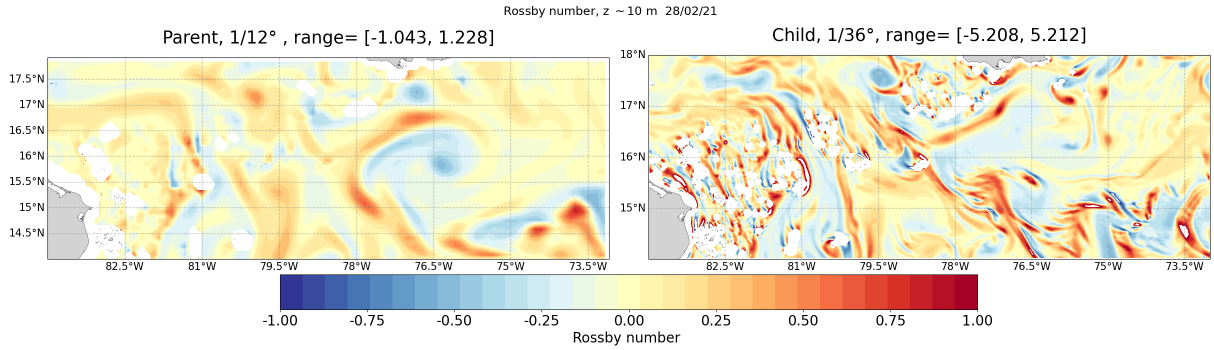

Figure 3.10: Rossby number (ξ_z/f) at 10 m depth, on Feb. 28th, for the parent model (left) and the child model (right).

3.2.3 Mixed Layer Depth, Kinetic Energy

The comparison of the daily mean Mixed-Layer Depth (MLD), shown in the Fig.3.11 as a time series averaged over the area of interest, points out very similar value between parent and child models. The mean value of the MLD are 37.57 m for the parent model and 35.47 m for the child model. From what it seems, the child model makes a prediction that is slightly different, but overall, they are quite similar in terms of the trend. We come to the conclusion that there is a nearly surfacing of the MLD in a consistent part of our region of interest.

As explained in the introductory chapter submesoscale eddies that are produced due to the interaction of mean and mesoscale currents with topography, which generates topographic wakes. The bottom drag in the BBL produce vorticity, the high-vorticity sheets are separated and barotropic instability occurs, that makes separated wakes roll up into submesoscale coherent vortices (SCVs), if the Rossby number R_o is O(1). To asses this barotropic instability we now analyse the Kinetic Energy (KE) and Brunt-Vaisala (BV) frequency profiles.

The KE profile is obtained by averaging the horizontal velocities across each depth layer.

$$\langle KE(z) \rangle = \frac{1}{\Delta x \Delta y} \int_{\Delta x} \int_{\Delta y} (u(z)^2 + v(z)^2) dx dy \tag{3.1}$$

The BV frequency is obtained as in Chap.1 from the density profile averaged over the region, which is computed from vertical mean temperature and salinity as in S. Kanwal 2021.

The two profiles are derived from the specified geographical region, which ranges from 14.1°N to 17.9°N and from 83.7°W to 73.2°W. As observed, the child model exhibits a smoother profile of the Brunt-Väisälä frequency (BV frequency), but with a more pronounced peak (see Figure 3.12b). This observation supports the notion that restratification processes are occurring.

Moreover, analyzing the vertical profiles of kinetic energy (KE) (see Figure 3.12a), it can be observed that the child model identifies higher KE values within the top twenty meters of the water column. This suggests that the KE is predominantly confined to the surface layer. In this region, mixed layer instabilities facilitate the conversion of potential energy into kinetic energy, generating both horizontal and vertical ageostrophic (submesoscale) currents, which contribute to restratification. The disparities in the KE structure between the parent and child models are significant.

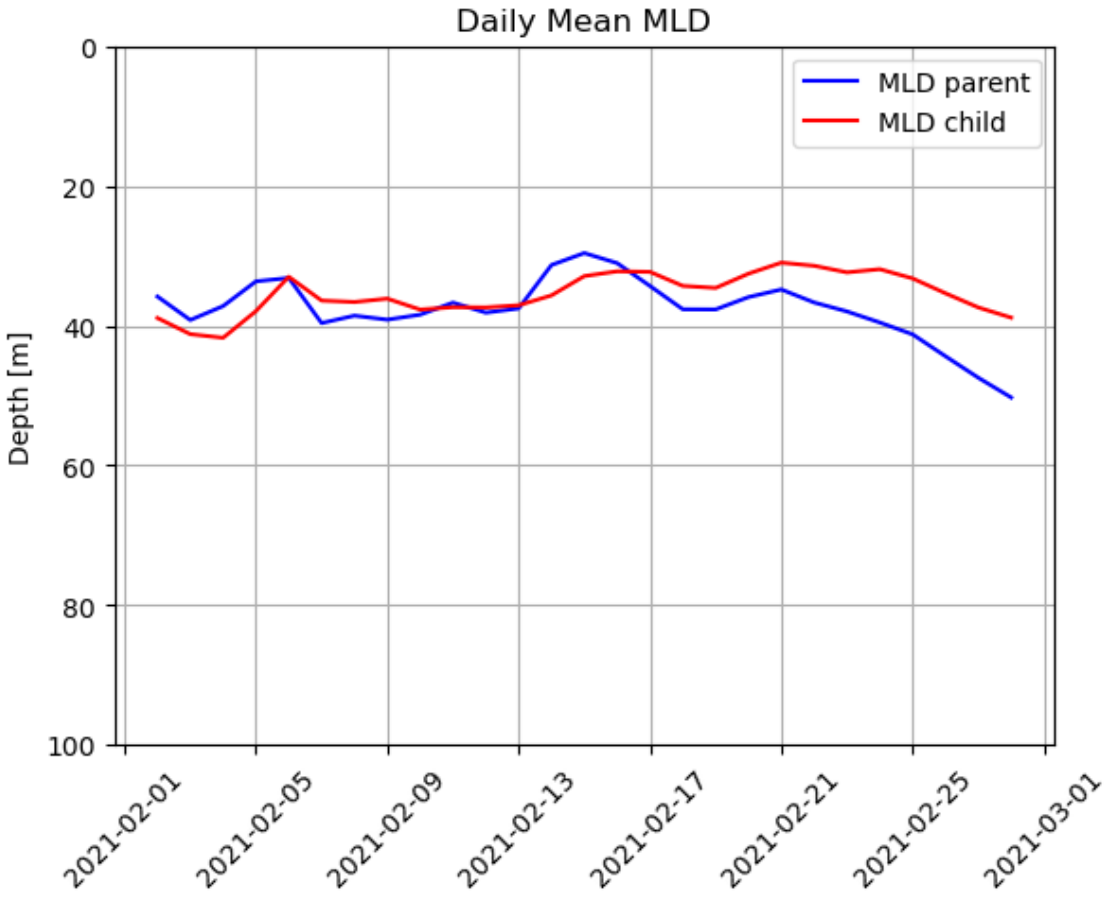

Figure 3.11: Mixed-Layer Depth evolution during Feb 2021: comparison between parent (blue) and child (red) models in the Chibcha channel

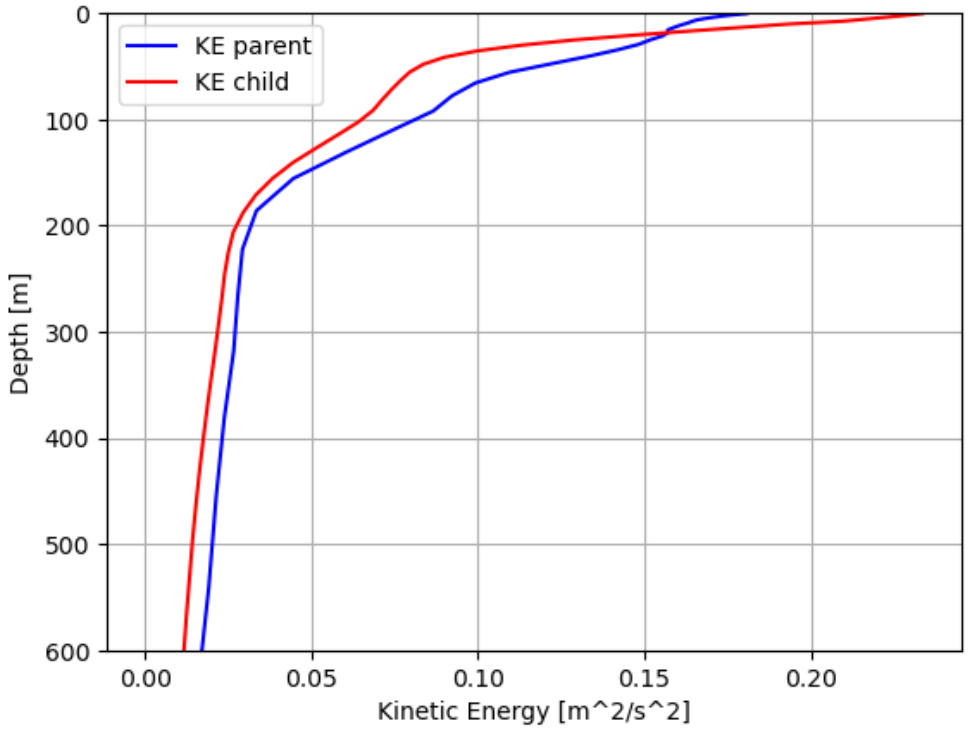

(a) 28/02/2021

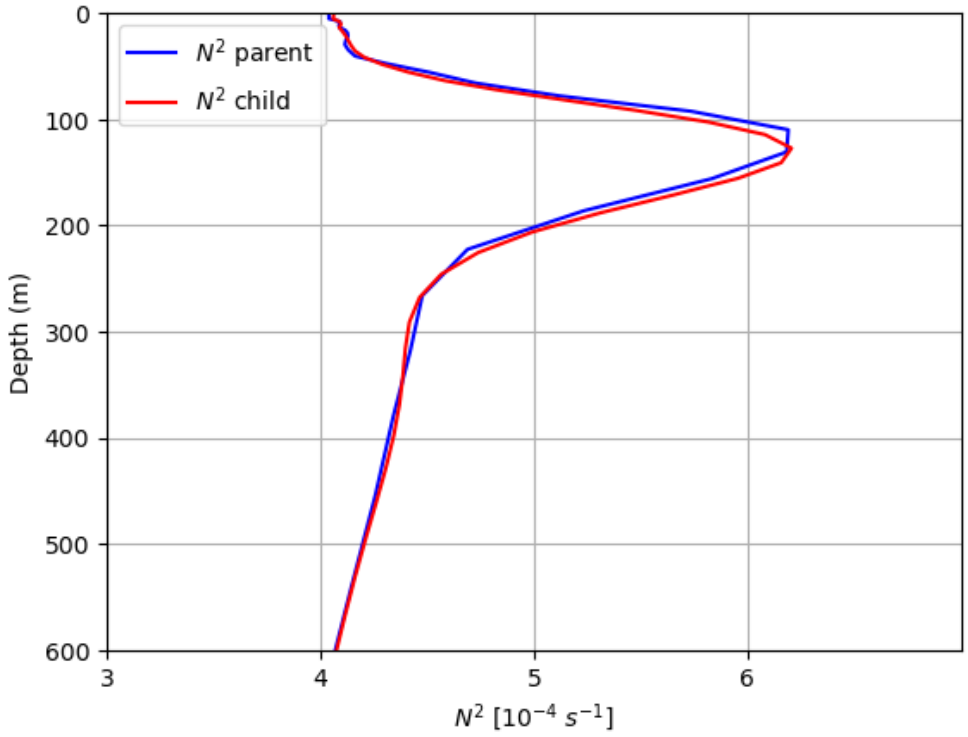

(b) 28/02/2021

Figure 3.12: Profiles of daily mean Kinetic Energy (top panel) and BruntVaisala frequency squared (bottom panel), on Feb 28, 2021. Comparison between parent and child models. The mean vertical profiles are computed over the area of interest: 14.1 ÷ 17.9 N, 83.7 ÷ 73.2 W.

CHAPTER 4

Sensitivity experiments: topographic effects on submesoscale dynamic

In this chapter, the characteristics of the downscaled ocean currents and their interaction with topography in the Chibcha channel of the Caribbean sea is examined.
We will investigate how the island size and the submergence depth influence the ocean dynamic in this particular area. As shown byYang et al. 2017 the eddy trajectory and its structure are affected by an island or a seamount, in particular, under certain conditions, the eddy may split during the interaction with an island/seamount.
The boundary separation of high-vorticity sheets leads to barotropic instability, therefore is an important way to transform energy from the mesoscale to sub-mesoscale in the ocean. During the interaction between a current and a seamount the lower part of the jet is directly affected by the solid seamount while the upper part is not, then the vertical structure of the current is affected significantly.

In this chapter, we draw inspiration from the research conducted by Yang et al. 2017. However, we diverge from their focus on idealized eddies encountering islands or seamounts with simply geometry and instead concentrate on a more realistic scenario of downscaled ocean currents interacting with an island or seamount. By exploring the interaction of currents with islands or seamounts, we aim to gain valuable insights into the characteristics and effects of such interactions in oceanic systems.

4.1 Impinging current

The dynamics of the Caribbean Sea are primarily influenced by a persistent current throughout the simulation. Originating from the east, this current follows the southern coast of the Venezuelan basin, effectively collecting the outermost currents of various anticyclonic and cyclonic structures. Notably, there is a consistent anticyclonic structure located at 75°W-16°N throughout the entire duration of our experiment (refer to Fig. 3.3). This structure, while moving horizontally westwards, maintains a relatively stable latitude and contributes to the formation of a strong current near our island of interest.

As this anticyclone shifts, the associated strong current also moves, directing itself towards the Chibcha Channel in close proximity to the southern coast of Jamaica. Along this trajectory, the current encounters several islands and experiences shallower waters. As expected, the intensity of the current diminishes with depth. On February 28th, at the surface, it measures approximately 70-90 km in thickness and exhibits a peak intensity of up to 1.2 m/s. However, this intensity is halved when reaching a depth of 55 m on the same day.

Moving on to the real case and the setup of our sensitivity experiments, our focus is on Petrel Island, also known as Bajo Nuevo Bank. Situated in the western Caribbean Sea at coordinates 15.87°N 78.65°W, it is a small and uninhabited reef. In close proximity, approximately 110 kilometers to the west, lies Serranilla Bank, the nearest neighboring land feature (see Fig. 4.1).

4.2 Real case and set-up of sensitivity experiments

The Petrel Island, also known as Bajo Nuevo Bank, is a tiny, deserted reef located in the western Caribbean Sea at 15.87°N 78.65°W. Serranilla Bank, 110 kilometers to the west, is the nearest neighboring land feature (see Fig.4.1).
This island is interesting because it is located in a region with shallow depth. The flow in this area is therefore strongly influenced by the bathymetry. This island is one of the first encountered by the strong jet and is also quite isolated from other bathymetric structures, which simplifies the analysis of ocean dynamics. The coastlines used as input to the model (represented in the top left figure of Fig.4.2, colored in gray.) only show two small emergent structures on the surface, with thickness smaller than the grid resolution of the child and parent grids. In the nested model the island still doesn't emerges.

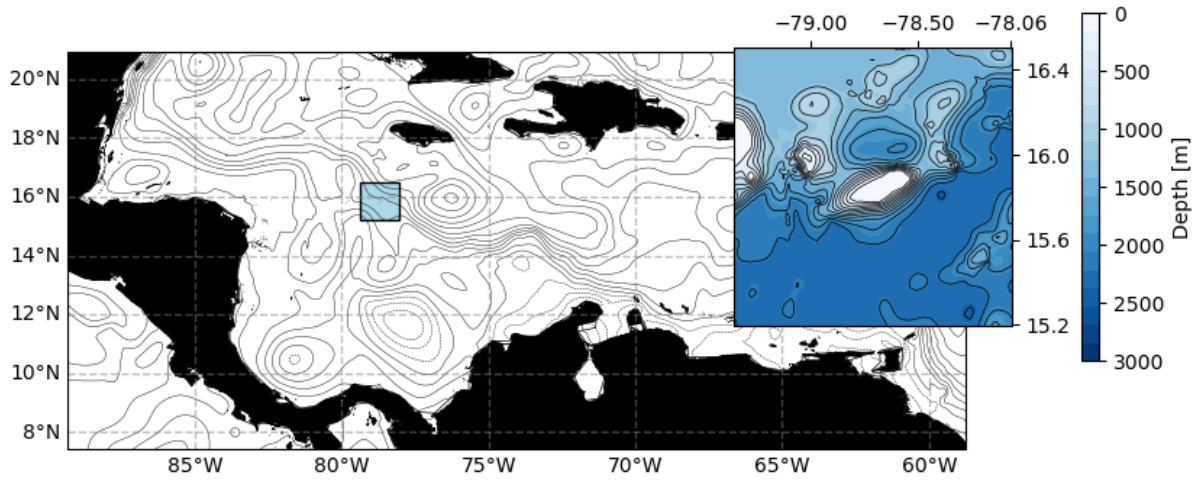

Figure 4.1: This section's region of analysis in the hatched box. GEBCO bathymetry for the tiny domain is displayed on the right. Contours are drawn every 200 meters, and colors range from 0 to 3000 meters.

Two experiments are conducted in addition to the reference model (referred to as *Exp. 1* - shown in blue in Fig.4.2).

- *Exp. 2*: in the first case, the initial topography was modified to bring the island up to the surface. The shape of the island was kept the same as it has at 50 m depth, expanding it above this depth consistently with the actual bathymetry below. This experiment is shown in green in Fig.4.2. This type of configuration tries to reproduce the real configuration as closely as possible.

- *Exp. 3*: subsequently, to assess the impact of the island on the development of submesoscale dynamics, it was removed by cutting it at a depth of 50 m, below the mixed layer depth (MLD) in this small area of interest, transforming the initial structure into a seamount. This experiment is shown in red in Fig.4.2.

The dimensions of the island and seamounts is schematised in Tab.4.1.

Exp.	Type	Dimensions	Submergene depth (m)
1	seamount	$\sim$ 11 x 3	5
2	island	$\sim$ 26 x 9 Km	0
3	seamount	$\sim$ 26 x 9 Km	50

Table 4.1: model setup and parameters for the parent and the child model.

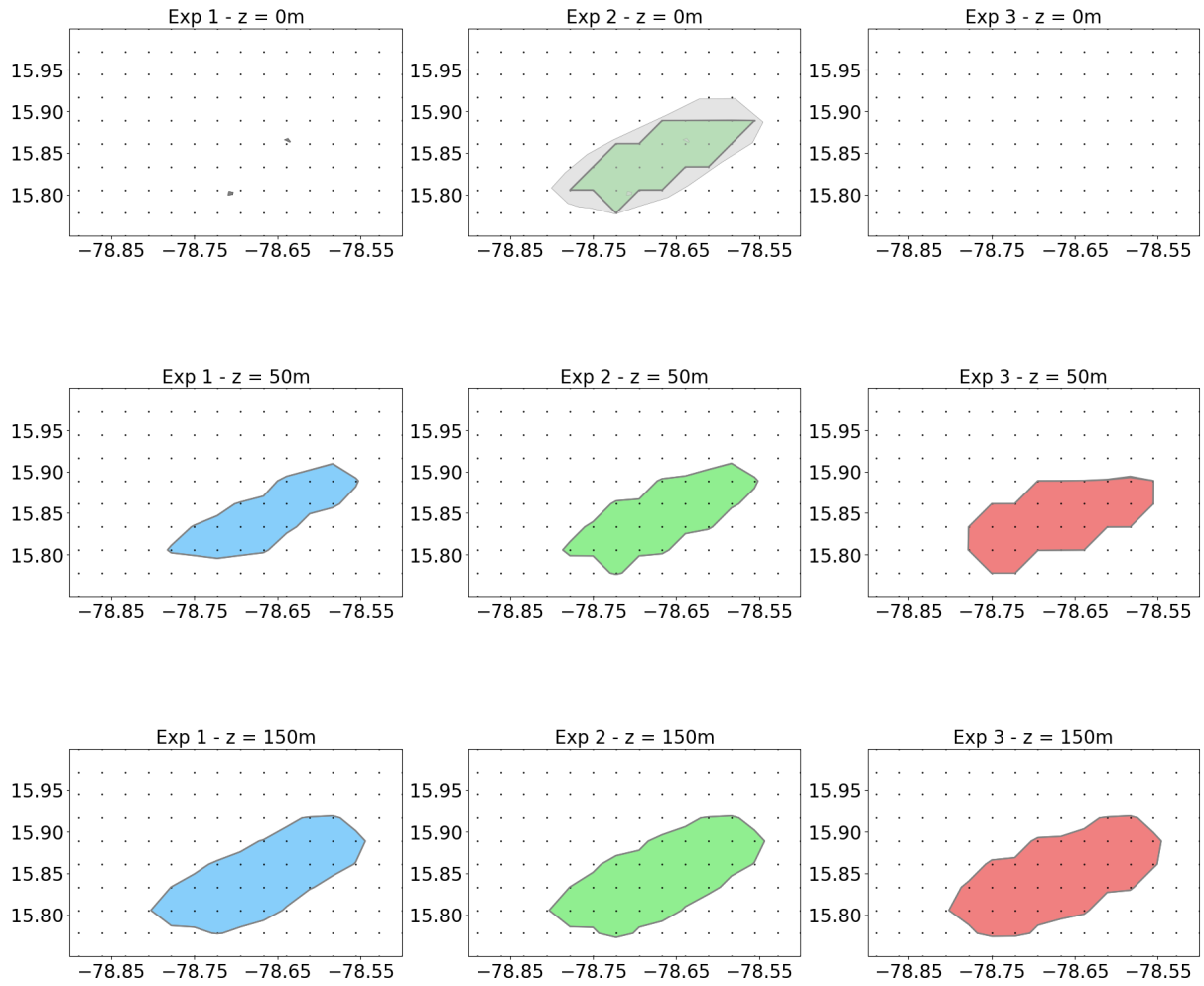

Figure 4.2: In this figure, the bathymetry at the surface (top row of graphs), at a depth of 50 m (second row), and at a depth of 150 m (third row) is shown for each experiment. The first column, depicted in blue, represents the reference child experiment (experiment 1), the second column in green represents experiment 2, and the third column in red represents experiment 3.
Additionally, in the top row, the gray color represents the coastline data used as input for the model. The black dots represent the model grid.

4.3 Current Field and Relative Vorticity Field

In Fig 4.3 the current field and the relative vorticity field comparisons at the surface are shown in our region, on Feb. 5 (first row), on Feb 14 (second row) and on Feb 28 (third row), 2021; for the three Experiments (respectively in the three columns).
These fields are also shown for a depth of 30 m (Fig. 4.4), just above the average MLD.

At the surface, at the beginning of the simulation, no significant differences are observed between Exp.1 and Exp.3, despite the difference in seamount depth. However, in Exp.2, the presence of well-defined structures behind the island starts to become noticeable. Additionally, a front is observed, with currents flowing in opposite directions on either side, approaching the island positioned at the center of each graph. The vorticity field (Fig. 4.3 below) also reveals the presence of this front. On February 14th, this front assumes a distinct cyclonic structure, with a predominance of positive relative vorticity. Exp.3 does not strongly influence this structure, while the first two experiments do. Well-defined wakes can be distinguished with respect to the incident current. After 28 days of simulation behind the emerging island (Exp.2), the wakes have clear directions, indicated by the curvy vectors in the figure, and exhibit submesoscale structures.
Therefore, we conclude that the cyclonic structure observed earlier has lost its energy due to the interaction between the flow and the topography. In the relative vorticity field behind the island, two zones with opposite signs are clearly distinguished. In Exp.3, it can be seen that even at a depth of 50 m, the island causes a local decrease in the surface current velocity in the periphery of the island. Behind this seamount, no submesoscale activity is detected, and even the local field of relative vorticity does not suggest its presence.

At a depth of 30 meters, the seamount at 50 m depth in Exp.3 influences the dynamics and makes the velocity and vorticity fields among the three experiments more similar to each other compared to the surface. The aforementioned cyclonic structure seems to be more distinguishable at this depth, although with lower vorticity and velocity magnitudes. As expected, there is not much difference between Experiments 1 and 2 at this depth, as the geographical structure is more similar. The most substantial differences, as always, are observed in Exp.3, where no submesoscale activity is detected, even at this depth. The vorticity fields remain very similar to the surface fields, with decreased magnitudes. The velocity fields appear to be slightly shifted towards the east in depth.

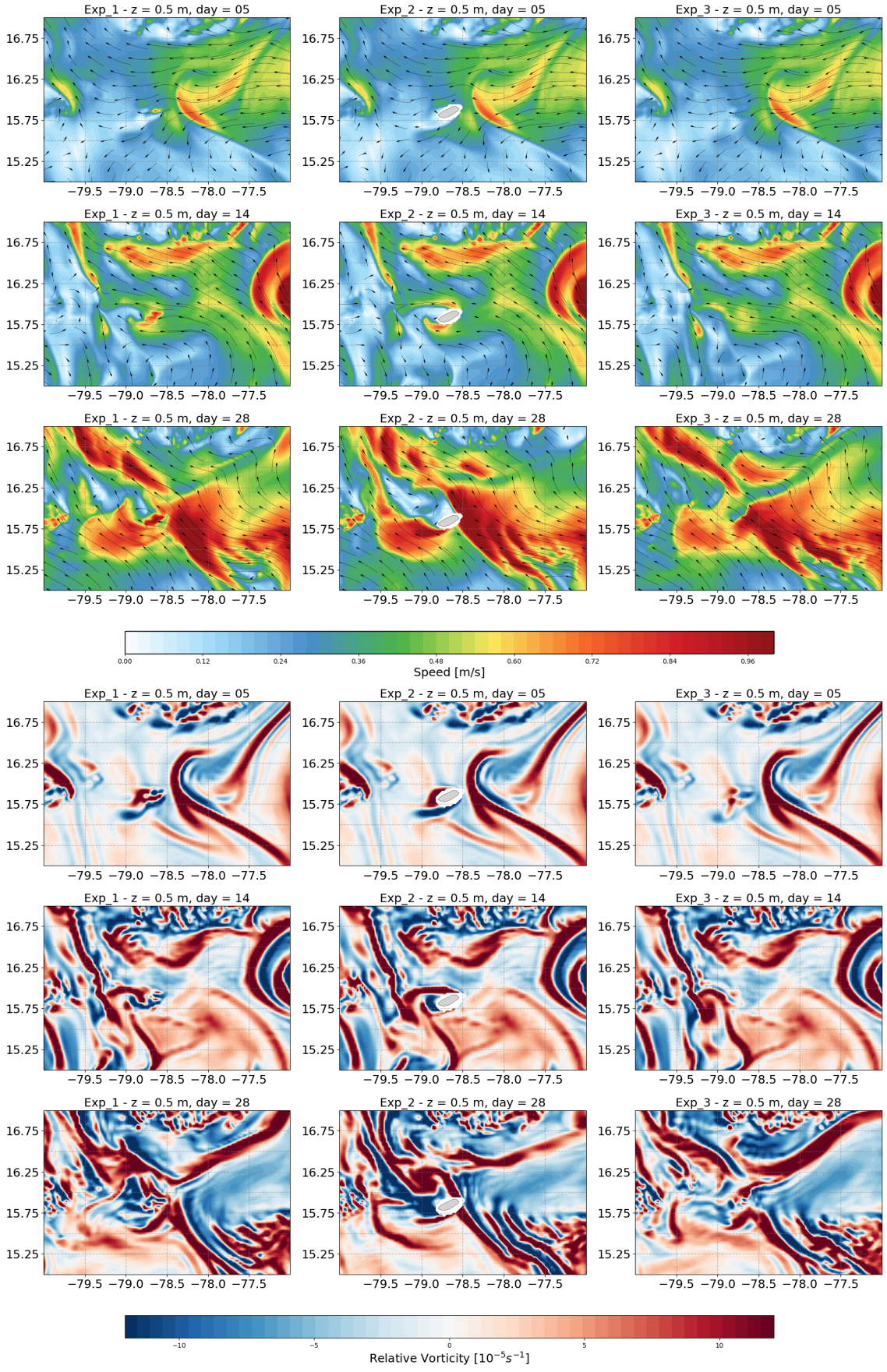

Figure 4.3: Currents (m/s) and relative vorticity ($10^{-5}s^{-1}$) at the surface: comparison between Exp.s 1-2-3 respectively in the 3 columns, on 3 days of the simulation: 5-14-28 Feb. at 00.00 h

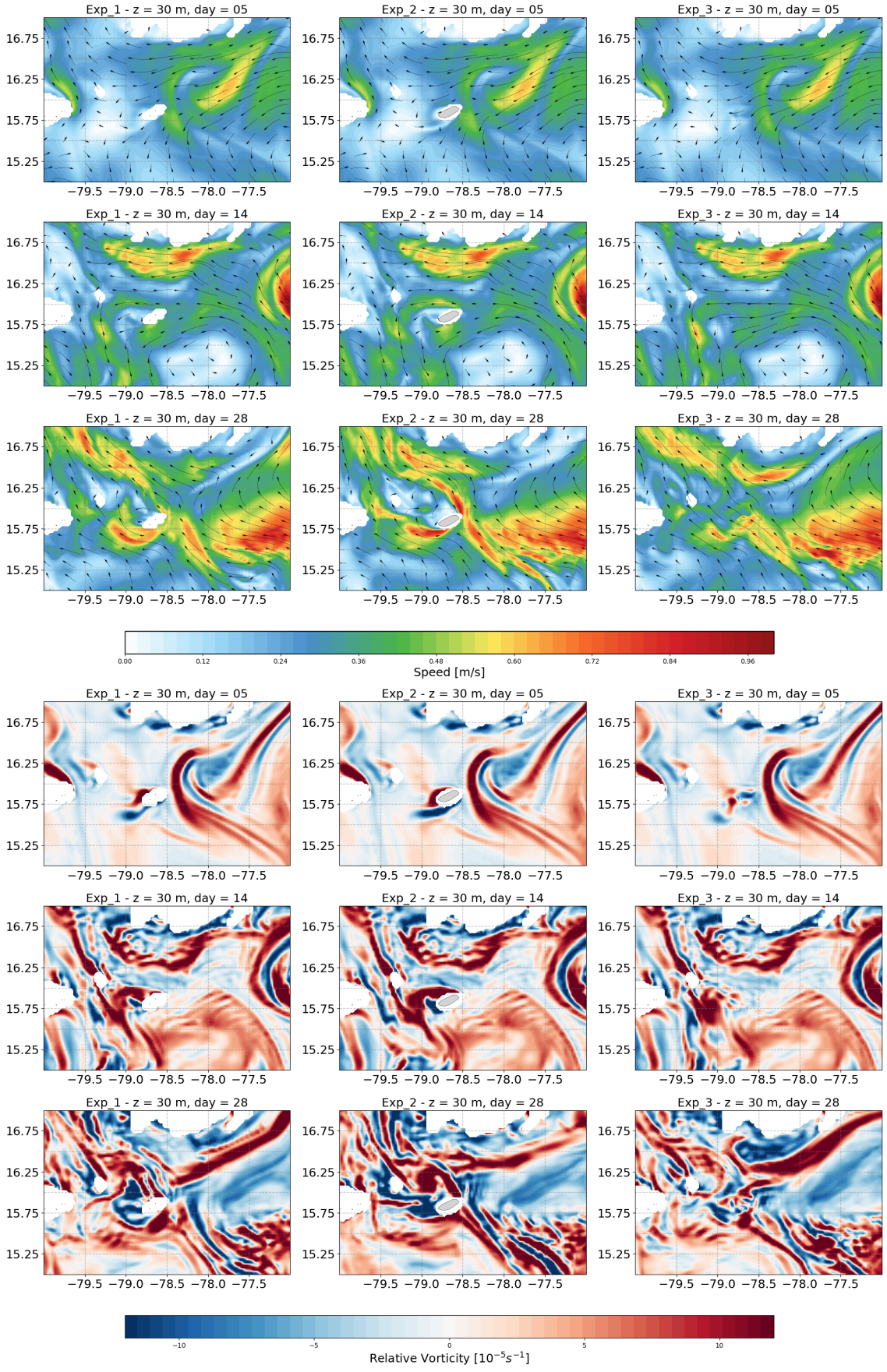

Figure 4.4: Currents (m/s) and relative vorticity ($10^{-5}s^{-1}$) at nearly 30 m depth: comparison between Exp.s 1-2-3 respectively in the 3 columns, on 3 days of the simulation: 5-14-28 Feb. at 00.00 h

4.4 Sea Surface Temperature

According to De Falco et al. 2022 the time-averaged Laplacian (the second horizontal derivative) of the SST is used to detect local fluctuations in temperature close to islands and seamounts:

$$\nabla^2 SST = \frac{\partial^2 SST}{\partial x^2} + \frac{\partial^2 SST}{\partial y^2} \tag{4.1}$$

Although the Laplacian operator does not distinguish between temperature minima and maxima, its extremes benefit small scale structures: areas of significant negative (positive) curvature in the temperature field, such as those surrounding a local cold (warm) anomaly with regard to the large scale field, correspond to strong positive (negative) Laplacian values. It is helpful to identify specific locations with improved vertical mixing or upwelling because places with localized lower temperatures can be reasonably linked to increased inflow of nutrient-rich waters from below the mixed layer. In Fig.4.5 the daily mean $\nabla^2 SST$ field is shown for the three experiments respectively in the 3 columns, on 3 days of the simulation: 5-14-28 Feb.

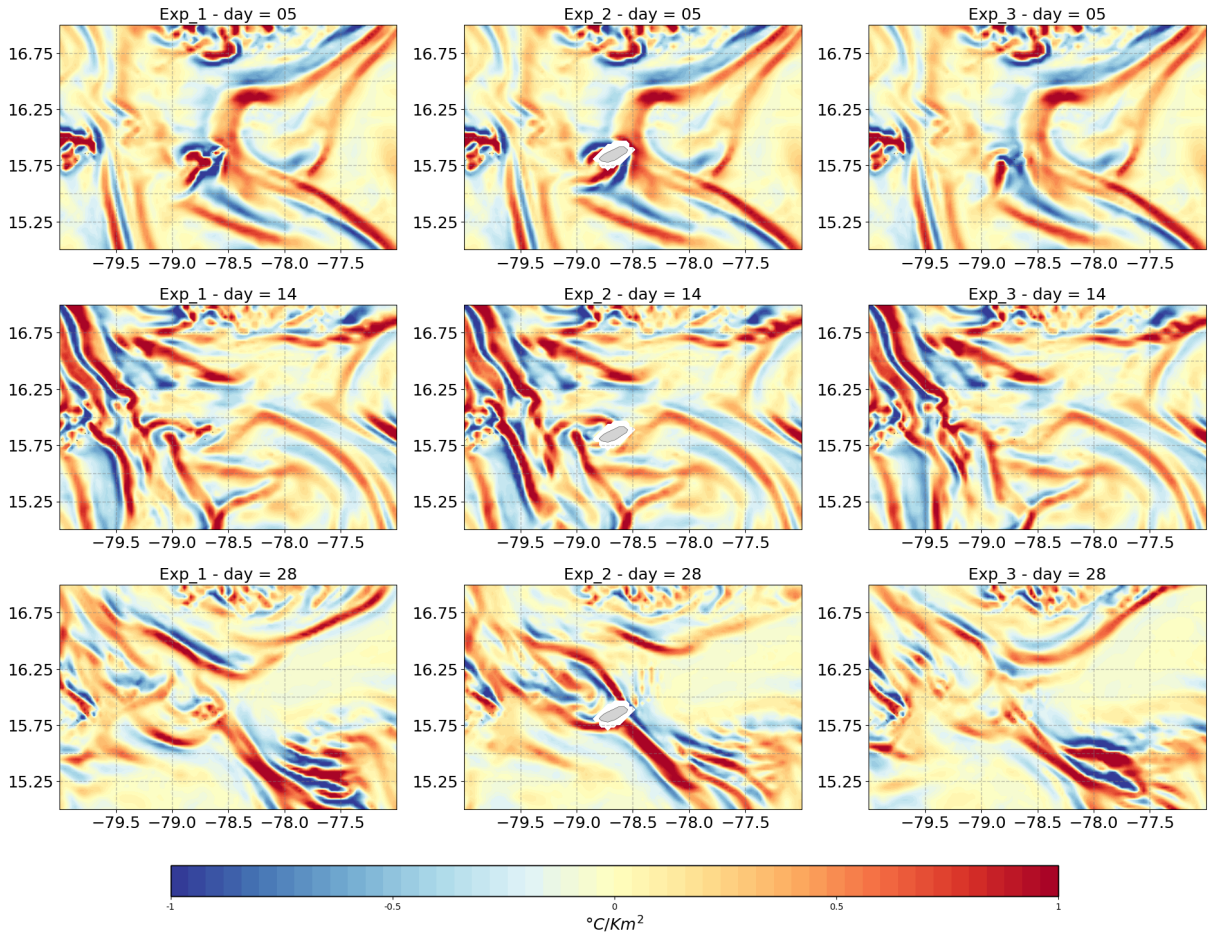

Figure 4.5: $\nabla^2 SST$ (°C/Km): comparison between Exp.s 1-2-3 respectively in the 3 columns, on 3 days of the simulation: 5-14-28 Feb.

The local divergence/convergence leads to upwelling/downwelling, usually associated with cold/warm anomalies and nutrient enriched/deprived waters.
This is consistent with what is shown in Fig.1.9(b).
Between the three experiments, not much difference can be seen except in the last two weeks of the simulation, the structure of the SST Laplacian is very different in the last row of Fig.4.5, especially with regard to the spatial extent of the zones with positive or negative values. In addition, this field is in agreement with the vertical velocity field (see comparison with Fig.4.6), confirming the above.

4.5 Vertical velocity and Mixed Layer Depth

In this section, we will study how the vertical velocity field and the depth of the mixed layer vary in the different cases analyzed; Exp.1, Exp.2, and Exp.3, as shown in Tab. 4.1.
This field is shown in an meridional transect (at 78.9°W) that is on the left of island nearly perpendicular to the mean incident flow direction during simulation. The vertical transects shown in each figure (Figs.4.7-4.9) consist of this direction, see Fig.4.6. This choice allows for a comparison between the dynamics at immediately behind the the island. These fields are displayed for three days of the simulation (Feb 5th, Feb 14th, and Feb 28th), noting that a single time snapshot is shown at midnight each day. The magnitudes of the vertical velocities range from O(10^{-5} to 10^{-6}), and all displayed graphs exhibit a high complexity of structure, with significant spatial variability.

Additionally, each graph includes the mixed layer depth (in black) and density contours in the shallowest part of the transect (in blue).

The most evident characteristic is that, as the days progress in all three experiments, an increase in vertical velocity values is observed. This is consistent with the enhanced submesoscale activity that we had previously captured.
For the first day, the mixed layer depth remains quite similar among the three experiments. However, we note that on the last day of the simulation, the differences are more pronounced, with an decrease in the depth of the mixed layer depth (MLD) in the second experiment compared to the first, this is consistent with the horizontal velocity fields, which show increased submesoscale activity located in that area. A northward displacement in the third experiment is detected.

Regarding the density contours, on Feb 14th and 28th, the surface layers of the ocean is populated by lower density values with respect the first day, and this behaviour is further enhanced in the case of Exp.2 (island) on the last day.

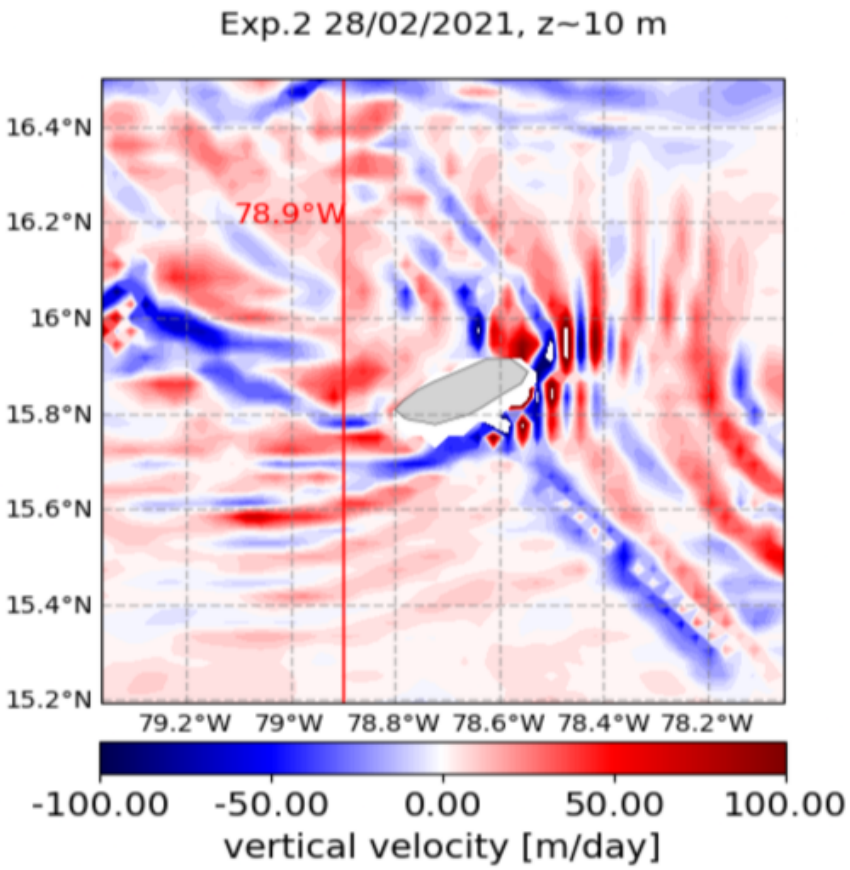

Figure 4.6: Vertical velocity field at a depth of 10 meters for the Exp.2 on the Feb. 28th. The red segment represent the meridional transect along which we will later study the profiles of vertical velocity in the different experiments.

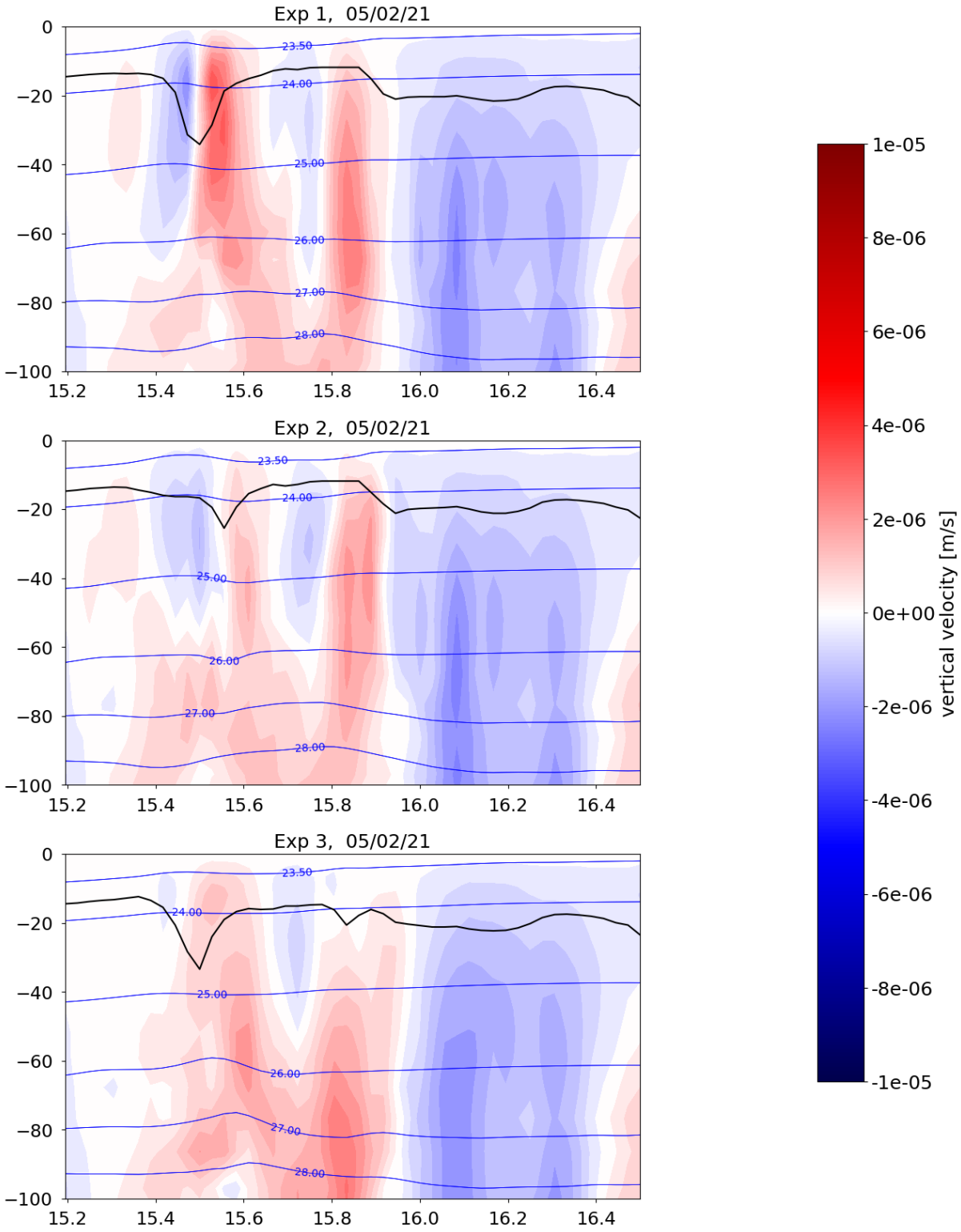

Figure 4.7: Transects for Feb. 5th of density (blue lines) and MLD (black lines), with focus on the first hundred meters, in the vicinity of the island/seamount. The three figures refer to the segment in Fig.4.6. The vertical velocity field is displayed in m/s for the 3 experiments.

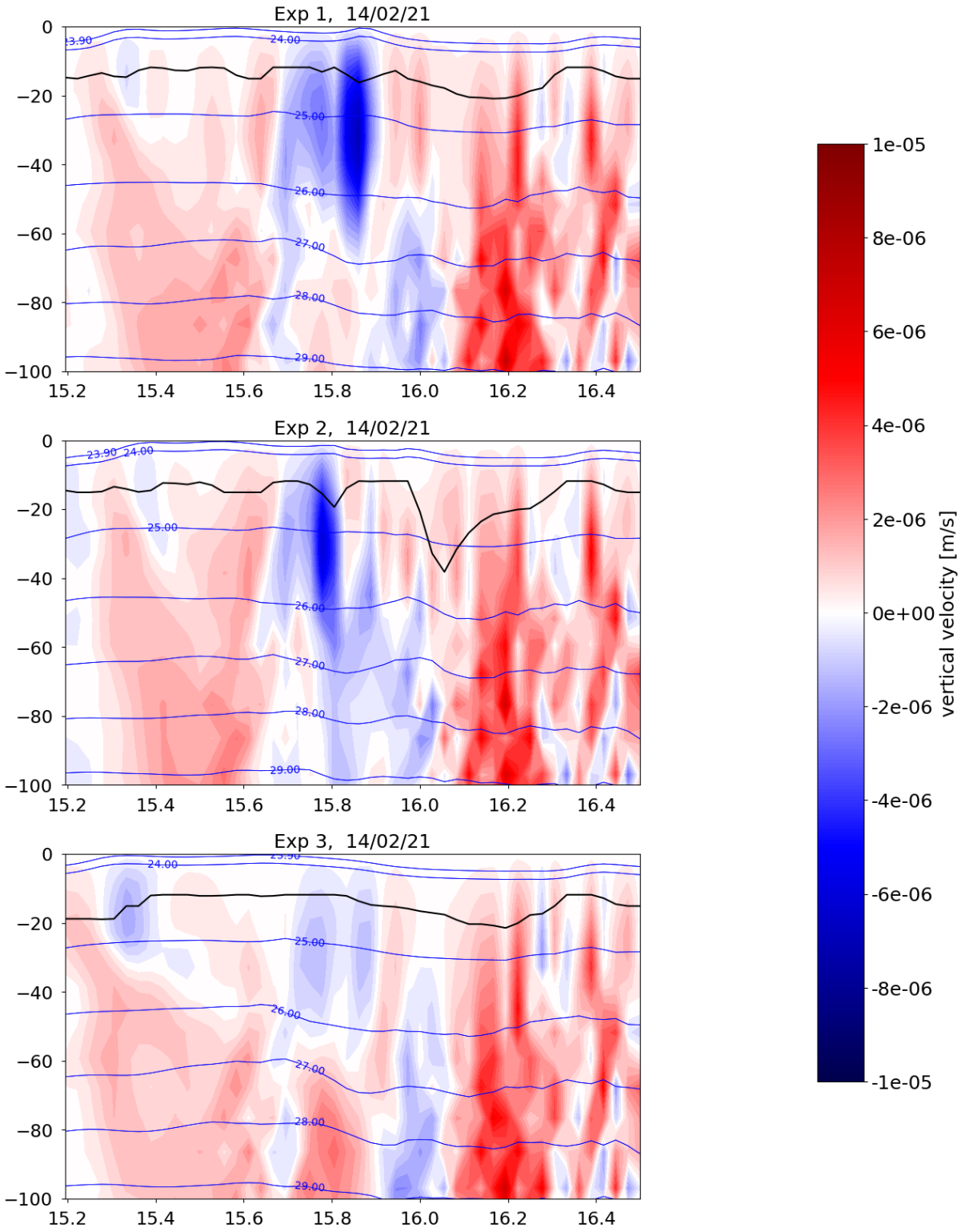

Figure 4.8: Transects for Feb. 14th of density (blue lines) and MLD (black lines), with focus on the first hundred meters, in the vicinity of the island/seamount. The three figures on the left to the segment in Fig.4.6. The vertical velocity field is displayed in m/s for the 3 experiments.

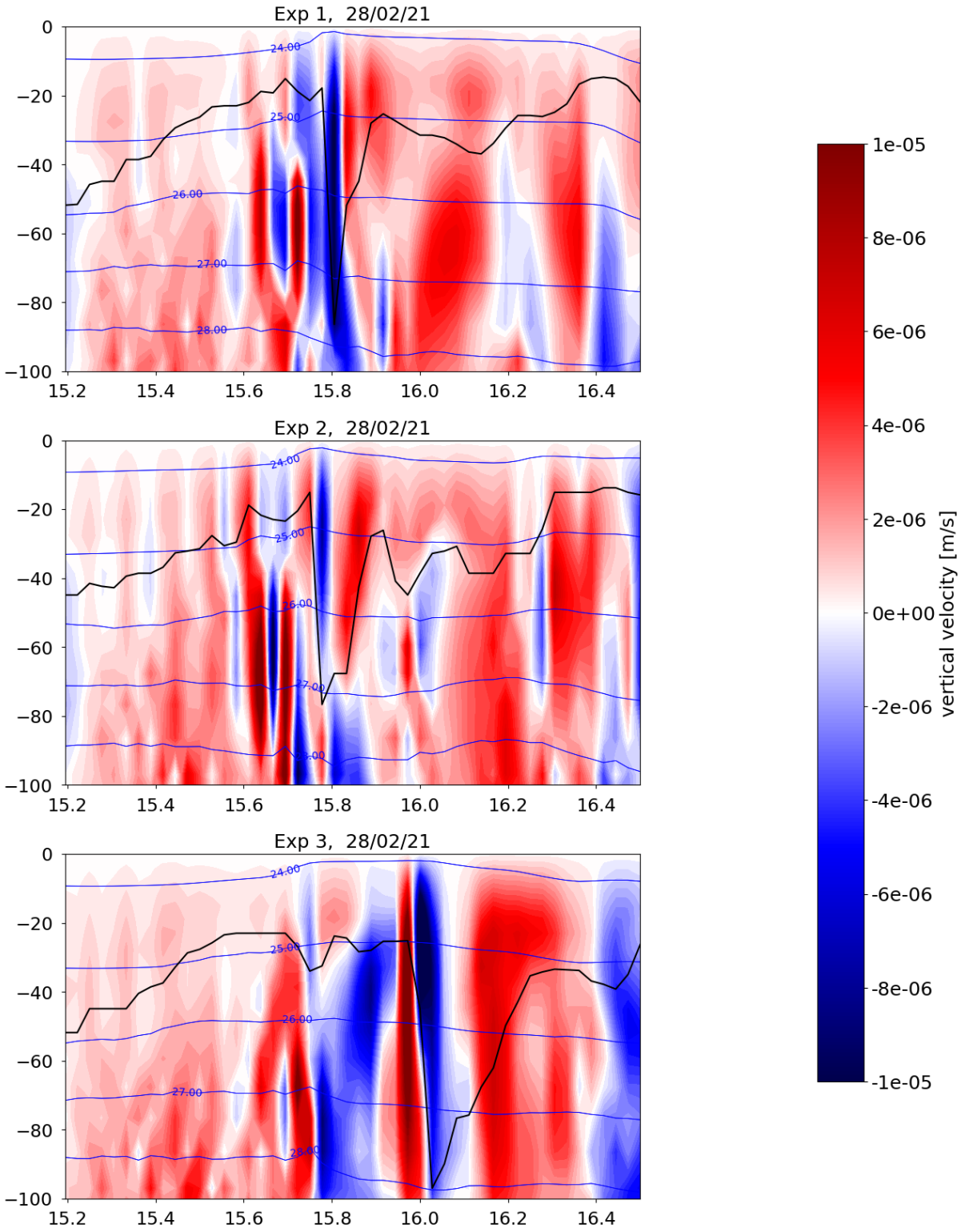

Figure 4.9: Transects for Feb. 14th of density (blue lines) and MLD (black lines), with focus on the first hundred meters, in the vicinity of the island/seamount. The three figures on the left refer to the segment in Fig.4.6. The vertical velocity field is displayed in m/s for the 3 experiments.

4.6 Topographic submesoscale wakes

The work of Srinivasan et al. 2017 was taken into consideration for this section.
As previously stated, surface water contact with the numerous island chains in and around the Chibacha channel is a primary source of submesoscale coherent vortices (SCVs). These SCVs are created by the separation of bottom drag-generated shear layers caused by a barotropic-centrifugal instability of vortical wakes. We investigate the surface flow energetics to characterize the flow-topographic interactions. Energy is transferred from the background mean flow to the eddies in barotropic instabilities. The energy transfer from mean to eddy KE is stated as using a decomposition of the flow fields into mean and deviations as **u**=$\bar{\mathbf{u}}$+**u'**, where the bar represents temporal averages. The energy transfer from mean to eddy KE is written as

$$KmKe = HRS + VRS \tag{4.2}$$

where

$$HRS = -(\overline{u'u'}\overline{u_x} + \overline{u'v'}\overline{u_y} + \overline{v'v'}\overline{v_y} + \overline{u'v'}\overline{v_x}) \tag{4.3}$$

and

$$VRS = -(\overline{v'w'}\overline{v_z} + \overline{u'w'}\overline{u_z}) \tag{4.4}$$

are the contributions from the horizontal and vertical Reynolds stresses to the mean to eddy transfer; KmKe > 0 implies that energy is transferred from the mean to the eddies and vice versa.

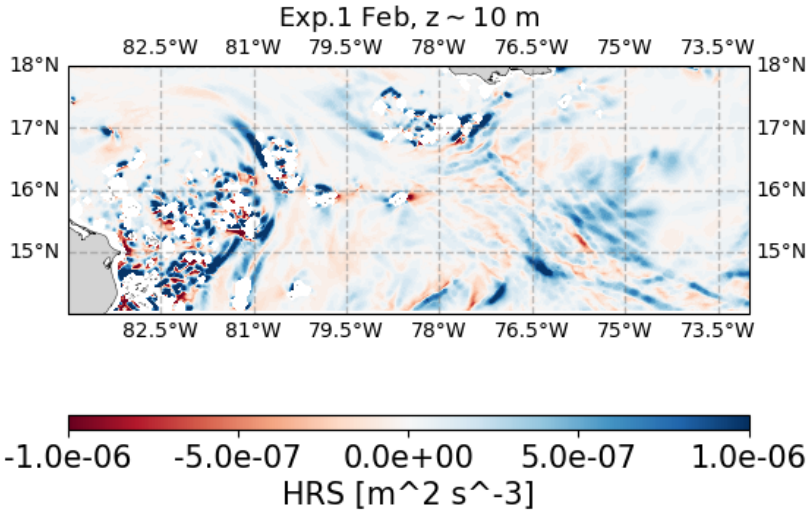

Figure 4.10: HRS ($m^2\ s^{-3}$) at $z = -10$ m averaged over the month of Feb. for the topographically active region in the Chibacha Channel.

Fig. 4.10 shows a spatial map of HRS at a depth of $z = -10\,\mathrm{m}$ (which is well within the mixed layer in this region) on Feb. (thus the averaging operator in Eq. 4.3 is a monthly average here). Strong positive signals in the wakes of headlands and island wakes are observed. These patches of positive HRS (mean to eddy conversions) have narrow (cross-flow) spatial structures with widths less than 20 km, indicating that the eddy generation due to barotropic conversions occurs at the submesoscales (SMs). These patterns are likely a consequence of the small island sizes. From the plots in Fig.4.11 where the HRS field is plotted for the 3 different experiments, it can be observed that the energy transfer from mesoscale to submesoscale, represented by the positive blue values, is highlighted in the case of Exp.2 (emergent island), followed by the reference case, and lastly the seamount case. This provides further confirmation that submesoscale dynamics are enhanced by the presence of islands.

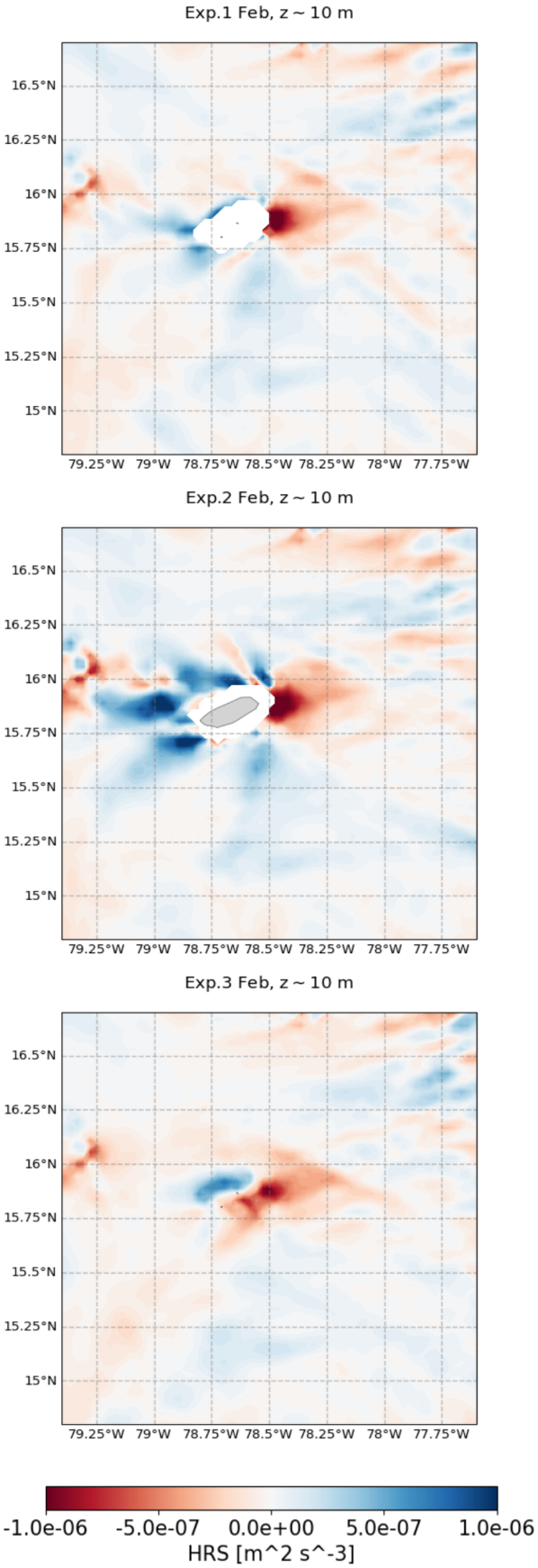

Figure 4.11: Spatial maps of HRS at $z = -10\,\mathrm{m}$ for the topographically active region around the island of interest for the three experiments.

Summary and conclusion

Resolving submesoscale flows in ocean numerical simulations requires very fine resolution grids on the order of 1 km. The dynamical downscaling approach is used to increase the resolution of our numerical model which may better capture ssubmesoscale features in the Caribbean Sea. This approach involves generating a high-resolution nested model based on large-scale information from the Copernicus Marine Environment Monitoring Service (CMEMS) global model. In this study, a nested model at $1/36^\circ$ resolution is created using the NEMO-based SURF platform, downscaling daily average fields from the CMEMS global model at $1/12^\circ$ resolution. The simulation period spans from February 2nd to 28th, 2021, focusing on the winter months when submesoscale activity is more significant. A spin-up period of 3 days is considered at the beginning of the simulation.

In Chapter 3, the mesoscale dynamics of the Caribbean Sea are analyzed, with a focus on velocity, temperature, salinity, and relative vorticity fields at a depth of 10 meters within the surface Mixed Layer. The 9 km resolution model captures the mesoscale circulation patterns but lacks submesoscale features.

The results reveal a complex mesoscale circulation in the Caribbean Sea characterized by strong currents, energetic jets, eddies, and gyres. The North Brazil Current and the North Equatorial Current dominate at a depth of 10 meters, flowing westward with intensities up to 1.4 m/s and a salinity of around 35 PSU. The Subtropical Gyre also contributes to the circulation with slightly higher salinity levels. The Colombia and Venezuela basins exhibit two main current systems at their boundaries, accompanied by various eddy structures including anticyclones and cyclonic circulation patterns. Anticyclonic eddies in the Venezuela basin have warm cores and higher sea surface heights, while cold-core eddies display lower sea surface heights.

The Panama-Colombia Gyre, formed by currents from the Guadeloupe Passage,

exhibits cyclonic structures and interacts with a persistent anticyclonic structure. The currents from the Guadeloupe Passage merge with those in the northern part of the Venezuela basin and exit through the Chibcha channel towards the Mexican coast at high speed.

The temperature distribution shows warmer temperatures ranging from about 22.5°C to 29.5°C in the Colombian basin and Cayman basin, while colder temperatures around 21.5°C are observed along the Venezuela coast. Meanders and vortices in the temperature field indicate the presence of eddies with varying thermal characteristics.

The distribution of tracers follows the progression of anticyclonic eddies, indicating the advection of scalar fields. Vorticity fields provide a clearer view of the structures, particularly in the Chibcha channel, where flow-topography interaction generates thin filaments of positive and negative vorticity.

Previous research attributes the formation of eddies in the Caribbean Sea to flow-topography interaction, meandering of the Caribbean boundary current, and the growth of baroclinic instabilities around river plume fronts. Cold filaments on the eastern side of the basin contribute to cooling in the eastern part of the Caribbean Sea, while eddies transport salinity anomalies from the Amazon and Orinoco river plumes westward.

These findings emphasize the dynamic and intricate nature of the Caribbean Sea's circulation patterns, highlighting the importance of considering mesoscale features when studying the marine environment in the region.

In Chapter 3, the focus shifts to the commencement of submesoscale processes in the Chibcha channel and the benefits of high-resolution downscaled fields. The simulation at 3 km resolution successfully resolves the emergence of submesoscale activities such as eddies and thin filaments of ocean tracers. Compared to the lower-resolution simulation, the higher-resolution simulation reveals a more stratified upper-ocean layer and a more active ocean surface.

The mean value of the Mixed Layer Depth (MLD) is 37.57 m for the parent model and 35.47 m for the child model. We conclude that there is a nearly surfacing of the MLD in a consistent part of our region of interest. The Kinetic Energy (KE) is predominantly confined to the surface layer. In this region, mixed layer instabilities facilitate the conversion of potential energy into kinetic energy, generating both horizontal and vertical ageostrophic (submesoscale) currents, which contribute to restratification. The disparities in the KE structure between the parent and child models are significant. The Rossby number distributions from the parent and child vorticity fields indicate broader distributions with higher standard deviation and kurtosis values in the child model, demonstrating the presence of submesoscale horizontal currents resulting from the dynamical downscaling method.

The study also considers the influence of bathymetry and topography, particularly

the presence of islands and seamounts with dimensions smaller than the grid resolution. The impact of these features on submesoscale dynamics is analyzed in Chapter 4 by modifying the size of an island and conducting sensitivity experiments.

The boundary separation of high-vorticity sheets leads to barotropic instability, which is an important way to transform energy from the mesoscale to submesoscale in the ocean. During the interaction between a current and a seamount, the lower part of the jet is directly affected by the solid seamount, while the upper part is not. Consequently, the vertical structure of the current is significantly affected. Therefore, two experiments are conducted in addition to the reference model: in the first case, the initial topography is modified to bring the island up to the surface, and subsequently, to assess the impact of the island on the development of submesoscale dynamics, it is removed by cutting it at a depth of 50 m, below the mixed layer depth (MLD), transforming the initial structure into a seamount. The submesoscale activity is most evident in the experiment where the island emerges, and well-defined wakes can be distinguished with respect to the incident current. This is the case when we try to reproduce the actual conformation of the island. In the third experiment (seamount), no submesoscale activity is detected.

The analysis of the surface temperature field was conducted by studying the Laplacian of this variable, which allows the identification of small local fluctuations. It is helpful to identify specific locations with improved vertical mixing or upwelling because places with localized lower temperatures can be reasonably linked to increased inflow of nutrient-rich waters from below the mixed layer. The local divergence/convergence leads to upwelling/downwelling, usually associated with cold/warm anomalies and nutrient-enriched/deprived waters. In the third experiment, in particular, although the seamount is still quite high, the temperature field does not show any fluctuations that can be attributed to it.

The vertical velocity field suggests that near the three configurations, the vertical velocity increases in the last two weeks of the simulation, confirming an increase in kinetic energy. Finally, this last field was analyzed by studying the energy transfer from mean to eddy kinetic energy. These patches of positive Horizontal Kinetic Energy Reynolds Stress (HRS), indicating mean to eddy conversions, have narrow (cross-flow) spatial structures with widths less than 20 km, indicating that the eddy generation due to barotropic conversions occurs at the submesoscales. These patterns are likely a consequence of the small island sizes.

4.7 Future outlook

In order to improve the statistical analysis, it is advisable to broaden the range of experiments by exploring different depths and sizes of seamounts and islands.

In addition to the examination of the classical phenomenon of a flow encountering an obstacle, further investigation into the phenomenon of eddy splitting would be of great interest. Specifically, studying the interaction between single or multiple eddies with islands and seamounts in a realistic setting, considering actual topography and bathymetry, would provide valuable insights. Furthermore, it is crucial to quantify the increase in Net Primary Productivity (NPP) around islands. This phenomenon, known as the Island Mass Effect (IME), involves enhanced upwelling and mixing, leading to an influx of nutrients in the euphotic layer and promoting biological productivity while reducing surface temperature. Understanding the factors influencing the IME requires case-specific studies.

APPENDIX A

Equations Governing Geophysical Flows

The constitutive equations for fluid dynamics were derived from the concept of continuous media. In particular the advective term $\boldsymbol{v} \cdot \boldsymbol{\nabla}$ represents the effect of convection or the transfer of the property due to the movement of the fluid itself, in the context of fluid dynamics equations, such as the Navier-Stokes equations, the advection term accounts for the contribution of the fluid's velocity field to the transport of the desired property. The evolution of this physical properties can be described using Eulerian or Lagrangian point of view, and a set of conservation equations of mass, momentum and energy, were derived for a Lagrangian coordinate system (Cx K Batchelor 1967; Currie 1993). We are going to characterize the state of the ocean by seven field variables, the velocity field $\boldsymbol{u} = (u, v, w) = u_i$, the pressure field p, the density ρ, the temperature T and the salinity S.

A necessary statement in fluid mechanics is that mass be conserved, and mathematically the statement takes the following form (continuity equation):

$$\frac{\partial \rho}{\partial t} + \nabla \cdot (\rho \boldsymbol{v}) = 0. \tag{A.1}$$

For a fluid, Newton's second law is better stated per unit volume with density replacing mass, and augmenting the acceleration term for geophysical flows, in with *rotation of the earth is important.*

The resulting equations are called the Navier-Stokes equations[1]:

$$\frac{\partial \boldsymbol{v}}{\partial t} + \boldsymbol{v} \cdot \boldsymbol{\nabla} \boldsymbol{v} + 2\boldsymbol{\Omega} \times \boldsymbol{v} = -\frac{1}{\rho}\boldsymbol{\nabla} p - g\hat{k} + \nu \nabla^2 \boldsymbol{v}. \tag{A.2}$$

where: $\Omega = 7.2910^{-5} s^{-1}$ is the angular velocity of the earth and $\nu = \frac{\mu}{\rho} \sim 10^{-6} m^2 s^{-1}$ is the kinematic viscosity and $\mu \sim 10^{-3} K g m^{-1} s^{-1}$ the molecular viscosity of the water.
The description of the fluid system is not complete until we also provide a relation between density and pressure. This relation is called *equation of state* and tell us about the nature of fluid. In the ocean water density is a complicated function of pressure, temperature and salinity (Gill 1982).
We can define a new quantity called potential temperature: $\theta = T + \int_p^{p_r=0} (\frac{\partial T}{\partial p_s})_s dp$; that is useful because it takes into account the variations in pressure and temperature in a fluid so that two volumes of water having the same potential temperature have the same thermodynamic properties regardless of their absolute pressures and temperatures.
Finally the equation of state can be written as a function of the potential temperature and the salinity:

$$\rho = f(\theta, S). \tag{A.3}$$

Additionally the equation governing temperature arises from conservation of energy, this principle known as the first law of thermodynamics ($\frac{de}{dt} = Q - W$).
Replacing each quantity with its own mathematical definition, we arrive at the simple final formulation.
We can write the equation for temperature directly as the equation for potential temperature as:

$$\frac{\partial \theta}{\partial t} + \boldsymbol{v} \cdot \nabla \theta = K^* \nabla^2 \theta. \tag{A.4}$$

Where $K^* \sim 1.510^{-7} m^2 s^{-1}$ is the molecular diffusivity of temperature.
The last variable for which an equation for the ocean is required is the salinity. This is written as:

$$\frac{\partial S}{\partial t} + \boldsymbol{v} \cdot \nabla S = K_S^* \nabla^2 S. \tag{A.5}$$

Where $K_S^* \sim 10^{-9} m^2 s^{-1}$ is the molecular diffusivity of salinity.
Our set of governing equation is completed, there are again seven variables *(u, v, w, p, ρ, T and S)* for which we have continuity (A.1), momentum (A.2) and temperature equations (A.4), the equation of state (A.3) and the salt equation (A.5).

[1]The neglect of curvature terms is analogous to the distortion introduced by mapping the curved earth's surface onto a plane. If the dimensions of the domain be comparable with the size of the planet, the axes of the Cartesian system of coordinates should be replaced by spherical coordinates.

APPENDIX B

Turbulence closure schemes

Turbulence closure schemes are mathematical models used in fluid dynamics to simulate the effects of turbulence, which is a complex and chaotic behaviour of fluid flow that is difficult to model directly. There are many different types of turbulence closure schemes, but the one that we use in this work is the Reynolds-averaged Navier-Stokes (RANS) models. RANS models average out the turbulent fluctuations, providing a simplified solution to the equations of motion.

We decompose each variable into a mean, denoted with a set of brackets, and a fluctuation, denoted by a prime: $u = \langle\ u\ \rangle + u'$ such that $\langle u' \rangle = 0$ by definition.[1] So we have to average the $x-$, $y-$ and $z-$ momentum (A.2) equations over the turbulent fluctuations, and we have to note the presence of three new terms that represent the effects of turbulent fluctuations on the mean flow and that are called *Reynolds stresses* τ_{ij} (B.1). Reynolds stresses therefore make up a tensor like the viscous one but now containing the moment flux of the turbulent fluctuations.

In order to account for the cumulative impact of unresolved turbulent and subgrid scale motions on the larger, resolved flow, it is imperative to address these phenomena.

This process is called the *subgrid-scale parameterization*. The so-called *turbulence closure hypothesis* must therefore be invoked. Starting from empirical evidence, we will rewrite the turbulent Reynolds stresses in terms of the mean fields, assuming that the

[1] The averaging process can be defined as a temporal average over rapid turbulent fluctuations.

turbulent motion is generated by the mean one and in particular by its gradients (B.2).

$$\tau_{ij} = -\rho \begin{bmatrix} \langle u_i' u_i' \rangle & \langle u_i' u_j' \rangle & \langle u_i' u_k' \rangle \\ \langle u_j' u_i' \rangle & \langle u_j' u_j' \rangle & \langle u_j' u_k' \rangle \\ \langle u_k' u_i' \rangle & \langle u_k' u_j' \rangle & \langle u_k' u_k' \rangle \end{bmatrix} \tag{B.1}$$

$$\tau_{ij} = A_i \langle u_j \rangle_{,i} + A_j \langle u_i \rangle_{,j} \tag{B.2}$$

Because $A_i = (A_h, A_h, A_v)$, A_v and A_h are respectively called vertical and horizontal turbulent viscosity coefficients, and are defined as $A_i = \rho \langle l_i u_i' \rangle$ where l_i are the mixing lengths. It's easy to prove that $A_v << A_h$, this means that the horizontal mixing lengths are much larger than the vertical ones and therefore the horizontal turbulence is formed by large vortexes that have a very long average life and therefore mix very slowly over time.

Similarly to the case of the momentum equations, turbulent diffusivity coefficients are defined for temperature and salinity respectively K_v, K_h and K_v^s, K_h^s. The method used in this section has been described in detail by Benoit Cushman-Roisin 2011 and Nadia Pinardi 2021.

Bibliography

A. Adcroft, et al. (2011). *Ocean Mesoscale Eddies, from Geophysical Fluid Dynamic Laboratory*. Articolo. URL: https://www.gfdl.noaa.gov/ocean-mesoscale-eddies/.

Becker, JJ et al. (2009). "Global bathymetry and elevation data at 30 arc seconds resolution: SRTM30_PLUS". In: *Marine Geodesy* 32.4, pp. 355–371.

Benoit Cushman-Roisin, et al. (2011). *Introduction to geophysical fluid dynamics: physical and numerical aspects*. Academic press.

Capet, X. et al. (2008a). "Mesoscale to Submesoscale Transition in the California Current System. Part I: Flow Structure, Eddy Flux, and Observational Tests". In: *Journal of Physical Oceanography* 38.1, pp. 29–43. DOI: https://doi.org/10.1175/2007JPO3671.1. URL: https://journals.ametsoc.org/view/journals/phoc/38/1/2007jpo3671.1.xml.

— (2008b). "Mesoscale to Submesoscale Transition in the California Current System. Part I: Flow Structure, Eddy Flux, and Observational Tests". In: *Journal of Physical Oceanography* 38.1, pp. 29–43. DOI: https://doi.org/10.1175/2007JPO3671.1. URL: https://journals.ametsoc.org/view/journals/phoc/38/1/2007jpo3671.1.xml.

Cavallini, Fabio and Fulvio Crisciani (2012). *Quasi-geostrophic theory of Oceans and atmosphere: topics in the dynamics and thermodynamics of the Fluid Earth*. Vol. 45. Springer Science & Business Media.

Chelton, D. et al. (2011). "Global observations of nonlinear mesoscale eddies". In: *Progress in oceanography* 91.2, pp. 167–216.

Currie, IG (1993). "Fundamental Mechanics of Fluids, McGra. w-Hill". In: *Inc, New York NY*.

Cx K Batchelor, et al. (1967). *An introduction to fluid dynamics*. Cambridge university press.

D Pettenuzzo, et al. (2010). "On the corrections of ERA-40 surface flux products consistent with the Mediterranean heat and water budgets and the connection between basin surface total heat flux and NAO". In: *Journal of Geophysical Research: Oceans* 115.C6.

D. Chelton, et. al (1998). "Geographical variability of the first baroclinic Rossby radius of deformation". In: *Journal of Physical Oceanography* 28.3, pp. 433–460.

De Falco, Chiara et al. (2022). "Island mass effect: A review of oceanic physical processes". In: *Frontiers in Marine Science* 9, p. 1252.

Egbert, Gary D. and Svetlana Y. Erofeeva (2002). "Efficient Inverse Modeling of Barotropic Ocean Tides". In: *Journal of Atmospheric and Oceanic Technology* 19.2, pp. 183–204. DOI: https://doi.org/10.1175/1520-0426(2002)019<0183:EIMOBO>2.0.CO;2. URL: https://journals.ametsoc.org/view/journals/atot/19/2/1520-0426_2002_019_0183_eimobo_2_0_co_2.xml.

F. Trotta, et al. (2016). "A Structured and Unstructured grid Relocatable ocean platform for Forecasting (SURF)". In: *Deep Sea Research Part II: Topical Studies in Oceanography* 133. Physical, chemical and biological observations and modelling of oil spills in the Mediterranean Sea, pp. 54–75. ISSN: 0967-0645. DOI: https://doi.org/10.1016/j.dsr2.2016.05.004. URL: https://www.sciencedirect.com/science/article/pii/S0967064516301047.

— (2017). "Multi-nest high-resolution model of submesoscale circulation features in the Gulf of Taranto". In: *Ocean Dynamics* 67, pp. 1609–1625.

— (2021). "A relocatable ocean modeling platform for downscaling to shelf-coastal areas to support disaster risk reduction". In: *Frontiers in Marine Science* 8, p. 642815.

G. Boccaletti, et. al (2007). "Mixed layer instabilities and restratification". In: *Journal of Physical Oceanography* 37.9, pp. 2228–2250.

Gill, Adrian E (1982). *Atmosphere-ocean dynamics*. Vol. 30. Academic press.

Gula, Jonathan et al. (2022). "Submesoscale processes and mixing". In: *Ocean Mixing*. Elsevier, pp. 181–214.

John R Taylor, et al. (2011). "Shutdown of turbulent convection as a new criterion for the onset of spring phytoplankton blooms". In: *Limnology and Oceanography* 56.6, pp. 2293–2307.

— (2023). "Submesoscale Dynamics in the Upper Ocean". In: *Annual Review of Fluid Mechanics* 55.1, pp. 103–127. DOI: 10.1146/annurev-fluid-031422-095147. eprint: https://doi.org/10.1146/annurev-fluid-031422-095147. URL: https://doi.org/10.1146/annurev-fluid-031422-095147.

Jouanno, Julien et al. (2008). "The mesoscale variability in the Caribbean Sea. Part I: Simulations and characteristics with an embedded model". In: *Ocean Modelling* 23.3-4, pp. 82–101.

Kingsford, Michael John (2023). "Marine ecosystem". In: *Encyclopaedia Britannica*. URL: https://www.britannica.com/science/marine-ecosystem.

LaCasce, et al. (2020). "Baroclinic modes over rough bathymetry and the surface deformation radius". In: *Journal of Physical Oceanography* 50.10, pp. 2835–2847.

Law Chune, S et al. (2019). "PRODUCT USER MANUAL for the GLOBAL Ocean Sea Physical Analysis and Forecasting Products GLOBAL_ANALYSIS_FORECAST_PHY_001_024". In: *Copernicus Marine Environment Monitoring Service, Toulouse, France.*

Le Traon, Pierre Yves et al. (2019). "From observation to information and users: The Copernicus Marine Service perspective". In: *Frontiers in Marine Science* 6, p. 234.

LN Thomas, et al. (2008). "Submesoscale processes and dynamics". In.

López-Álzate, Margarita E et al. (2022). "Mesoscale eddy variability in the Caribbean Sea". In: *Ocean Dynamics* 72.9-10, pp. 679–693.

M. Jeroen Molemaker, et al. (2015). "Submesoscale Instability and Generation of Mesoscale Anticyclones near a Separation of the California Undercurrent". In: *Journal of Physical Oceanography* 45.3, pp. 613–629. DOI: https://doi.org/10.1175/JPO-D-13-0225.1. URL: https://journals.ametsoc.org/view/journals/phoc/45/3/jpo-d-13-0225.1.xml.

Maicu, Francesco et al. (2021). "Downscaling with an unstructured coastal-ocean model to the Goro Lagoon and the Po River Delta branches". In: *Frontiers in Marine Science* 8, p. 647781.

McWilliams, J.C (2016). "Submesoscale currents in the ocean". In: *Proceedings of the Royal Society A: Mathematical, Physical and Engineering Sciences* 472.2189, p. 20160117.

Miracca-Lage, Mariana et al. (2022). "Can the Surface Quasi-Geostrophic (SQG) Theory Explain Upper Ocean Dynamics in the South Atlantic?" In: *Journal of Geophysical Research: Oceans* 127.2, e2021JC018001.

Müller, et al. (2005). "Routes to dissipation in the ocean: The 2D/3D turbulence conundrum". In: *Marine turbulence: theories, observations and models* 397, p. 405.

Pinardi, N. et al. (2003). "The Mediterranean ocean forecasting system: first phase of implementation (1998–2001)". In: *Annales Geophysicae* 21.1, pp. 3–20. DOI: 10.5194/angeo-21-3-2003. URL: https://angeo.copernicus.org/articles/21/3/2003/.

Pinardi, Nadia (2010). "FROM OCEAN MESOSCALE MODELLING TO OPERATIONAL OCEANOGRAPHY: A TRIBUTE TO A.R. ROBINSON". In: *CIESM Congress 2010.*

Pinardi, Nadia (2021). *Physical Oceanography Notes for Master Degree program in Earth System Science*. Pacchetto di slide. URL: https://www.unibo.it/it/didattica/insegnamenti/insegnamento/2021/412224.

S. Kanwal, et al. (Feb. 2021). "SeaDataCloud Density Climatology for the Global Ocean". In: DOI: 10.12770/725d02ed-2c93-44e8-a1ac-48a9cd5ac883.

Simoncelli, Simona et al. (2011). "Coastal Rapid Environmental Assessment in the Northern Adriatic Sea". In: *Dynamics of Atmospheres and Oceans* 52.1. Special issue of Dynamics of Atmospheres and Oceans in honor of Prof. A.R.Robinson, pp. 250–283. ISSN: 0377-0265. DOI: https://doi.org/10.1016/j.dynatmoce.2011.04.004. URL: https://www.sciencedirect.com/science/article/pii/S0377026511000182.

Srinivasan, Kaushik et al. (2017). "Topographic and mixed layer submesoscale currents in the near-surface southwestern tropical Pacific". In: *Journal of Physical Oceanography* 47.6, pp. 1221–1242.

Stammer, Detlef (1997). "Global Characteristics of Ocean Variability Estimated from Regional TOPEX/POSEIDON Altimeter Measurements". In: *Journal of Physical Oceanography* 27.8, pp. 1743–1769. DOI: 10.1175/1520-0485(1997)027<1743:GCOOVE>2.0.CO;2. URL: https://journals.ametsoc.org/view/journals/phoc/27/8/1520-0485_1997_027_1743_gcoove_2.0.co_2.xml.

Talley, Lynne D (2011). *Descriptive physical oceanography: an introduction*. Academic press.

Torres, Hector S et al. (2018). "Partitioning ocean motions into balanced motions and internal gravity waves: A modeling study in anticipation of future space missions". In: *Journal of Geophysical Research: Oceans* 123.11, pp. 8084–8105.

TWN Haine, et al. (1998). "Gravitational, symmetric, and baroclinic instability of the ocean mixed layer". In: *Journal of physical oceanography* 28.4, pp. 634–658.

Wang, Qingyue et al. (2022). "Submesoscale processes-induced vertical heat transport modulated by oceanic mesoscale eddies". In: *Deep Sea Research Part II: Topical Studies in Oceanography* 202, p. 105138. ISSN: 0967-0645. DOI: https://doi.org/10.1016/j.dsr2.2022.105138. URL: https://www.sciencedirect.com/science/article/pii/S0967064522001230.

Yang, S. et al. (2017). "A modelling study of eddy-splitting by an island/seamount". In: *Ocean Science* 13.5, pp. 837–849. DOI: 10.5194/os-13-837-2017. URL: https://os.copernicus.org/articles/13/837/2017/.

Zhou, Jiang et al. (2021). "Mesoscale Eddy-Induced Ocean Dynamic and Thermodynamic Anomalies in the North Pacific". In: *Frontiers in Marine Science*, p. 1695.